REPORT DOCUMENTATION PAGE

AD-A215 348

Public reporting burden for this collection of information is estimated to average 1 hour per response, including the time for reviewing instructions, searching existing data sources, gathering and maintaining the data needed, and completing and reviewing the collection of information. Send comments regarding the burden estimate or any other aspect of this collection of information, including suggestions for reducing this burden, to Washington Headquarters Services, Directorate for Information Operations and Reports, 1215 Jefferson Davis Highway, Suite 1204, Arlington, VA 22202-4302, and to the Office of Management and Budget, Paperwork Reduction Project (0704-0188), Washington, DC 20503.

1. AGENCY USE ONLY (Leave blank)	2. REPORT DATE	3. REPORT TYPE AND DATES COVERED
	February 82	Final (1 Nov 80-31 Oct 81

4. TITLE AND SUBTITLE	5. FUNDING NUMBERS
THE STRUCTURE OF FLOWS WITH UNSTEADY BOUNDARY CONDITIONS	61102F 2307/A2

6. AUTHOR(S)

Hermann Viets   Mont Ball
Richard J. Bethke   David Bougine

7. PERFORMING ORGANIZATION NAME(S) AND ADDRESS(ES)	8. PERFORMING ORGANIZATION REPORT NUMBER
Wright State University Dept of Engineering Dayton, OH 45435	AFOSR·TR· 89-1519

9. SPONSORING/MONITORING AGENCY NAME(S) AND ADDRESS(ES)	10. SPONSORING/MONITORING AGENCY REPORT NUMBER
AFOSR BLDG 410 BAFB DC 20332-6448	AFOSR-81-0025

11. SUPPLEMENTARY NOTES

12a. DISTRIBUTION/AVAILABILITY STATEMENT	12b. DISTRIBUTION CODE
Approved for public release; distribution unlimited.	

13. ABSTRACT (Maximum 200 words)

14. SUBJECT TERMS			15. NUMBER OF PAGES
			138
			16. PRICE CODE

17. SECURITY CLASSIFICATION OF REPORT	18. SECURITY CLASSIFICATION OF THIS PAGE	19. SECURITY CLASSIFICATION OF ABSTRACT	20. LIMITATION OF ABSTRACT
unclassified	unclassified		

The Structure of Flows with Unsteady
Boundary Conditions

Hermann Viets, Richard J. Bethke,
Mont Ball and David Bougine

Acoession For	
NTIS GRA&I	☒
DTIC TAB	☐
Unannounced	☐
Justification	
By	
Distribution/	
Availability Codes	
Dist	Avail and/or Special
A-1	

Identification of Convected Flow Structures
by Decomposition Techniques[+]

Richard J. Bethke[*]
Wright State University
Dayton, Ohio   45435

Hermann Viets[**]
West Virginia University
Morgantown, WV   26506

Introduction

Convected large scale structures have been identified in many different

flows such as wall boundary layers, wakes, and jets. In each case, the

presence of the coherent structures can have a significant effect on the

overall flow properties such as pressure distributions and mixing rates.

In order to successfully predict the overall properties, the dynamics of

the large scale structures must be understood and reasonably modeled. This

requires first that the structures must be identified in experimental data

and it is the purpose of this paper to propose an improved method to do so.

The difficulties involved with searching for a convected vortex structure

in a general flow field have been treated by Lugt[1]. In a previous paper,[2] the

present authors discussed a method of c   .nt structure identification which

was based on a Fourier transformation. I..   technique proved to be very

useful in isolating the coherent vortex structures and hence illuminating

the dynamics of those structures.

---

[*] Associate Professor, Engineering Department

[**] Professor and Associate Dean, College of Engineering

The present identification technique appears to allow the identification of smaller and less well defined structures. It is based on the concept of decomposing the flow (specifically the velocity field) into various components of rotation, translation, shear, etc. and then determine the magnitude and importance of each of these elements.

The Model

The flow model is organized in terms of the data cell illustrated in Figure 1. At each corner of the data cell several pieces of information may be available. In this case only the velocities at these positions are considered since the search is for a velocity structure. However, the same technique would be applicable to the search for structure in the passive contaminants; for example temperature or density.

The two components of velocity at each corner of the data cell, u_1, v_1, u_2, v_2, u_3, v_3, u_4, and v_4, are known by experiment. Decomposing these velocities into their component structures requires a model of those structures. A set of mutually orthogonal descriptors is shown in Figure 2a and consists of rotation, translation in each of two orthogonal directions, expansion in the same directions and shear. The mutually orthogonal descriptors are chosen because they are physically realistic. Other orthogonal descriptors could be chosen, as shown in Figure 2b. They are not included in the present technique because the present six descriptors appear to be sufficient from a physical point of view. It will be seen in the results that the six descriptors are adequate to identify the vortex structure. Attempts are currently underway to incorporate all eight descriptors and identify any potential improvement in the technique.

The model equation, in vector form, is

$$\overline{V} = X \, \overline{\beta} + \overline{\epsilon} \tag{1}$$

where

$\overline{V}$ ≡ velocity at the corners of the data cell

X ≡ matrix of computational weights

$\overline{\beta}$ ≡ parameters of rotation, translation, etc.

$\overline{\epsilon}$ ≡ error between the model and the measured velocities.

In expanded form the equation is,

$$
\begin{bmatrix} u_1 \\ v_1 \\ u_2 \\ v_2 \\ u_3 \\ v_3 \\ u_4 \\ v_4 \end{bmatrix}
=
\begin{bmatrix}
-A & 1 & 0 & -1 & 0 & B \\
-B & 0 & 1 & 0 & 1 & -A \\
-A & 1 & 0 & 1 & 0 & B \\
B & 0 & 1 & 0 & 1 & A \\
A & 1 & 0 & 1 & 0 & -B \\
-B & 0 & 1 & 0 & -1 & -A \\
A & 1 & 0 & 1 & 0 & -B \\
B & 0 & 1 & 0 & -1 & A
\end{bmatrix}
\begin{bmatrix} \beta_1 \\ \beta_2 \\ \beta_3 \\ \beta_4 \\ \beta_5 \\ \beta_6 \end{bmatrix}
+
\begin{bmatrix} \epsilon_1 \\ \epsilon_2 \\ \epsilon_3 \\ \epsilon_4 \\ \epsilon_5 \\ \epsilon_6 \\ \epsilon_7 \\ \epsilon_8 \end{bmatrix}
\qquad (2)
$$

The velocities are measured experimentally and are the data to be analyzed for coherent structure. The β vector consists of the modeled parameters shown in Figure 2. The matrix is composed of the computational weights which relate the flow model (Figure 2) to the actual measurements. The difference between the results of the model and the actual velocity measurements is attributed to an error represented by the $\overline{\epsilon}$ vector. Of course, if the model had eight coefficients instead of six, the result would be eight equations and eight unknowns. This would allow no room for error. However, this would only model the data, not the process because the actual data does have errors and only allows six physically realistic parameters as shown. The two additional degrees of freedom are incorporated into the non-zero error.

The matrix of computational weights is developed by observing the effect of each of the descriptors on the velocities in the data cell. The lengths of

of the sides of the rectangular data cell are A and B and, for example, the

velocity u_1, produced by the rotational component, β_1 is proportional to the

length of the side, A and is in the -X direction, hence the negative entry -A

in the first matrix entry. Likewise the effect due to rotation on the v_1

component is proportional to the side B and is also negative, hence the entry

-B in the first column, second row. The effect on u_1 due to the translation

in the same direction β_2 is directly proportional and therefore the entry 1

in column two, first row.

It should be noted that only the proportionality is of importance. The

exact relationship between the descriptors and the velocities is not critical

because that scale can be (and is) absorbed in the β values yet to be found

and that the objective here is to identify the spacial distributions of the

various descriptors in the hope that the distributions will clarify the flow

structure. That is, the objective here is to develop contours in space which

describe the various β terms. It is these contours which will define the

coherent structures and the numerical values associated with those contours

are not as important as the shape of the contours.

The Solution

The presentation of the solution will be in the form of spacial contour

maps which will then allow the identification and location of coherent

structures. The method of solution is based upon the fact that the optimum

values of the β parameters (i.e., those identified as the best fit of the model

to the data) occur when the error vector $\bar{\epsilon}$ is of minimum length. This, in

turn, requires that the error vector be orthogonal to the surface containing

all of the vectors $\bar{X}_n$ which compose the matrix of computational weights in

Eqn.(2). Therefore,[3]

$$\bar{X}'_1 \cdot \bar{\epsilon} = 0 \text{ and } \bar{X}'_2 \cdot \bar{\epsilon} = 0 \qquad (3)$$

or in general

$$X' \, \overline{\varepsilon} \approx 0 \tag{4}$$

But the error is the difference the actual measurements V and those which

would make the error zero $\hat{V}$, so

$$X'(V - \hat{V}) = 0 \tag{5}$$

but
$$\hat{V} = X\hat{\beta} \quad (since \ \overline{\varepsilon} = 0) \tag{6}$$

so
$$X'V - X'X\hat{\beta} = 0 \tag{7}$$

or
$$\hat{\beta} = (X'X)^{-1}X'V \tag{8}$$

where the 6 x 6 matrix, because the components are independent, yields

$$X'X = \begin{bmatrix} 4(A^2+B^2) & 0 & 0 & 0 & 0 & 0 \\ 0 & 4 & 0 & 0 & 0 & 0 \\ 0 & 0 & 4 & 0 & 0 & 0 \\ 0 & 0 & 0 & 4 & 0 & 0 \\ 0 & 0 & 0 & 0 & 4 & 0 \\ 0 & 0 & 0 & 0 & 0 & 4(A^2+B^2) \end{bmatrix} \tag{9}$$

If $A^2+B^2 = 1$ (which presents no problem since only relative values of

β are of importance) the inverse yields

$$(X'X)^{-1} = \begin{bmatrix} \tfrac{1}{4} & & & & & \\ & \tfrac{1}{4} & & & 0 & \\ & & \tfrac{1}{4} & & & \\ & & & \tfrac{1}{4} & & \\ & 0 & & & \tfrac{1}{4} & \\ & & & & & \tfrac{1}{4} \end{bmatrix} = \tfrac{1}{4} I \tag{10}$$

so

$$\hat{\beta} = \tfrac{1}{4} X'V \tag{11}$$

The matrix X and the velocity measurements v are known and $\hat{\beta}$ can be easily evaluated. Results for both synthetic flows and actual flows are presented in the following sections.

Synthetic Flow Results

In order to examine the contour plots of the orthogonal descriptors due to idealized flow fields, a synthetic vortex was created and subjected to the manipulation of Eqn. (11). The velocity distribution in the synthetic vortex is shown in Figure 3, where the velocity vectors are indicated.

By the methods described above, the contours for fixed values of β_n are shown in Figures 4-8 for various orthogonal descriptors. Figure 4 presents the contour map for the rotational component, β_1. As might be expected, most of the contour is rotationally symmetric and the most rapid changes in β values occur where the velocity changes are most rapid as seen in Figure 3. The deviations from rotational symmetry occur in regions of little change of magnitude and are caused by the fact that although the field is rotationally symmetric, as the rectangular data cell is moved through the field, the values it computes are symmetric about the center and the rectangular axes but cannot be entirely rotationally symmetric. This is due to finite difference representation of a rotational field by a rectangular grid.

The only place in the contour plot that presents a problem for the rectangular grid in that region where the velocity changes are small so contour lines are farther apart. In a real flow such a region would be unlikely and in fact would also be of little interest from the point of view of coherent structure. Thus the square grid presents no problem in terms of flow structure identification since coherent structures are invariably identified with large changes in flow properties, at least relative to their own scale.

The translation components, β_2 and β_3, produce rather interesting contours as shown in Figures 5 & 6 respectively. In each case a zero value contour passes through the synthetic vortex center and parallel to the direction of the translational velocity component in question. This is really a reflection of the fact that the vortex is perfectly symmetrical since it is synthetic and that the velocity field is fixed and not translating.

The contour for the expansion component in the horizontal direction, β_4, are shown in Figure 7 and result in a four lobe configuration. The contour plot for expansion in the vertical direction is rotated by 90° from that in Figure 7 and thus results in exactly the same plot. As in the previous Figures, the presence of the vortex leads to a very distinctive pattern.

The shear component, β_6, is plotted in Figure 8 and results in a contour map very similar to that observed for the expansion components but rotated by 45° about the center of the synthetic vortex. This is consistant with the fact that the maximum would occur in a plane inclined at 45° to the principal stress directions.

The contour plots described above, due to the synthetic vortex, will be the guide for the structure which can be identified in real flows based on the ability to recognize the appropriate patterns.

Real Flow Results

a. Vortex Structure near a Wall

An instantaneous flow field containing multiple vortices is described in Reference 4 and is produced by a cam shaped rotor which produces a vortex each time it rotates at the boundary of the flow field. The study of the vortex structure is motivated by some attractive potential applications of the rotor geometry.[5-7]

An example of the structure of the flow field produced by this method is shown in Figure 9. This field has been analyzed by the technique of Reference 2 to determine the vortex locations. In a frame of reference moving with the centers or the location of the two vortices found, the coherent structures may be seen in Figures 10 and 11, showing the upstream and downstream vortex structures respectively. It is the objective of the present method to identify the vortices more accurately, thereby allowing the use of the new technique to isolate even smaller structures in complicated flow fields.

The rotational orthogonal descriptor, β_1 of Figure 2, isolates the field of Figure 9 and is shown in Figure 12. According to the results of the synthetic vortex rotational component shown in Figure 4, the presence of a vortex structure is indicated by a closed contour with a maximum or minimum at its center (depending on the sign of rotation). In this case the rotational component clearly identifies two vortices, upstream and downstream. Each of the structures has a negative sign, indicating a clockwise rotation. The location of each vortex so identified coincides with the locations found by flow visualization and by a method of trial and error which consists of subtracting various translational velocities until an apparent vortex structure is evident.

In each case the locations of vortices are more accurate than those found by the technique of Reference 2. In addition the improved potential of the present technique is also evident in Figure 12 because not only the two major vortex structures are isolated but an additional vortex structure rotating in the opposite direction is evident in the lower center of the Figure. This vortex structure could not be identified by the previous technique described in Reference 2.

The fact that this small vortex structure actually exists is verified by the smoke flow visualization photograph of Figure 13, which shows only

approximately half of the field in Figure 12. The smoke streak lines verify the presence of the structure and also indicate the strength of the technique. The origin of the structure itself is believed to be due to the production at the rotor or to breeding by the larger vortex structure itself. It has been shown by Francis, et. al.[8,9] that under certain conditions a plate oscillating perpendicularly out of a wall can produce two vortices of the same sign for each cycle of the oscillation. A similar effect was found for the flow produced by the rotor of different velocity and length scales[10]. In this case, however, the smaller vortex is of opposite sign to the major vortex structure. Thus the breeding of a secondary vortex by the primary structure is a probability.

Looking back to the orthogonal descriptors of the synthetic vortex, the pattern produced by the stream wise translational descriptor, Figure 5, shows a line in the translational direction through the vortex center with closed contours above and below that position. Such a pattern is observed twice in the results of Figure 14; one is at the location of the upstream vortex, although only the upper lobe of the closed contours is evident. The other is at the location of the downstream vortex where, conversely, only the lower closed lobe is found.

It is of interest to note that the actual contour values in the case of the synthetic structure yield zero values on the line passing through the vortex center. When a vortex is translating through a flow field, a translational flow is superimposed on the vortex structure so that the vortex center lies essentially on an average value contour if the flow field without the vortex is approximately uniform. If the flow field, without the vortex, is still rapidly varying then this need not be the case.

Translation in the orthogonal direction can also be employed to locate

vortex centers as shown in Figure 15. As in the case of the synthetic vortex

(Figure 6) the structure is a vertical line passing through the vortex center

with the value of the contour roughly equal to the average value if the field

without the vortex is relatively uniform. As in Figure 14, the downstream vortex

is not found as easily due to the fact it is more diffuse and less concentrated.

There is a possibility that additional information may be extracted from the

field in terms of the direction of translation of the structure. Further

analysis is proceeding along these lines.

For both the stream wise and transverse expansion descriptors, Figures

16 and 17, the pattern for the vortex location should be similar to that produced

in Figure 7 for the synthetic vortex. Three-fourths of this structure is found

in the upstream vortex of the contour plots of Figures 16 and 17. The missing

lobe is the upstream one farthest from the wall, although there is some evidence

of it in Figure 16 and more indication in Figure 17. The reason for this

apparently missing piece of contour is probably due to the flow <u>over</u> the

vortex structure, due to the fact that the structure is moving at a velocity

less than that of the free stream velocity far from the wall.

The structure is extremely weak for the downstream vortex and suggests

the possibility for using this technique to quantify the strength of the vortex.

More test cases will be required to calibrate the technique and the effect of

a non uniform flow on which the vortex flow is convected.

In a similar manner, the shear flow descriptor also adequately describes

the upstream vortex location but not the downstream vortex. The position of

the lobes is rotated by 45° so they no longer lie in the quadrants but rather

on the axes. Again, three out of four lobes are present in the upstream vortex

but the downstream vortex is not evident.

Thus in the real flow case the most useful descriptor appears to be the rotational component, Figure 12. The rotational contour is capable of locating not only the concentrated upstream vortex but also the weaker downstream vortex. The usefulness of the other descriptors (in addition to isolating the rotational descriptor) is yet to be determined.

b. Vortex Structure in a Jet

The typical instantaneous velocity field of an oscillating jet is shown in Figure 19. These flow fields have been shown to contain convected large scale structures, an example of which is shown in Figure 20. The present objective is to isolate those structures more precisely and in a manner which will allow the identification of smaller structures.

Applying the same orthogonal descriptor technique discussed in earlier sections results in the identification of two vortex structures as shown by the contours of the rotational orthogonal descriptor in Figure 21. The upper and larger of the two vortices is approximately three times as strong as the lower vortex. The upper vortex has been found by other methods, i.e. the method of Reference 2 and the visual technique of subtracting stream wise velocity and observing the flow structure in essentially different frames of reference. In addition, the vortex structures have been observed in the experimental case by smoke flow visualization. The lower weaker vortex has been identified by none of these techniques.

The stream wise translation orthogonal descriptor is shown in contour form in Figure 22. As was the case in the synthetic vortex and in the rotor flow field as well, the translational contours appear to follow the general direction of convection of the large structure itself. The transverse translational component, Figure 23, clearly indicates a zero transverse velocity contour which is easily verified by the velocity vector field of Figure 19.

The expansion components in the two perpendicular directions are shown in Figures 24 and 25 and do not yield much information as to coherent structure. The lack of identifiable structure is probably related to the weakness of the vortices relative to those found in the case of the rotor flow field previously described. The same is true of the shear orthogonal descriptor whose contours are shown in Figure 26.

Expanded Use of the Present Technique

The data cases discussed in the present treatment all involved spacial distributions of data. One could also extract information from a set of fixed probes in a flow field (in particular a boundary layer as in Figure 27). The continuous signals generated by these probes with time are shown schematically in Figure 28 for two components of velocity from each of the three probes. The actual velocity change with time will depend upon the strength and location of any vortices convected throug the field. With a sufficient number of probes (where sufficient is not yet defined) the continuous field can be degenerated into a grid which is equivalent to those in Figures 3, 9, and 19.

Thus the temporal data can be analyzed in the same fashion and by the same technique as the data treated in the present case. This would then allow the determination of the vortex or large scale structure in a flow field and would allow the identification of that structure by a small number of variables.

Conclusions

The data analysis method developed in Reference 2 was successful in the identification of large scale coherent flow structures. However, additional accuracy was desired from the point of view of a technique which is capable of isolating small structures which would otherwise escape

detection. Identification of these smaller structures then offers the possibility the temporal data, as opposed to spacial data, can also be analyzed to determine the vortex structures being convected in a boundary layer. The smaller scale structures can now be found. The temporal data case is currently being examined.

References

1. Lugt, H., "The Dilemma of Defining a Vortex", in _Recent Developments in Theoretical and Experimental Fluid Mechanics_, Muller, Roesner and Schmidt (eds.), Springer-Verlag, Berlin-Heidelberg, 1979.

2. Bethke, R. J. and Viets, H., "Data Analysis to Identify Coherent Flow Structures", AIAA Paper 80-1561, AIAA Atmos. Flight Mech. Conf., Danvers, Mass., Aug. 1980.

3. Box, G.E.P., Hunter, W.G. and Hunter, J.S.,"Statistics for Experimenters", John Wiley, New York, 1978.

4. Viets, H., Piatt, M. and Ball, M., "Forced Vortices Near a Wall", AIAA Paper No. 81-0256, Aerospace Sciences Mtg., St. Louis, MO., Jan 1981.

5. Viets, H., Piatt, M. and Ball, M., "Unsteady Wing Boundary Layer Energization", AIAA Paper No. 79-1631, AIAA Atmospheric Flight Mechanics Conf., Boulder, Colo., Aug. 1979.

6. Viets, H., Piatt, M. and Ball, M. "Boundary Layer Control by Unsteady Vortex Generation", J. Wind Eng. and Indust. Aero., Vol. 7, 1981, pp. 135-144.

7. Viets, H., Ball, M. and Bougine, D., "Performance of Forced Unsteady Diffusers", AIAA Paper No. 0154, Aerospace Sciences Mtg., St. Louis, Mo., Jan 1981.

8. Francis, M.S., Lang, J. D., and Keesee, J. E., "Water Tunnel Measurements of Unsteady Separation", A.F.S.C. Report SRL-TR-78-0011, Dec. 1978.

9. Francis, M.S., Keese, J. E., Lang, J. D., Sparks, G. W., Jr., and Sisson, G. E., "Aerodynamic Characteristics of an Unsteady Separated Flow", AIAA Journal, Vol. 17, No. 12, Dec. 1979, pp. 1332-1339.

10. Viets, H., Catalano, G. and Ball, M., "Vortex Production Near the Back of an Automobile or Van", in preparation.
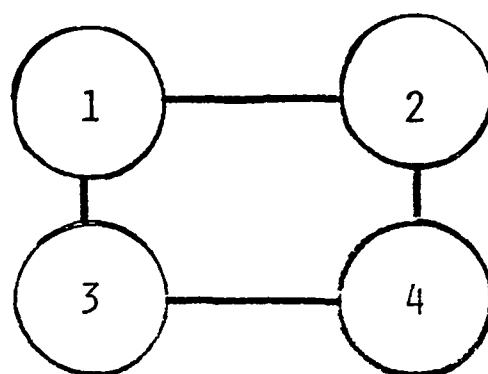
Figure 1. The data cell.

Symbol

β_1 rotation
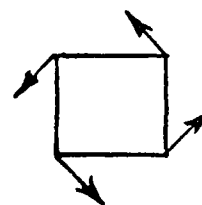
β_2 translation
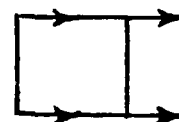
β_3 translation
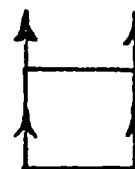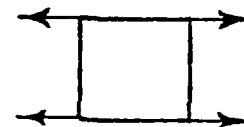
β_4 expansion

β_5 expansion
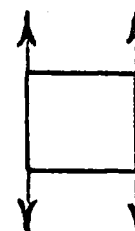
β_6 shear
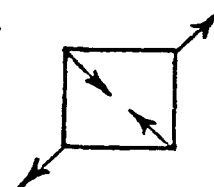
Figure 2a.   Orthogonal Descriptors included
in the present model.
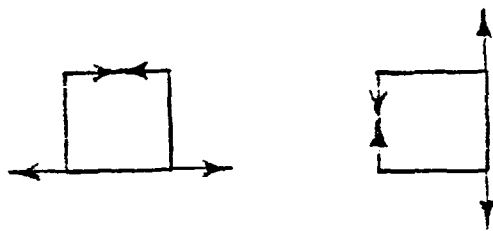
Figure 2b.   Orthogonal Descriptors not included
in the present model.
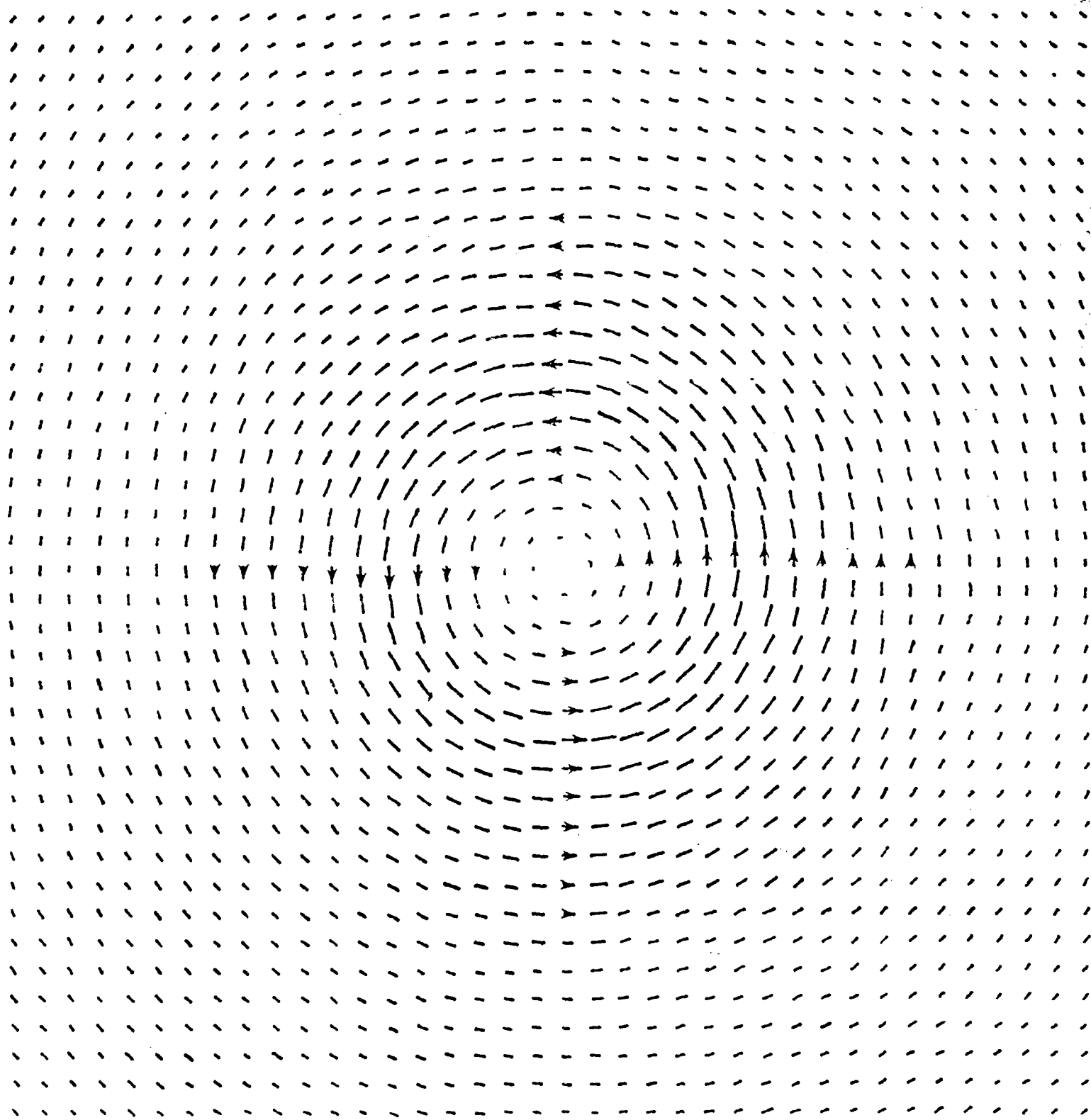
Figure 3. Velocity distribution in the synthetic vortex.
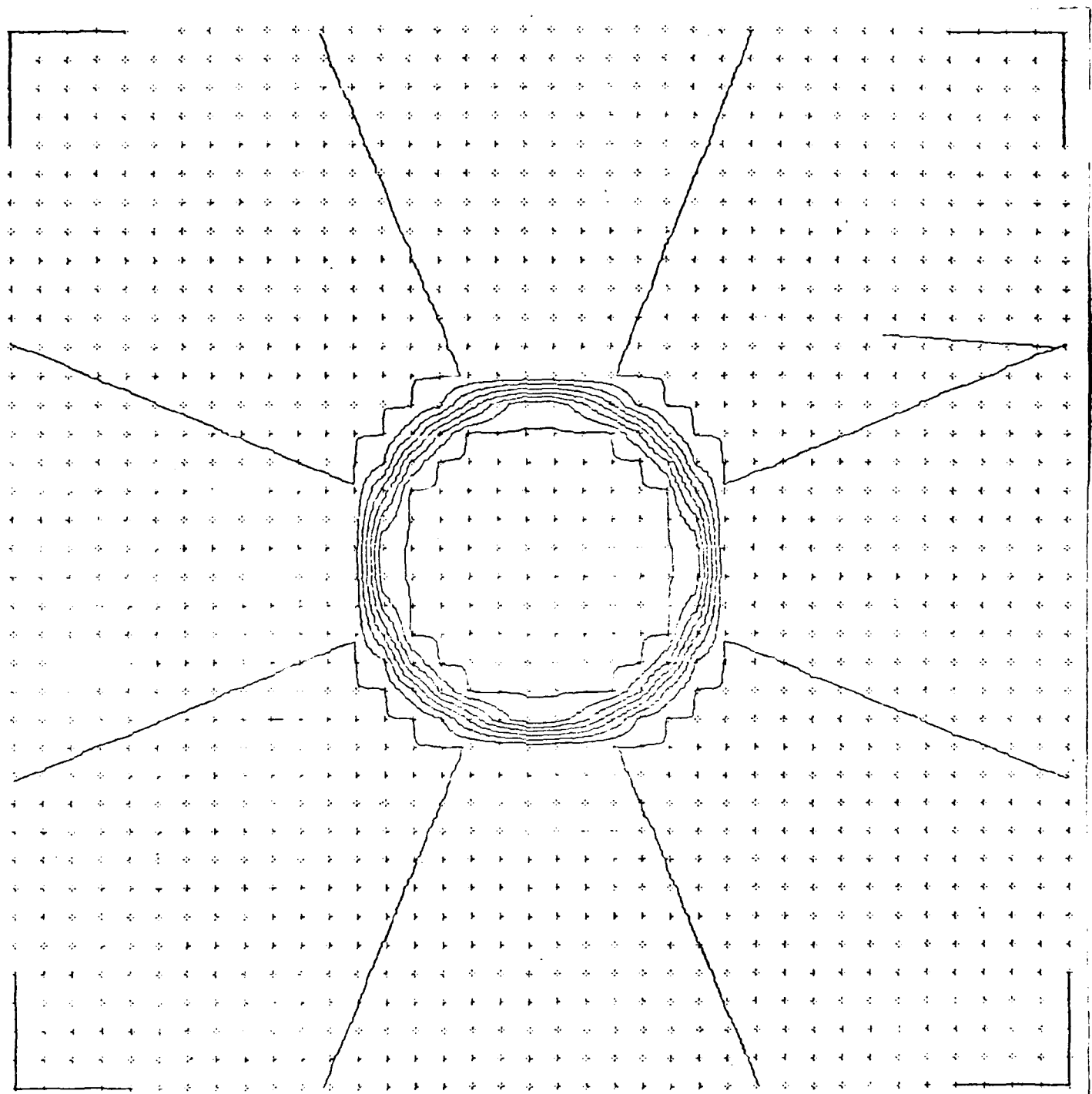
Figure 4. Rotational Component of Orthogonal
Descriptors for the synthetic Vortex.
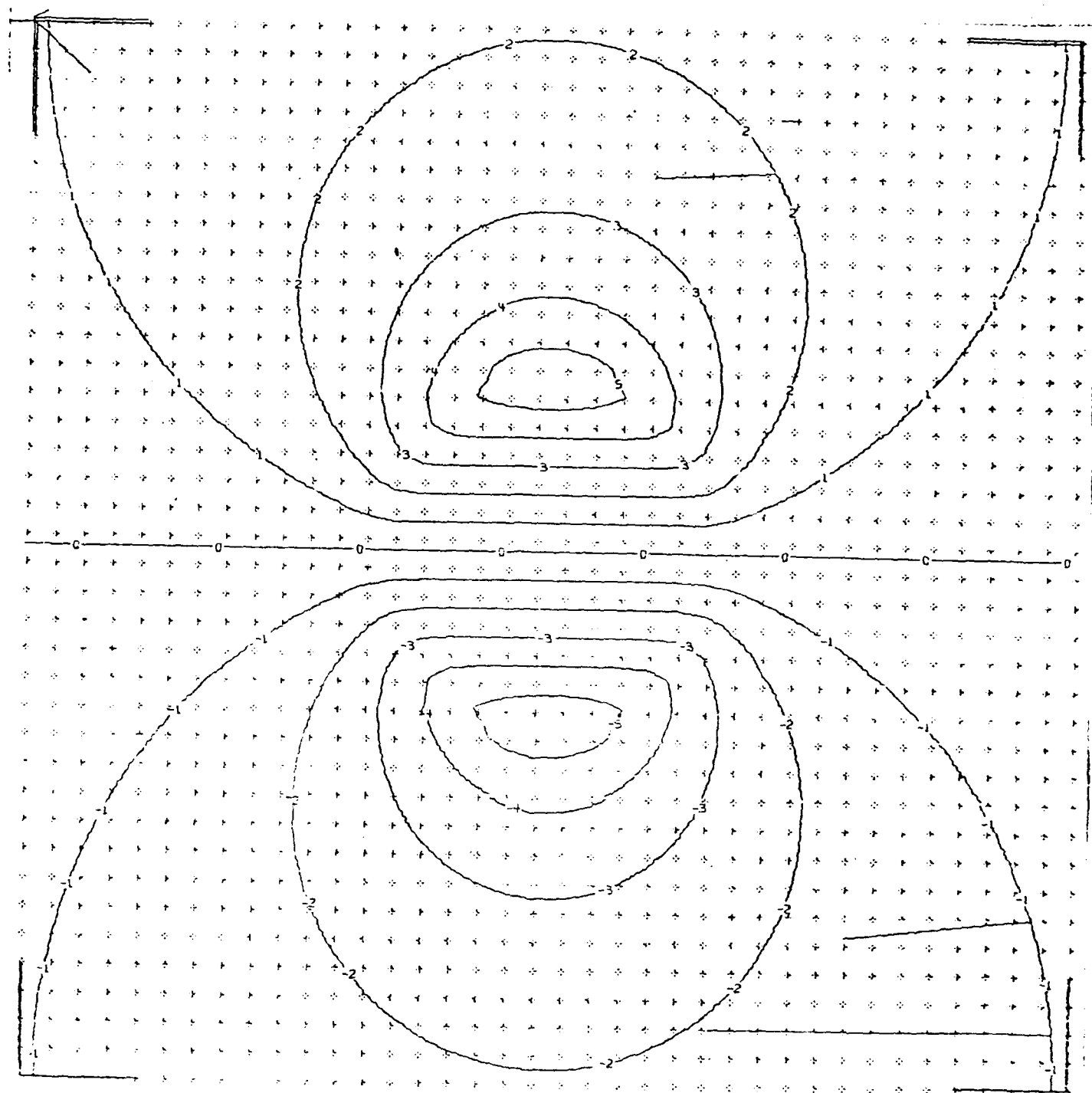
Figure 5. *Stream wise Translational Component of the Orthogonal Descriptors for the Synthetic Vortex*
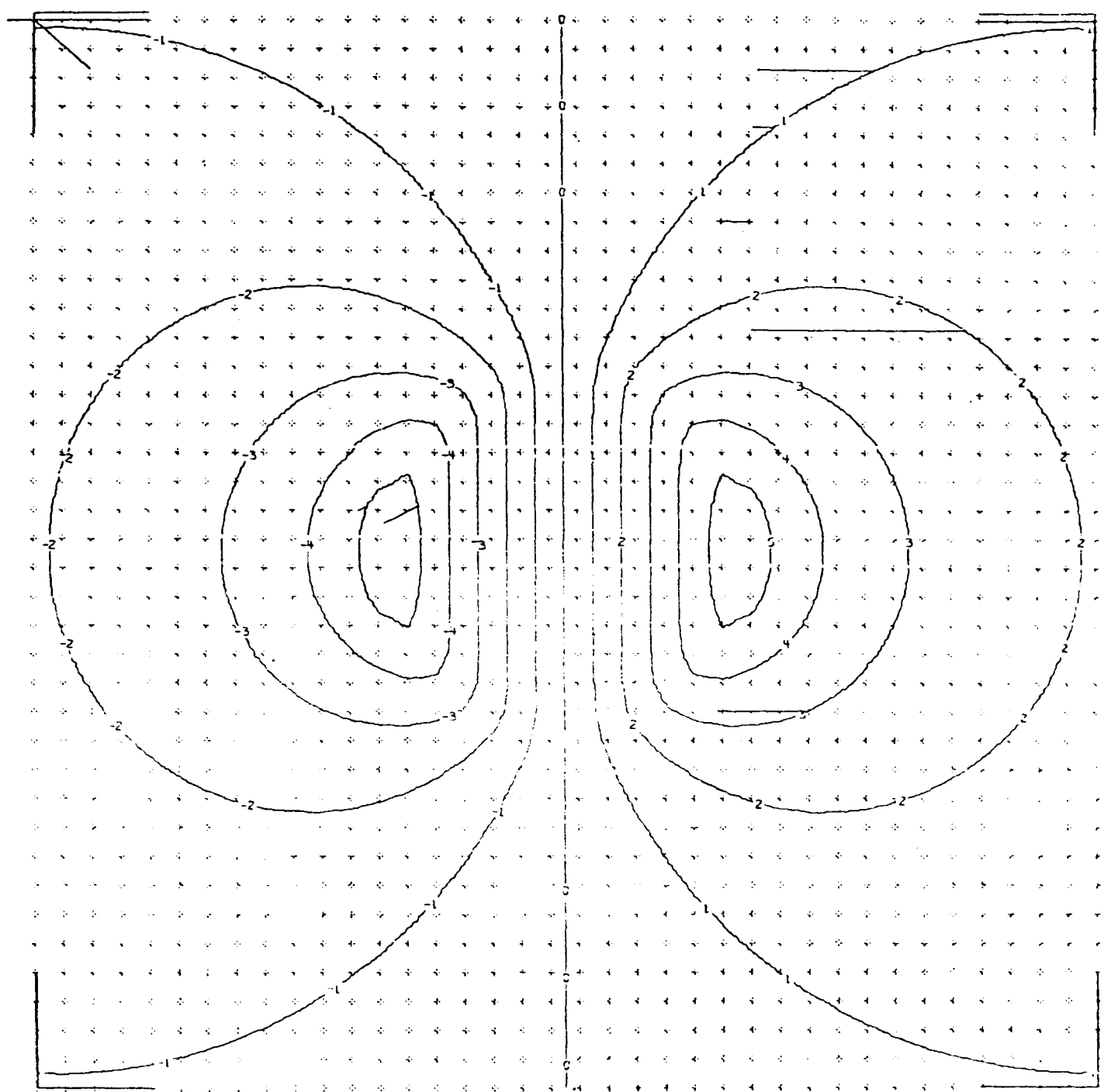
Figure 6. Transverse Component of the Orthogonal
Descriptors for the Synthetic Vortex
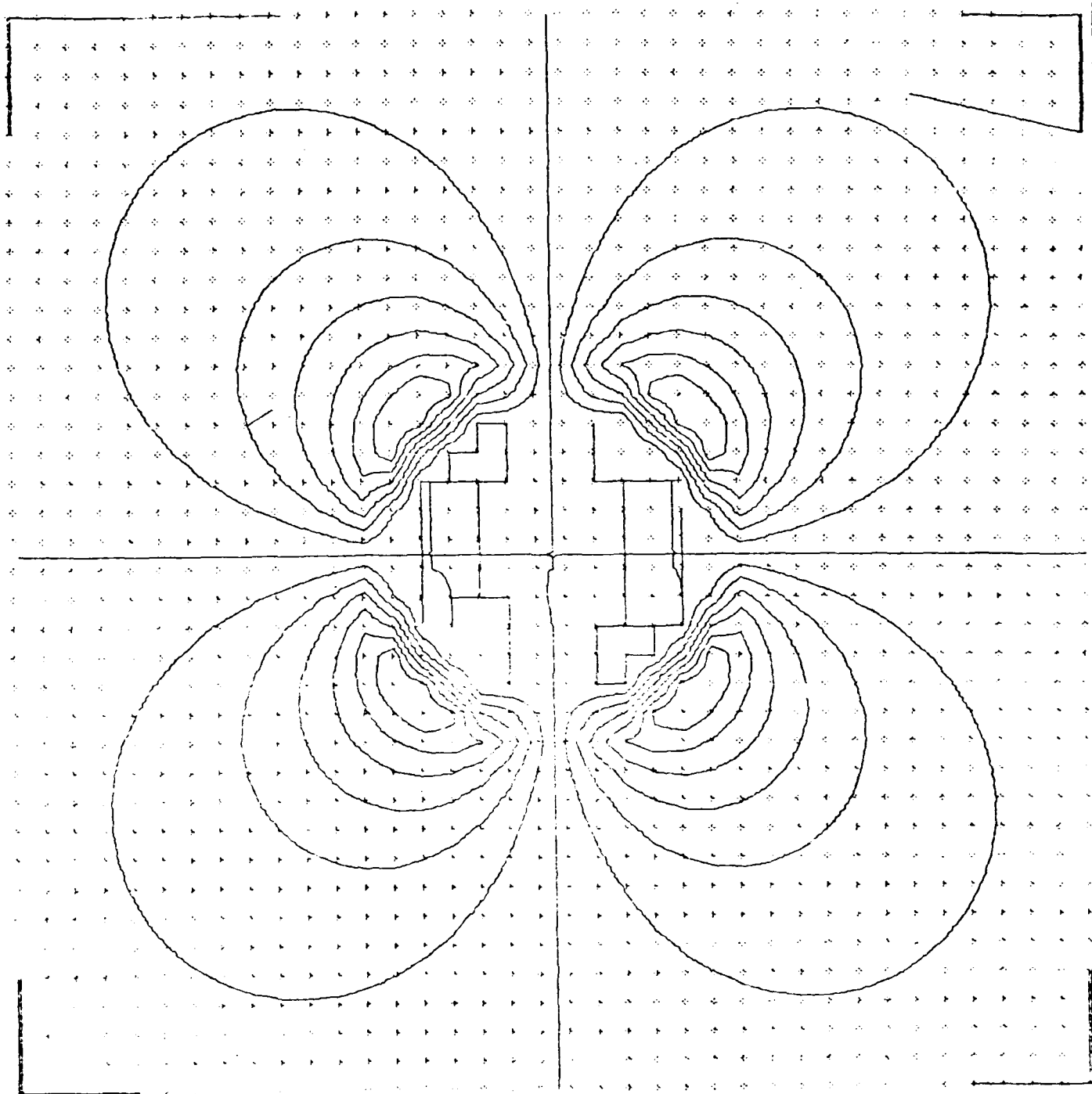
Figure 7. Stream wise Expansion Component of the Orthogonal
Descriptors for the Synthetic Vortex
(same as the transverse component)
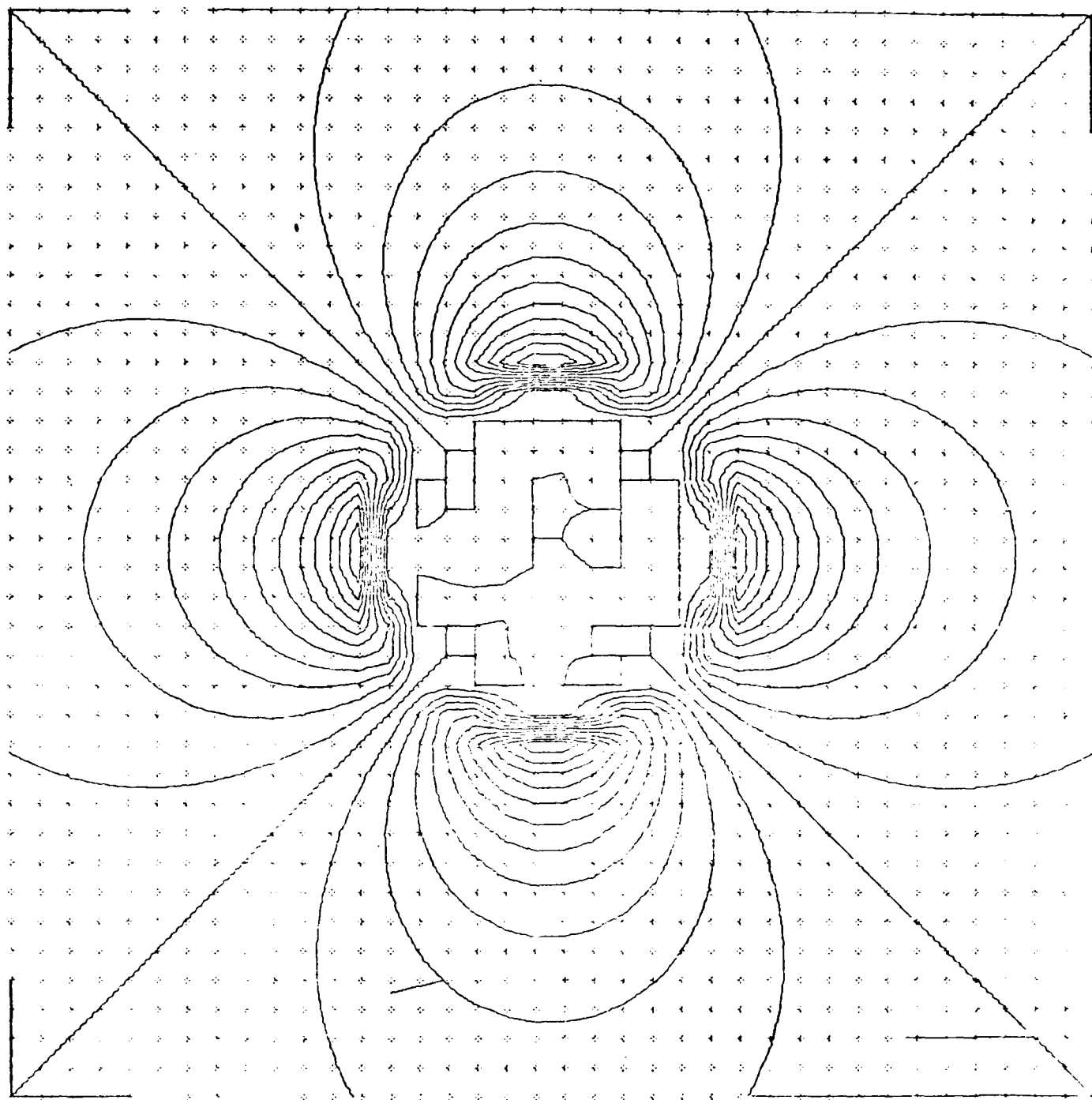
Figure 8. Shear Component of the Orthogonal
Descriptors for the Synthetic Vortex
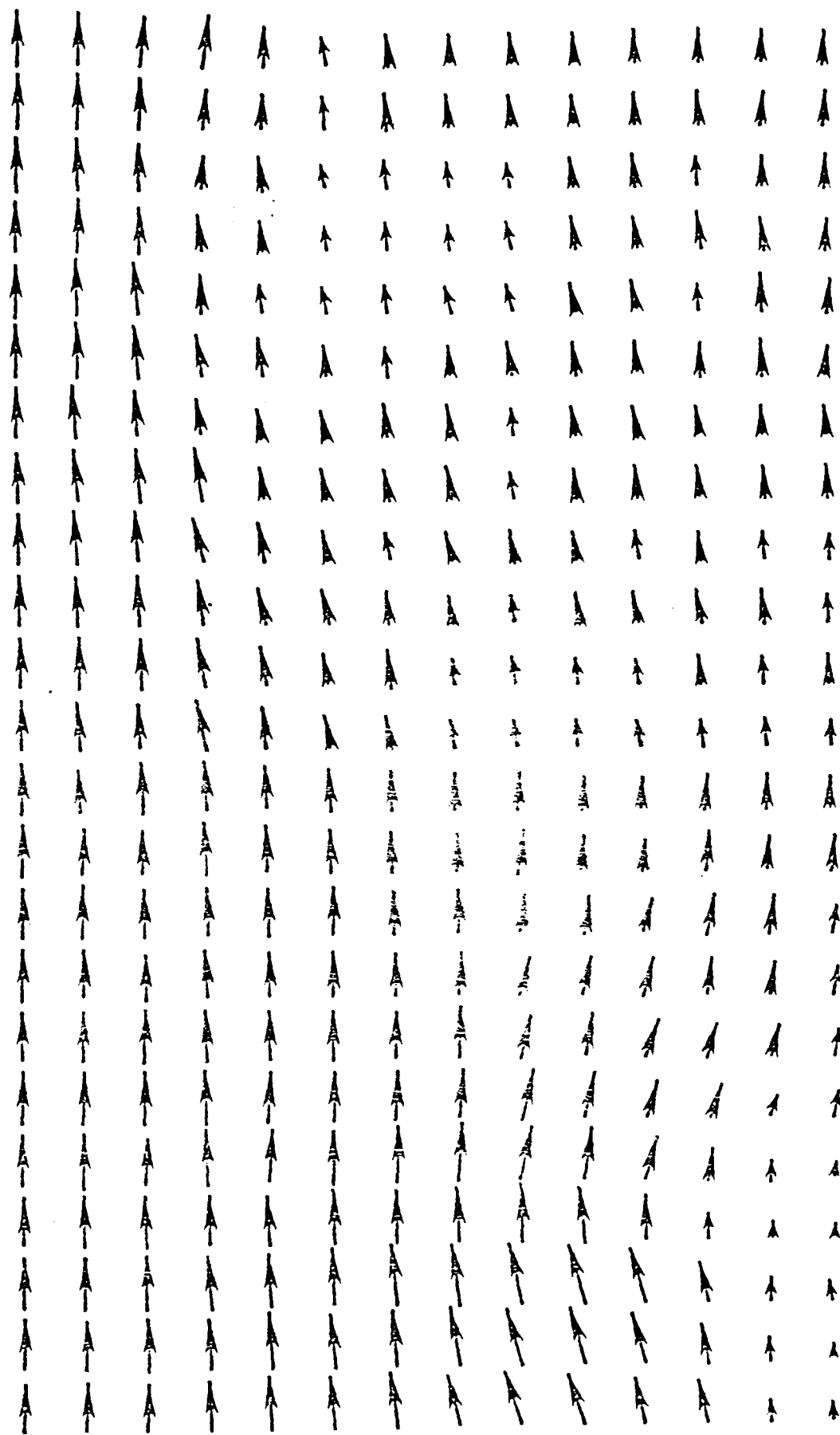
Figure 9. Flow field produced by the rotor.
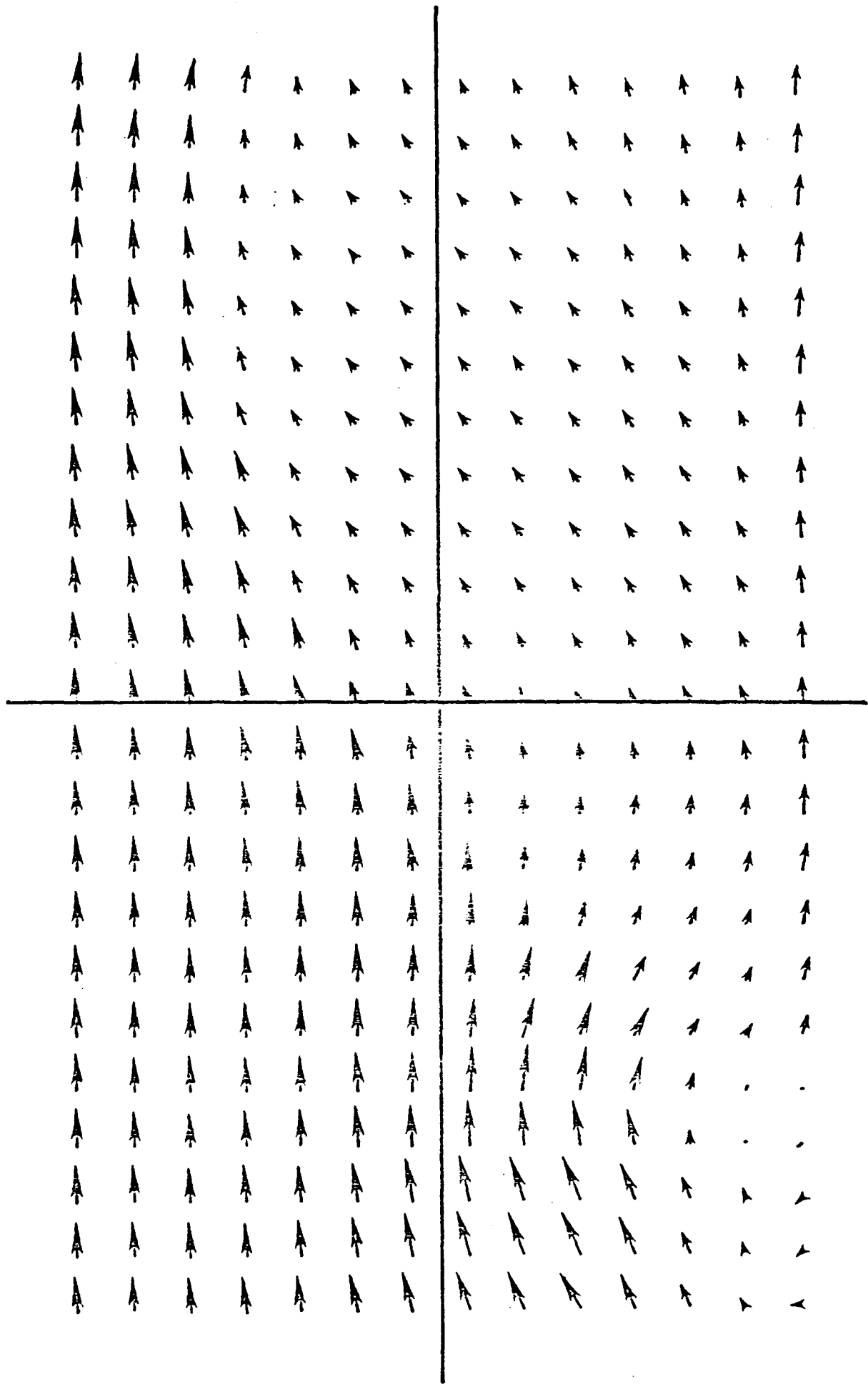
Figure 10. Structure of Upstream Vortex by Technique of Ref. 2.
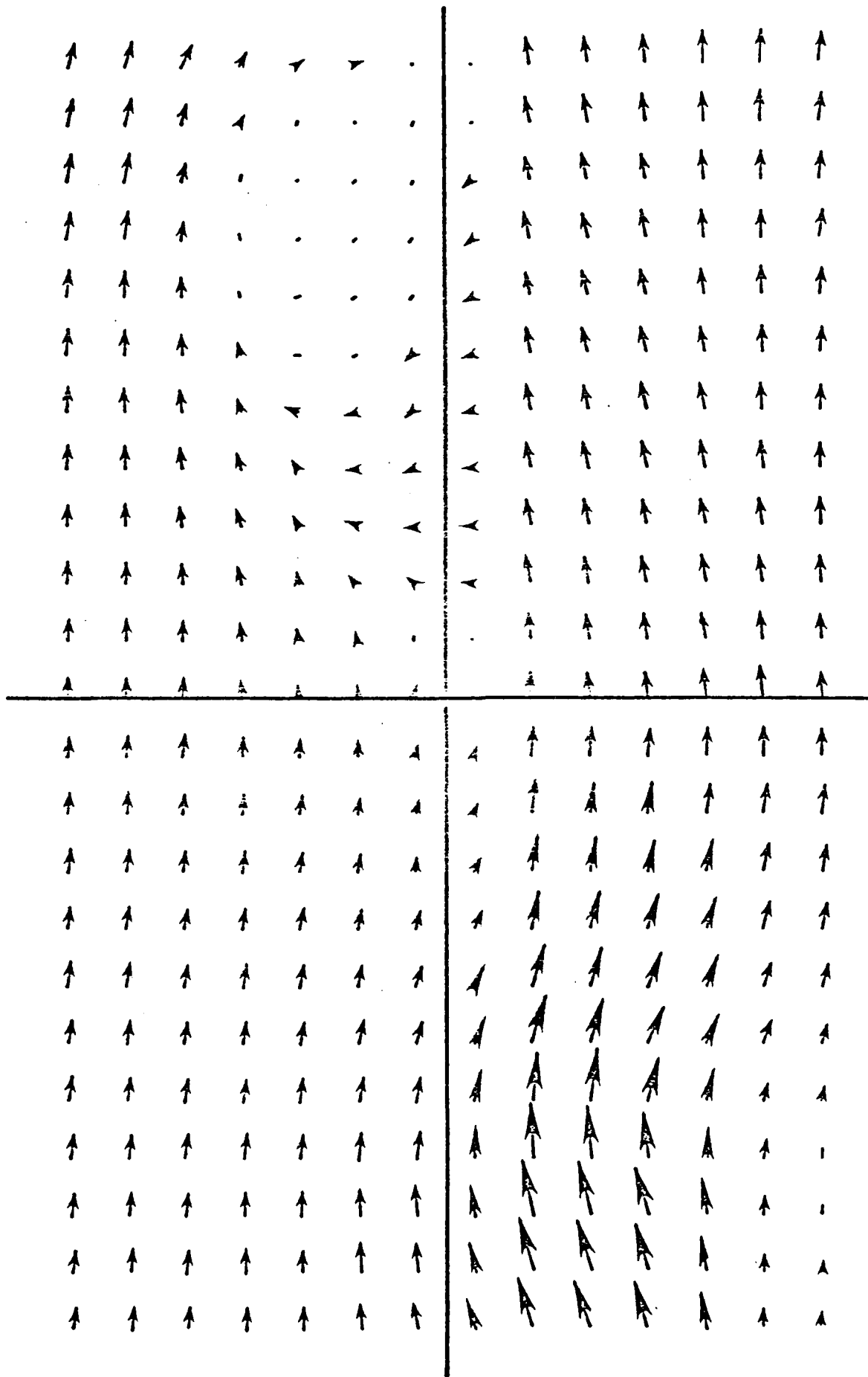
Figure 11. Structure of Downstream Vortex by technique of Ref. 2.
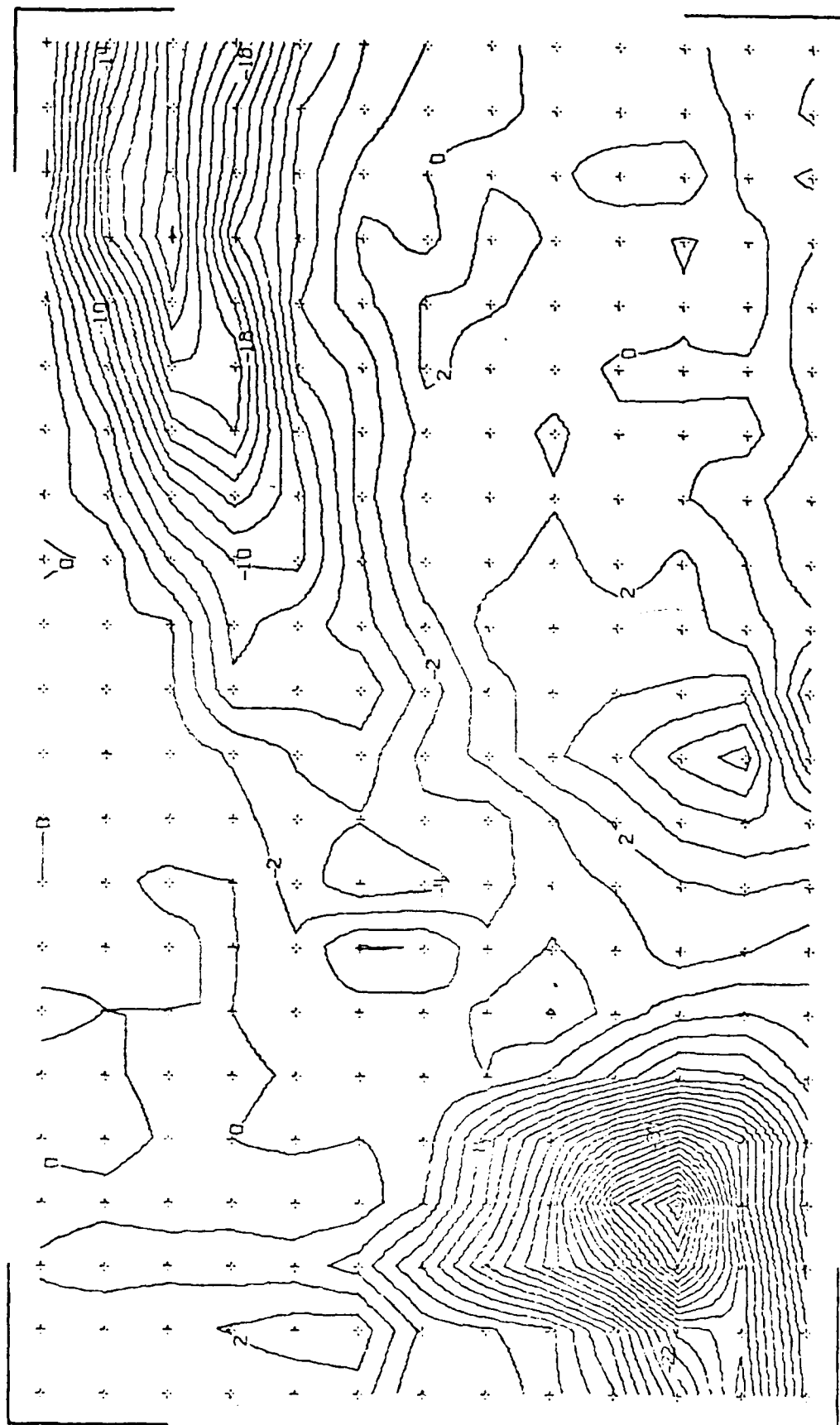
Figure 12. Rotational Descriptor for the Rotor Flow field.
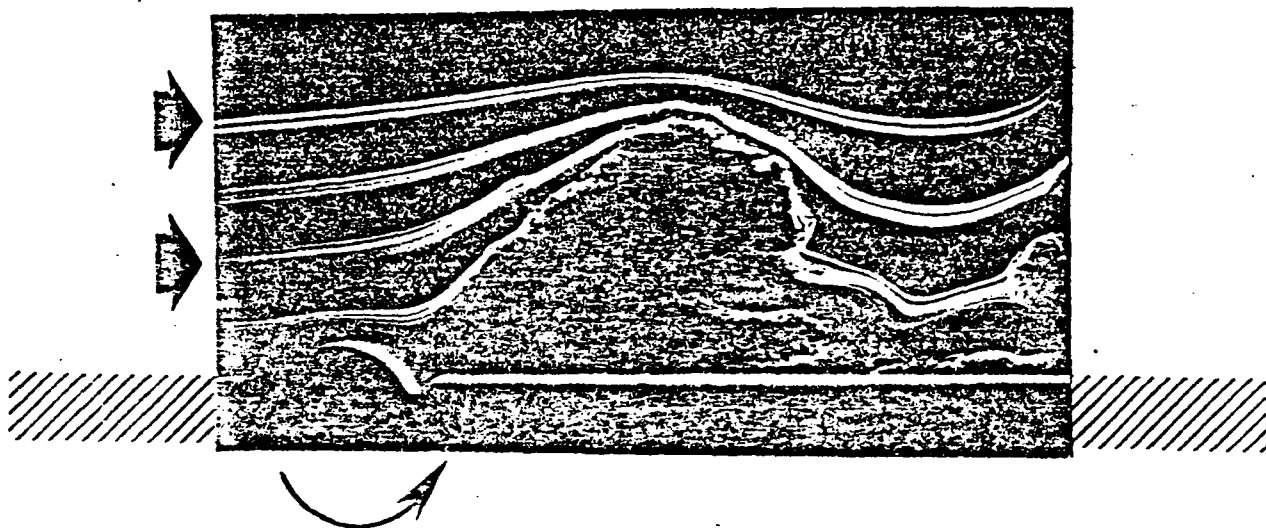
$$\omega = +3000 \text{ rpm}$$

Figure 13. Smoke flow visualization
of the rotor flow field
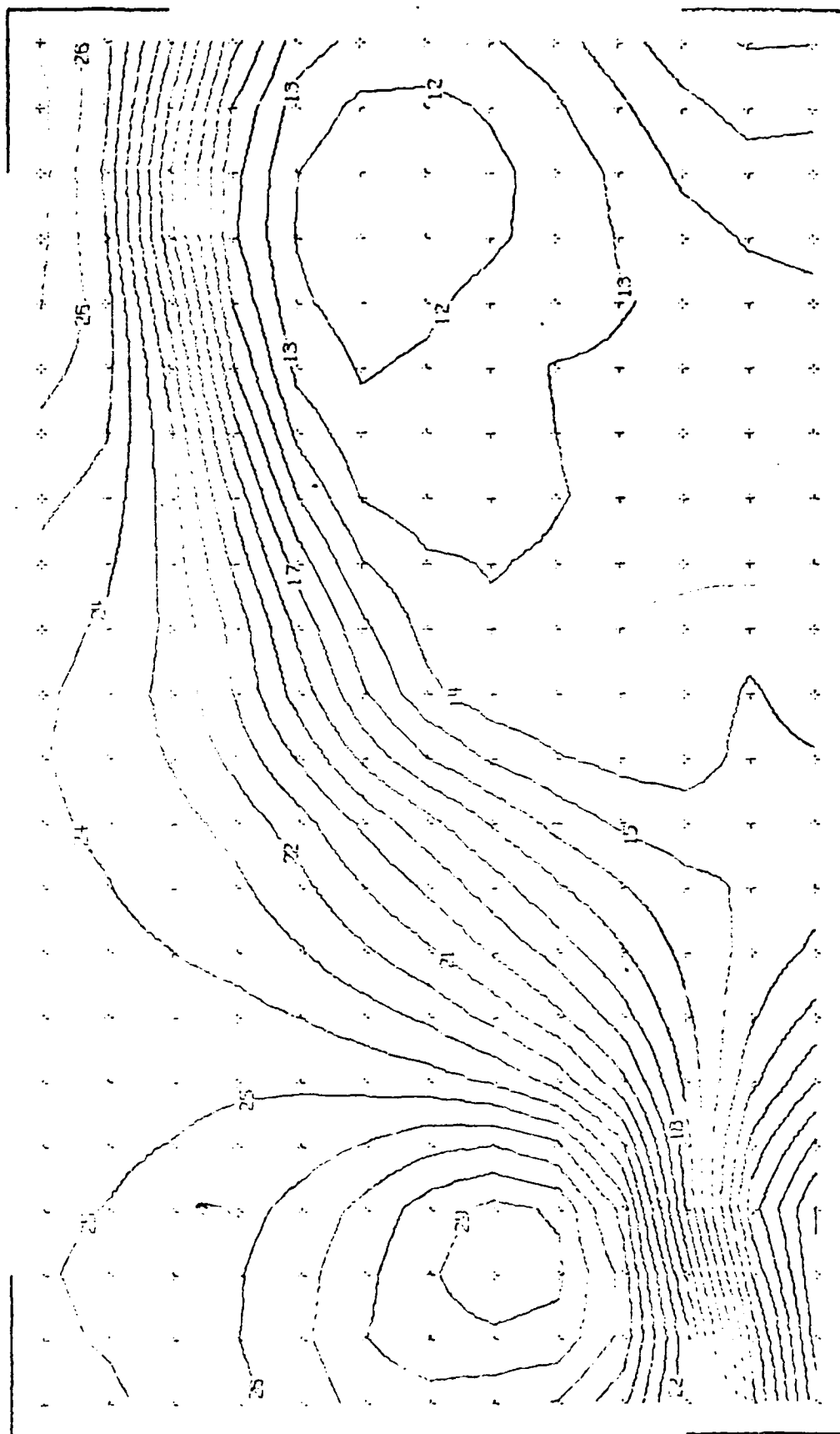
Figure 14. Streamwise translation descriptor for the rotor flow field.
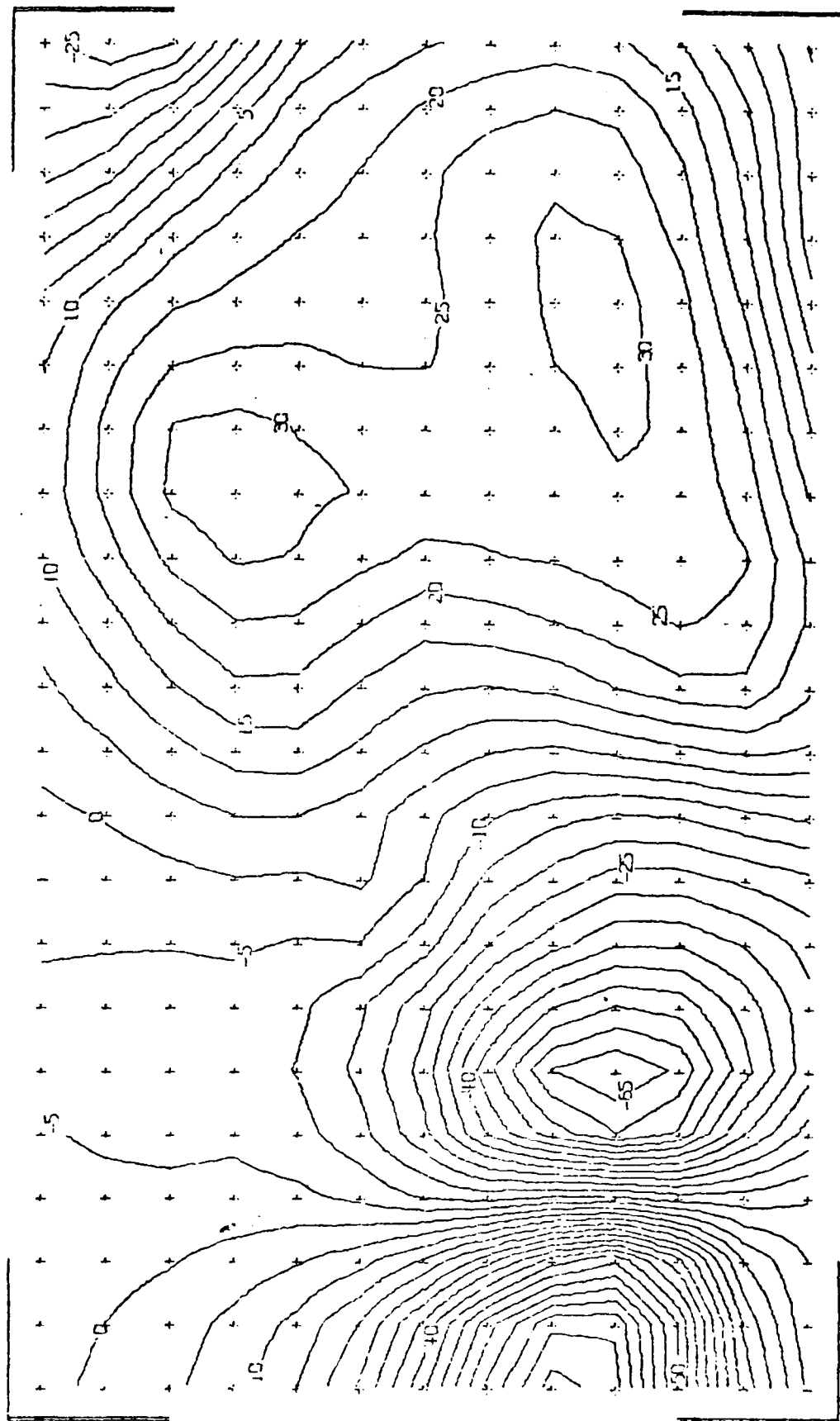
Figure 15. Vertical translation descriptor for the rotor flow field.
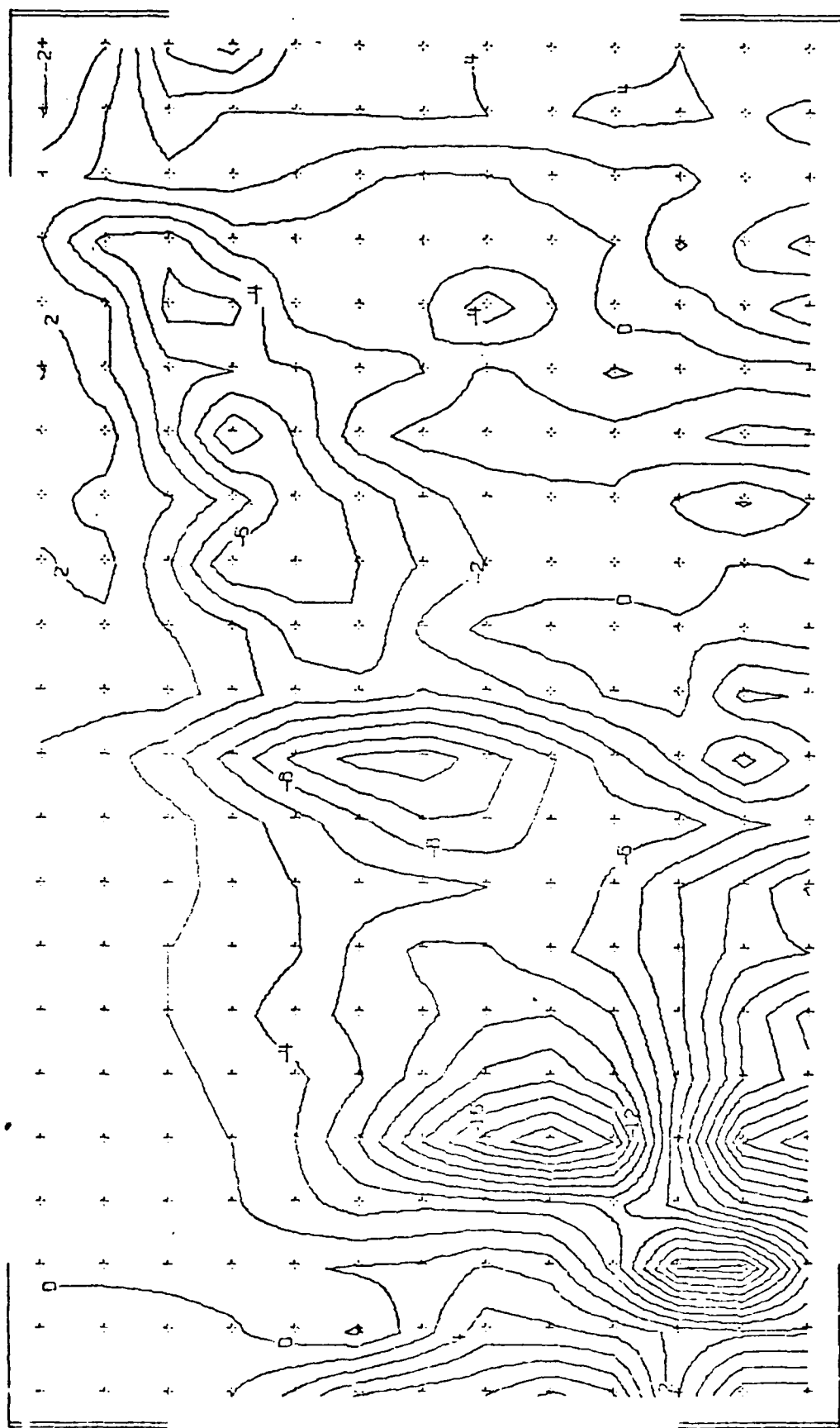
Figure 16. Stream wise expansion descriptor for the rotor flow field.
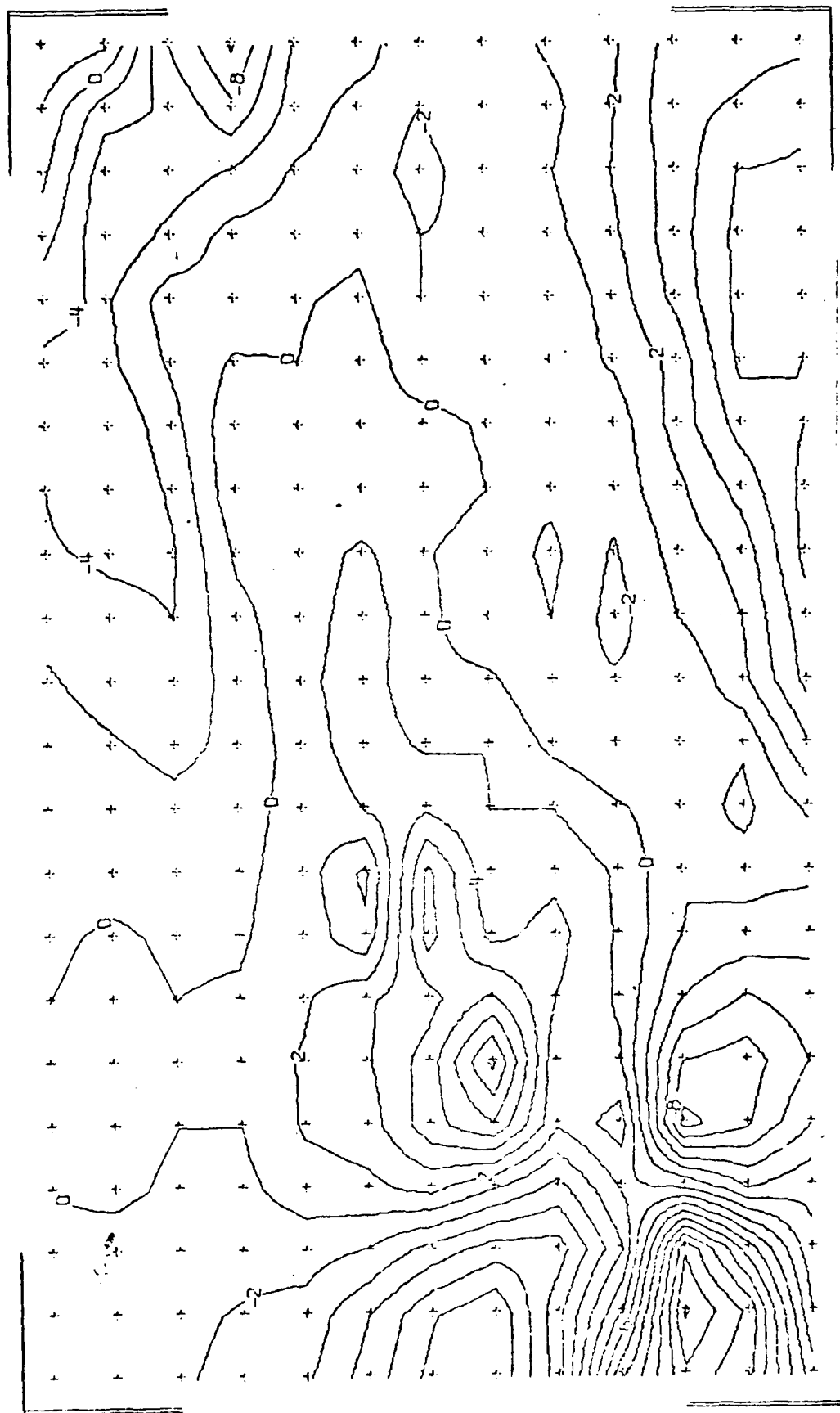
Figure 17. Transverse expansion descriptor for the rotor flow field.
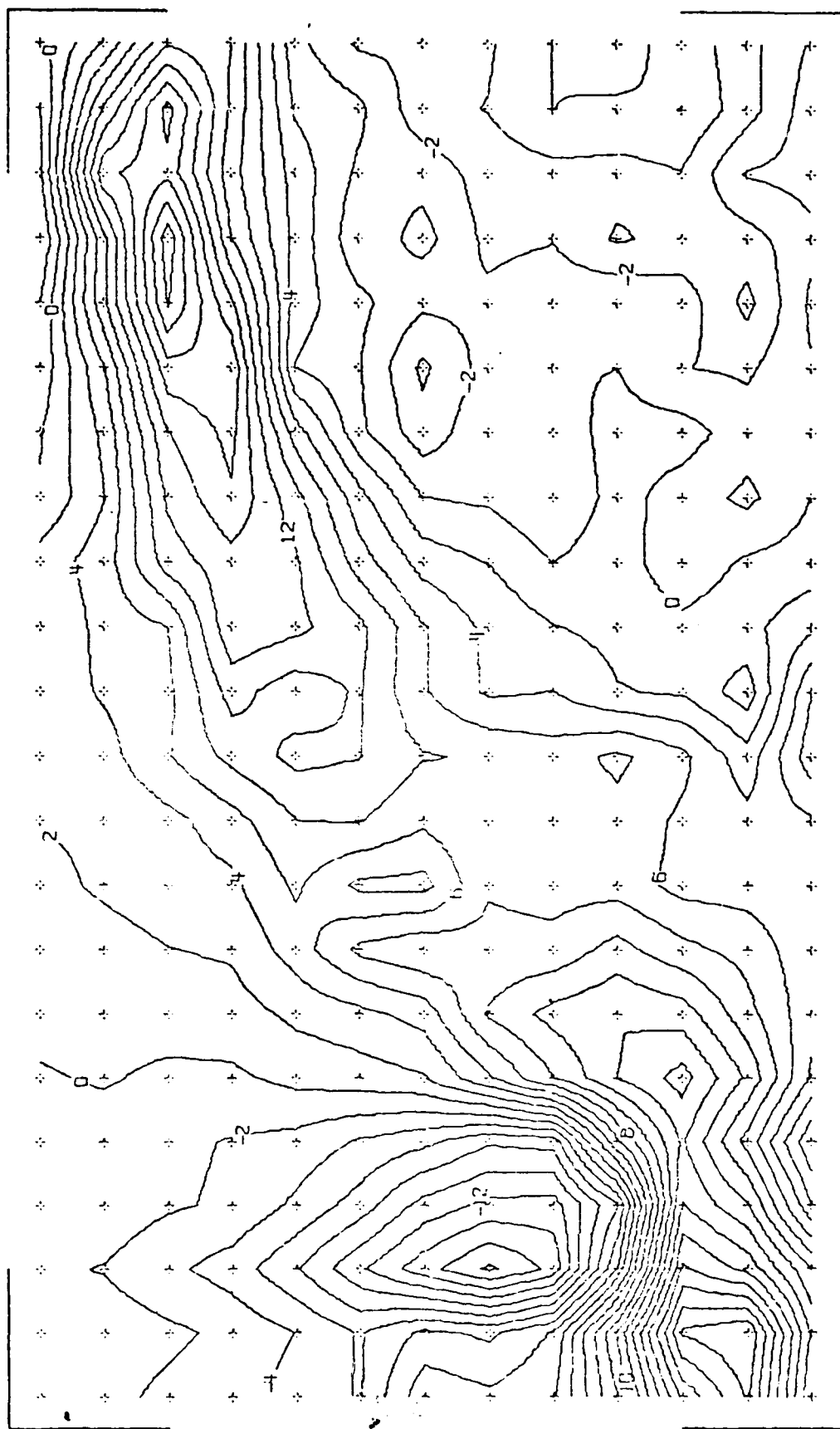
Figure 18. Shear flow descriptor for the rotor flow field.
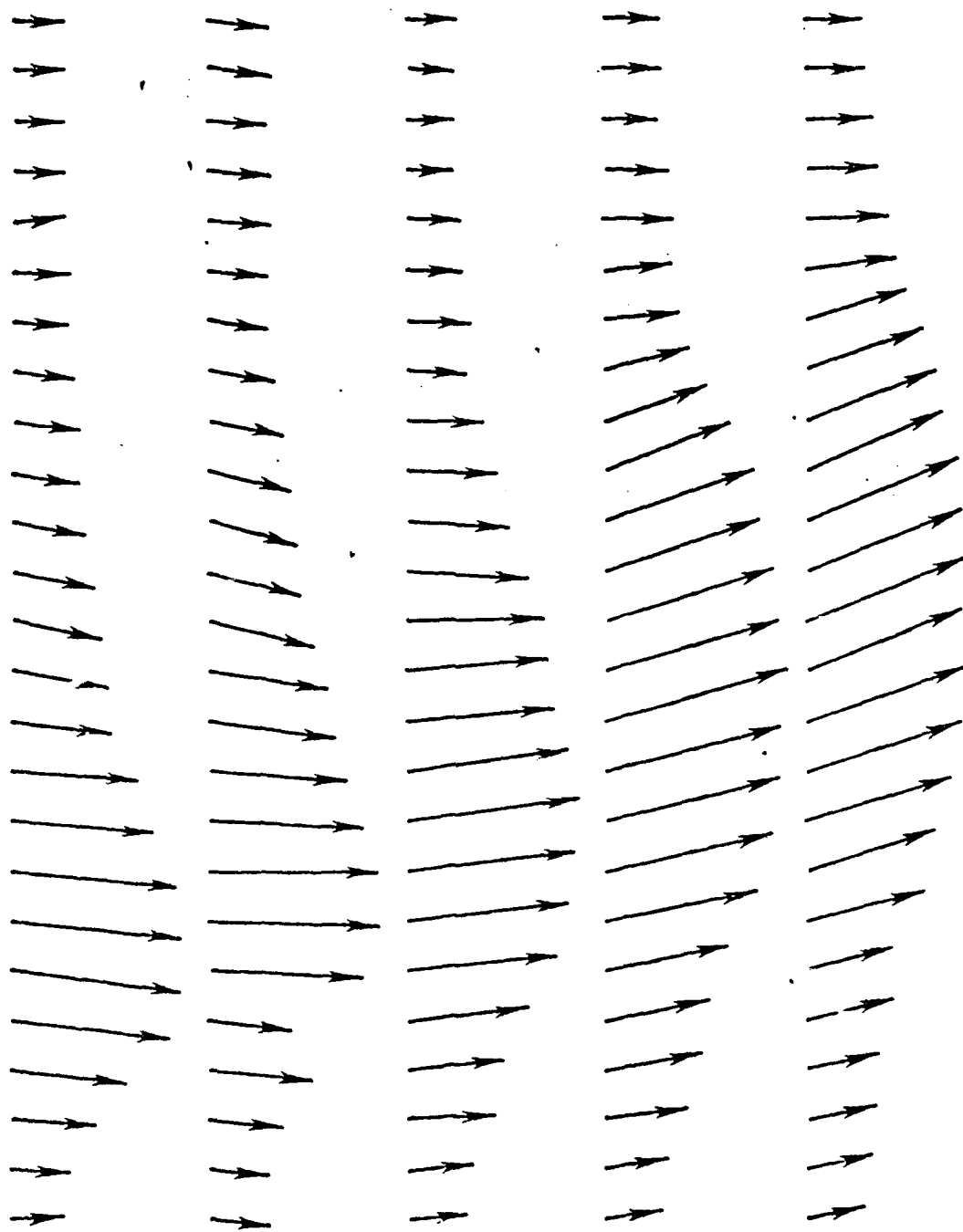
Figure 19. Typical instantaneous flow field in an oscillating jet.
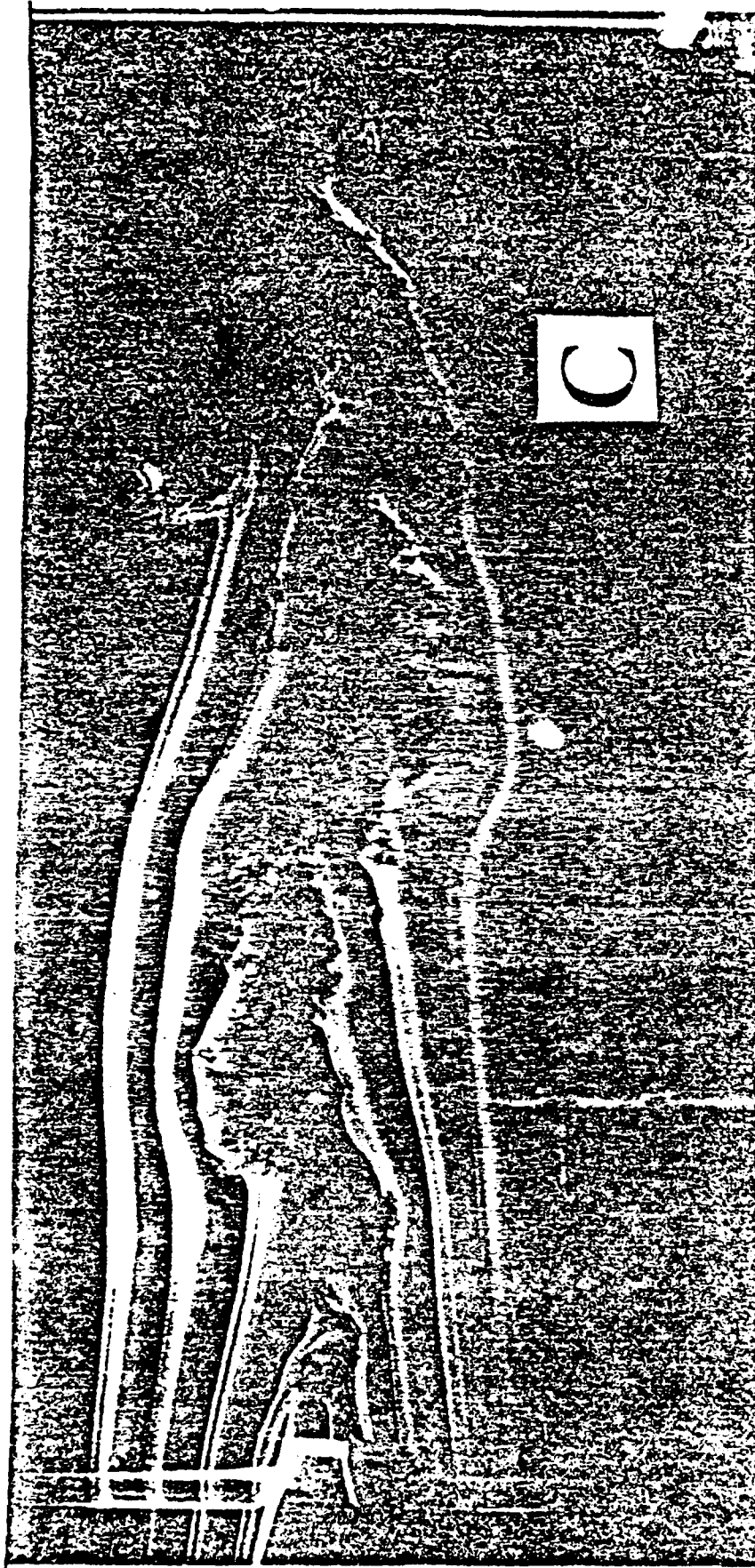
Figure 20. Smoke flow visualization of a vortex
in the oscillating jet (over c)
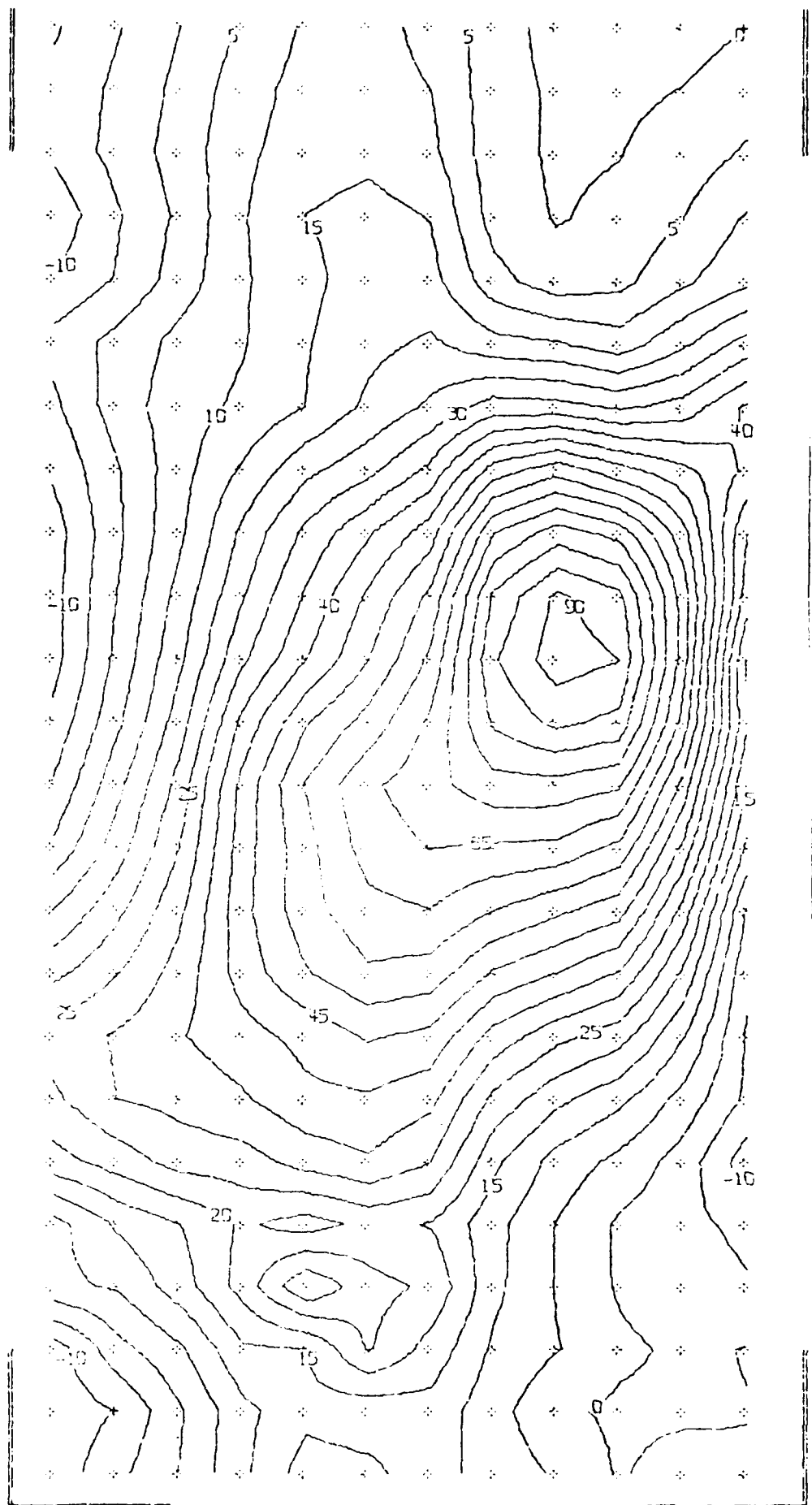
Figure 21. Rotational orthogonal descriptor for an unsteady jet flowfield.
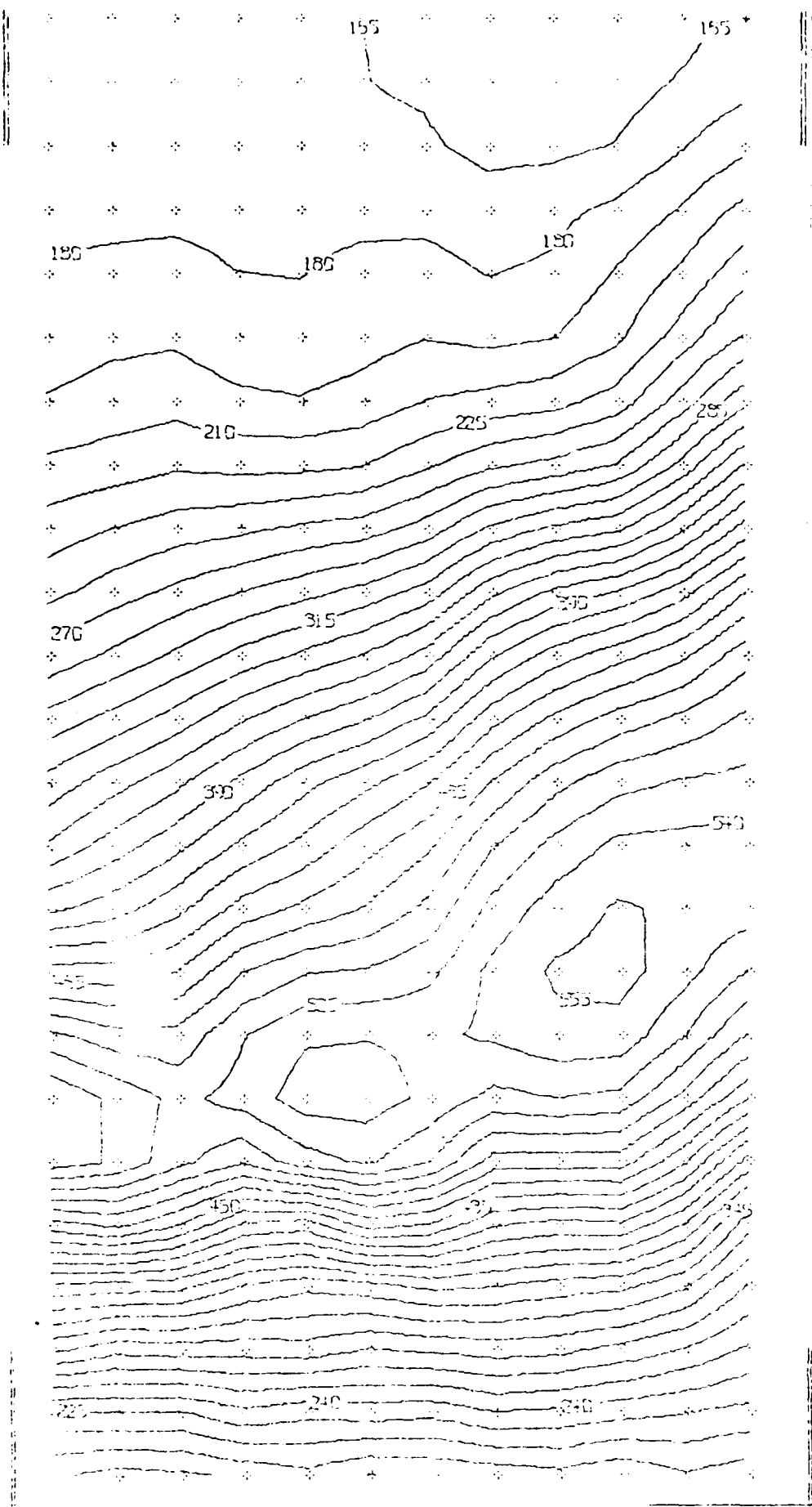
Figure 22. Streamwise translation orthogonal descriptor in
an unsteady jet flowfield.
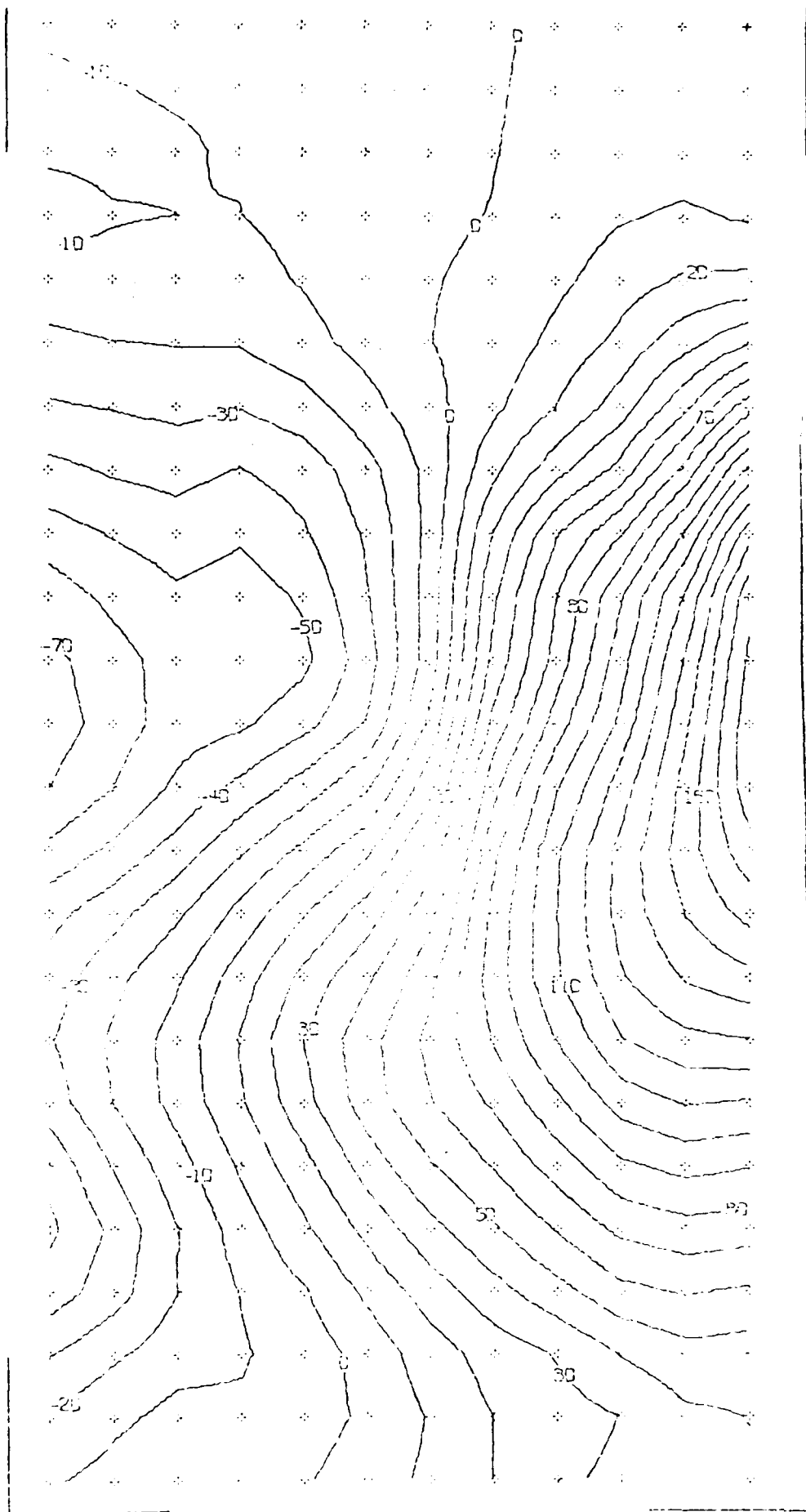
Figure 23. Transverse component of the translational velocity
orthogonal descriptor for an unsteady jet flowfield.
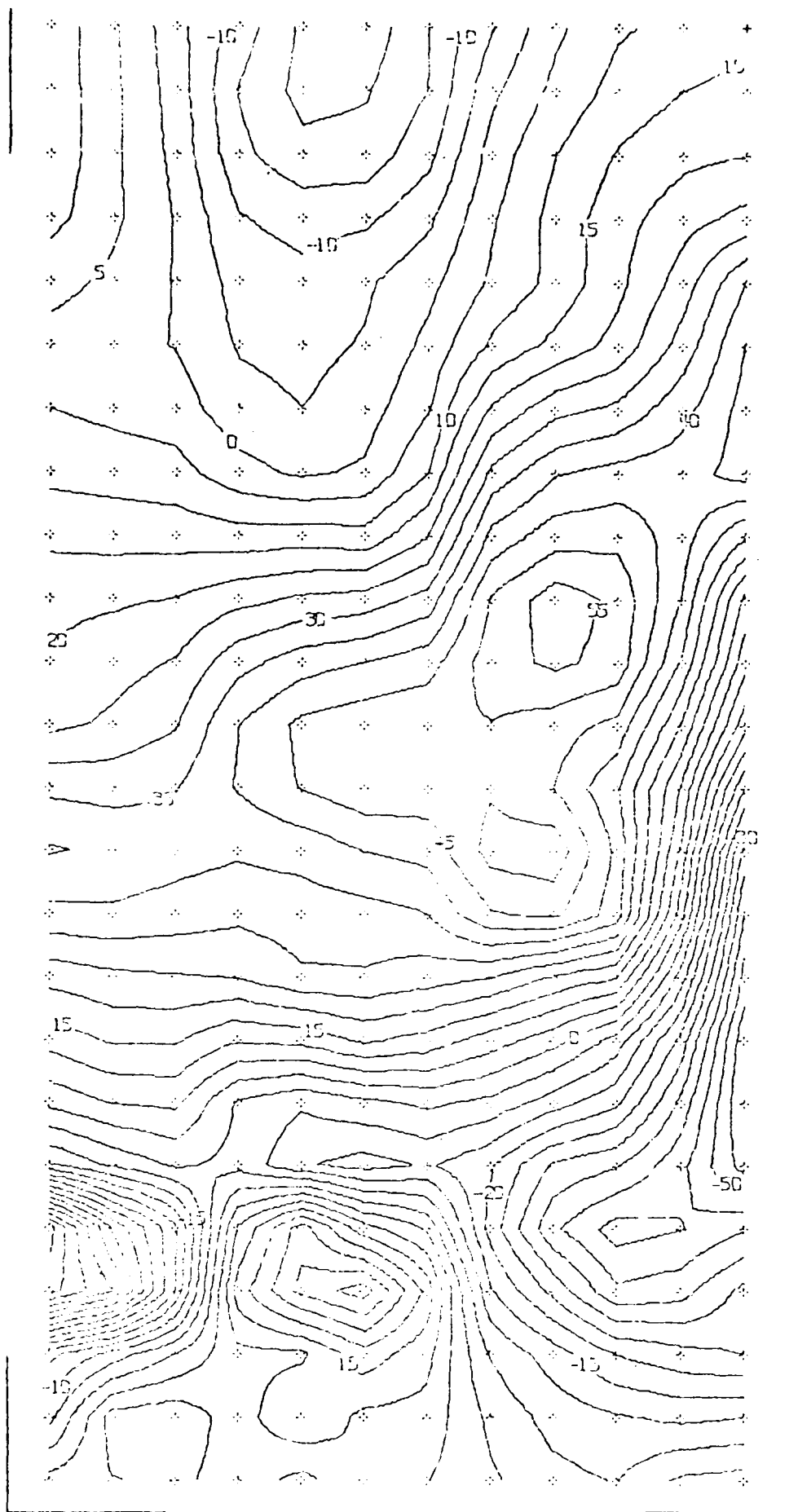
Figure 24. Streamwise expansion orthogonal descriptor in an unsteady jet flowfield.
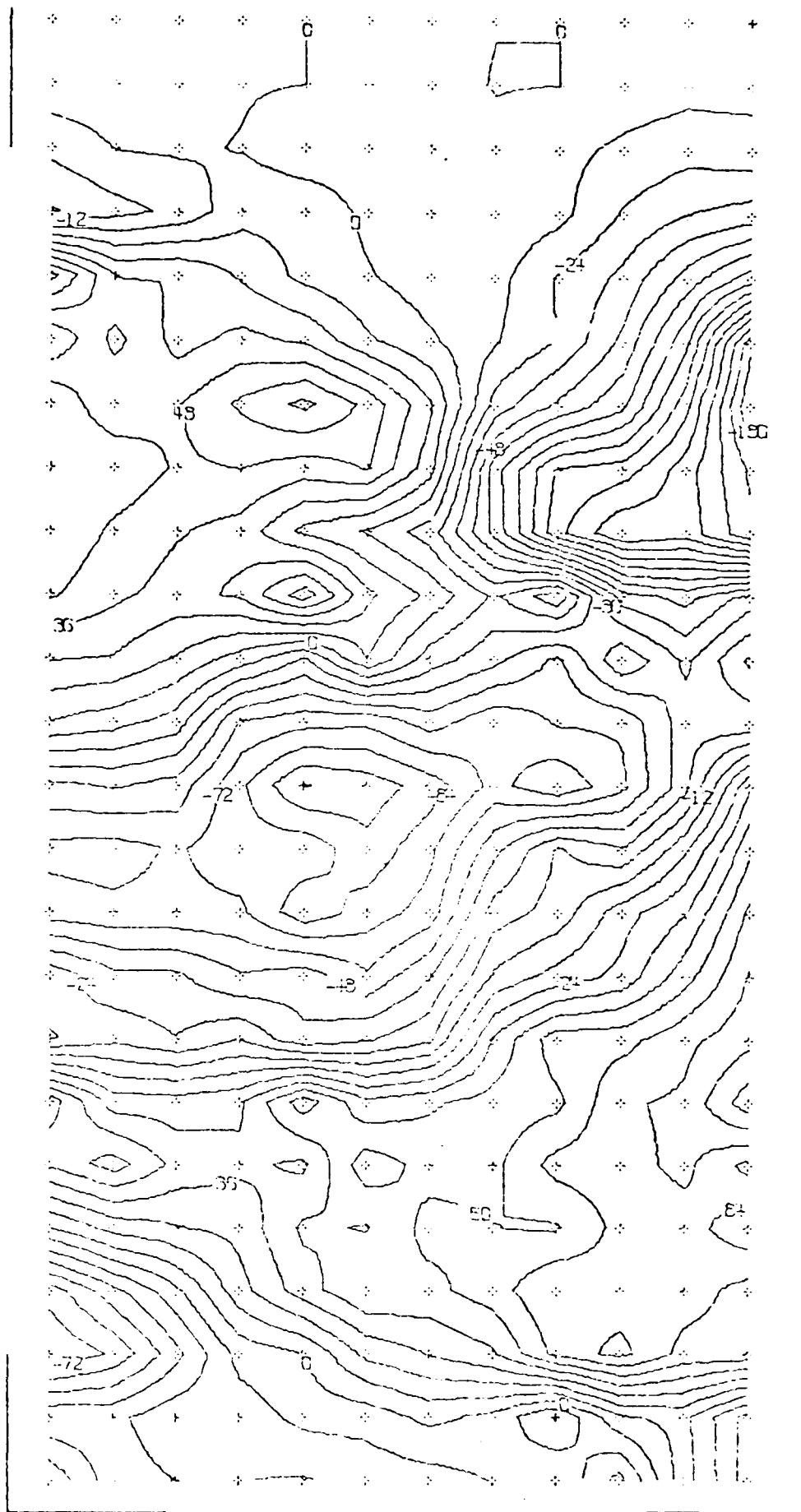
Figure 25.   Transverse component orthogonal descriptor
in an unsteady jet flowfield.
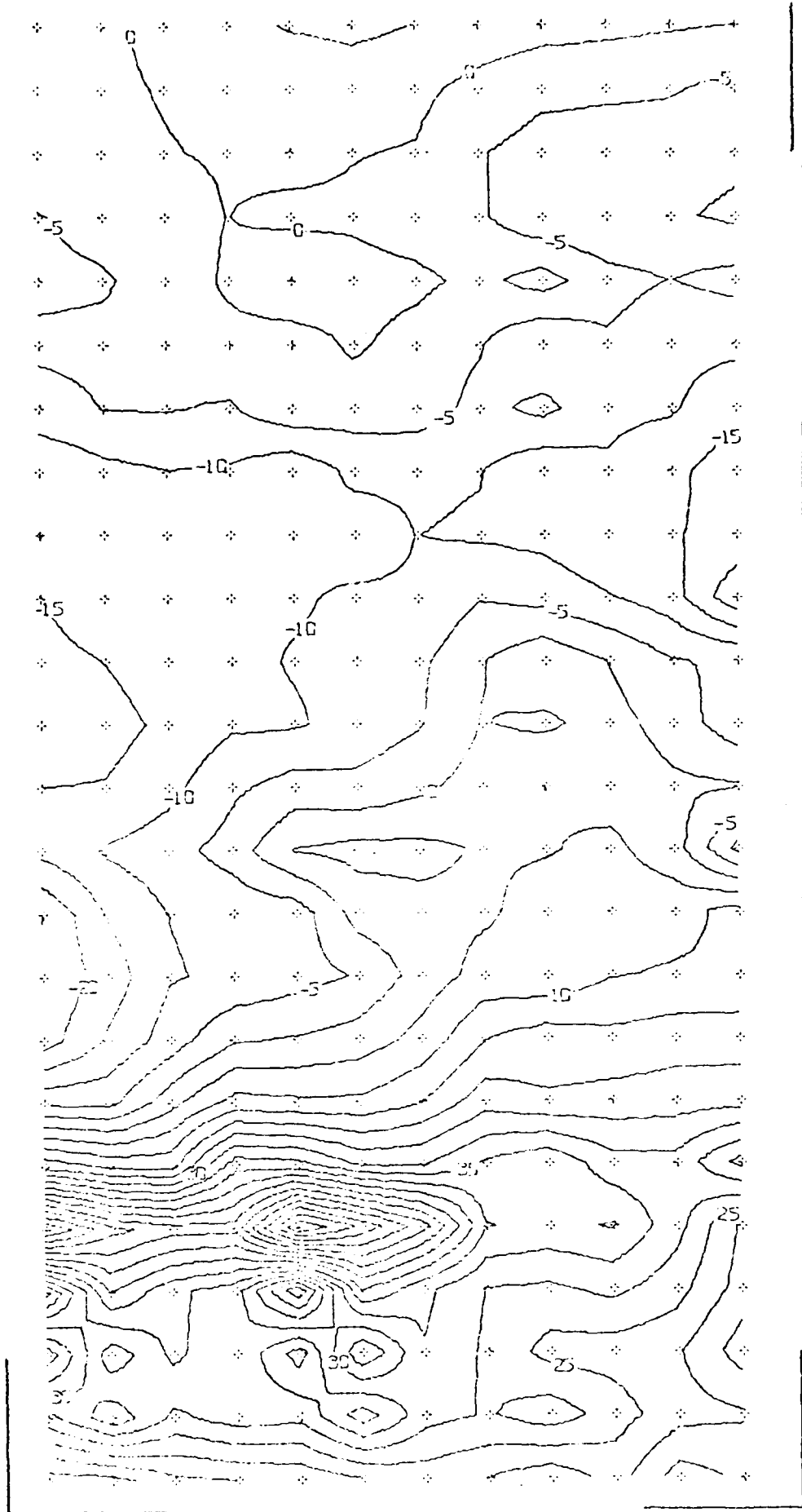
Figure 26. Shear orthogonal descriptor in an
unsteady jet flowfield.
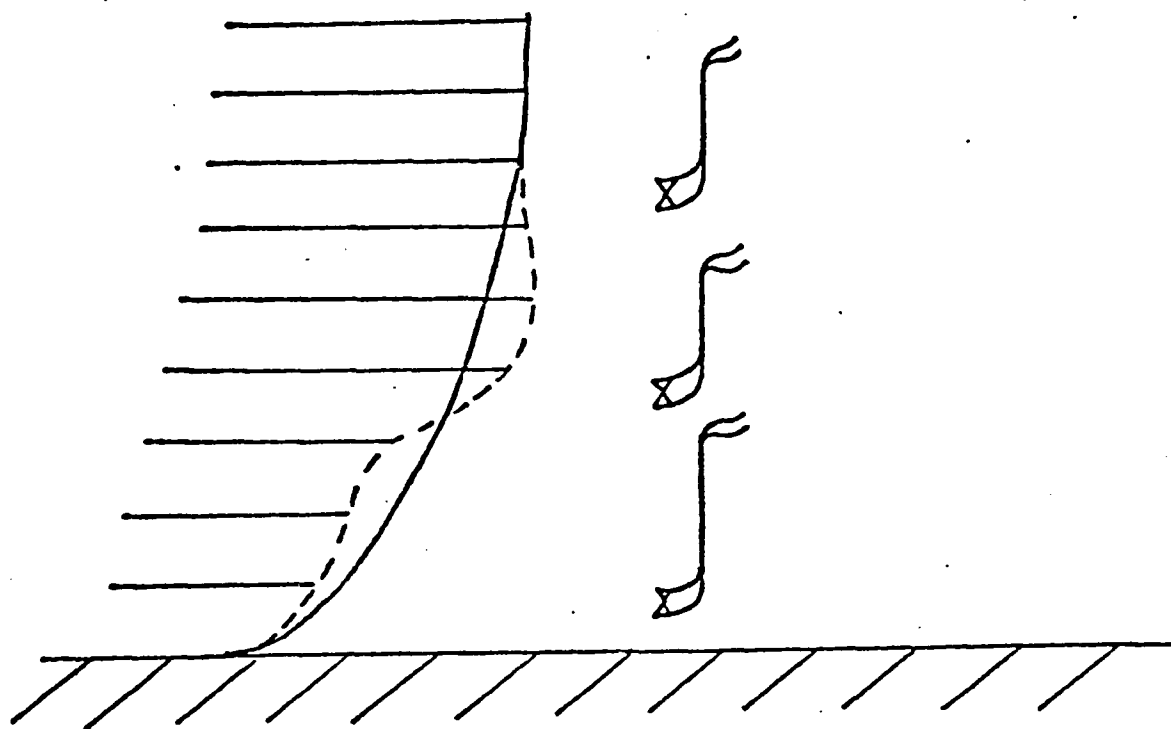
Figure 27. Multiple hot wire probes in a boundary layer containing a vortex.
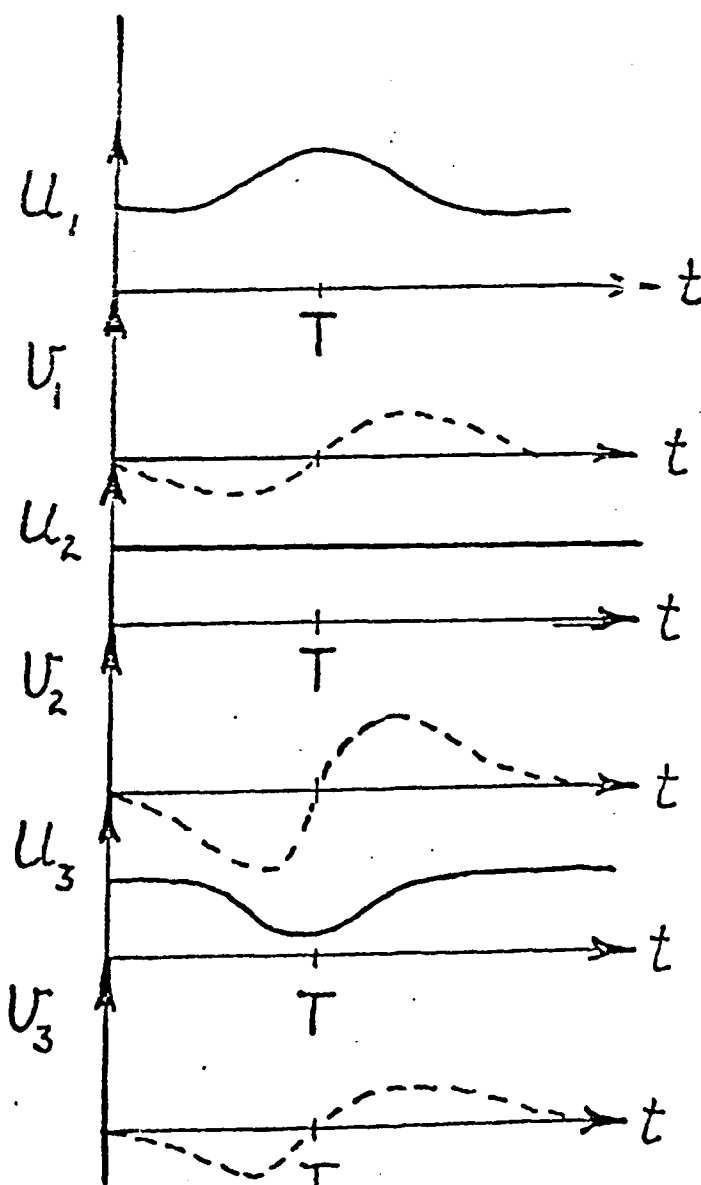
Figure 28. Schematic of the signals obtained from the probes of Figure 12.

Acoustic Structure Produced by an
Unsteady Jet in a Rectangular Duct+

Hermann Viets*
West Virginia University
Morgantown, WV 26506

Mont Ball**
Wright State University
Dayton, Ohio 45453

Summary

The acoustic field produced by an unsteady jet is examined both in the free jet configuration and when the jet is placed in a rectangular duct. Standing transverse acoustic waves are identified in the duct and they correspond to transverse duct dimensions which lead to a resonance with the driving frequency. The presence of the strong acoustic waves offers the possibility of employing these waves to transfer energy by means of normal forces as opposed to the more traditional view of an essentially viscous transfer by means of the physical mixing of two flows. From the point of view of potential application, such driven duct flows may correspond to ejectors or to jet pumps. Therefore, the mass flow through the rectangular duct is measured and analyzed as a gross indication of the momentum transfer from the jet to the induced flow.

Introduction

The use of unsteady flow to enhance the transfer of momentum from a primary to a secondary flow has been pursued by various investigators operating

---

* Associate Dean and Professor, College of Engineering

** Senior Technician

from different points of view. Much of the effort has centered on creating a time dependent primary flow to transfer momentum by normal (pressure) forces rather than tangential (shear) forces. Such a transfer would be more efficient and could be accomplished in a shorter streamwise distance. A secondary objective, still of interest even if the primary objective is not attained, is to increase the mixing rate of the primary jet so that relatively complete mixing is accomplished in a short streamwise distance. The advantage of complete mixing for ejector applications has been described by Quinn,[1] Bevilaqua[2] and others. The mixing increase must be achieved, however, without an exorbitant increase in primary nozzle losses. A comprehensive review of ejectors has recently been completed by Porter and Squyers[3] and includes unsteady effects.

The objective of the present paper is to outline briefly some of the past efforts in unsteady jets and duct flows and to highlight some current work in that area.

Some Past Unsteady Experiments

The primary objective of past experiments related to the unsteady transfer of momentum from one flow to another has been to increase the performance of ejector devices. An early experiment was performed by Lockwood[4] employing a pulsejet combustor similar to those used in German aircraft in the mid 1940's. The pulse consisted of a slug of air which passed through the shroud in the manner of a piston. An analysis of such a system where the primary flow (when it is on) completely fills the ejector shroud has been performed by Johnson and Yang[5] by the method of characteristics. These results are in reasonable agreement with the results of an accompanying experiment and suggest the existence of an optimum frequency.

Although the concept of filling the duct completely with a slug of fluid is enticing, it is not entirely suitable for higher area ratios between the

secondary and primary flows. For such cases, Foa[6] proposed a rotary primary jet where the components of the rotating nozzle were pictured to act like vanes of an impeller. The rotary jet has been analyzed by Hohenemser and Porter[7] and further tested for application by Maise.[8]

Various investigators have examined different ways of generating a time dependency in a free jet flow. McCormack, Cochran, and Crane[9] vibrated the jet nozzle in a transverse direction. Binder and Favre-Marinet[10] employed a rotating butterfly valve upstream to generate a pulsing flow at the exit of an axisymmetric nozzle. Flow visualization studies by Curtet and Girard[11] verified this structure and showed that the pulsating flow resulted in a series of vortex rings. This pulsating jet was subsequently applied in an ejector configuration[12] and indicated an improvement in performance especially for short ejectors. Unfortunately, the performance in this case was defined as the Ejector Thrust/ Nozzle Thrust with a fixed total pressure. This definition does not take into account the nozzle thrust efficiency nor any changes in primary mass flow between the two conditions, so the actual performance is still in question.

A fluidically controlled rectangular nozzle which produces a flapping jet was developed by Viets[13] and exhibited a rapid half width growth. The advantages of the fluidic control are the lack of moving parts and fluid control lines. Detailed investigations of this jet[14,15] showed strong vortex interactions leading to the mixing improvements. Vortex growth in driven unsteady jets at low Reynolds Numbers has been shown by Rockwell.[16] Another nozzle employing a fluidic instability was developed by Hill and Green[17] and consists of a rapid expansion section in a round duct.

Simmons, Platzer and Smith[18] have examined the unsteady jet flowfield produced by an angular oscillation of the jet nozzle itself and have recently studied a jet driven by an embedded oscillating vane.[19]

In addition to the emphasis on the primary jet itself, some recent effort has been directed at the control of wall boundary layers by unsteady stimulation[20,21] which has application to the mixing duct problem. Again the aim is to create vortex structures to improve mixing and energize the lower part of the boundary layer.

Acoustic Effects

Most of the unsteady primary nozzles described above have considered the performance advantage of such nozzles to be basically due to the improved mixing rate thereby produced. In application, this requires the thrust efficiencies of the unsteady nozzles to be high enough to make them competitive with nozzles such as the hypermixing type.[1,2] If the thrust efficiencies are not sufficiently high, the loss in the primary nozzle cannot be overcome by a viscous mixing improvement. There is, however, an alternate phenomenon which can be employed to improve the mixing by transferring the energy through normal (pressure) forces rather than tangential (viscous) forces as discussed in Section 1. The mixing can be accomplished by an acoustic interaction between the primary jet and the duct walls as demonstrated by Quinn.[22] His configuration consisted of an axisymmetric duct and a choked primary jet, which produces a strong screech tone as shown by Powell[23] and recently studied by Krothapalli, Baganoff, Hsia and Karamcheti.[24]

The acoustic interaction is most effective when the acoustic frequency available from the primary jet is well matched with the fundamental natural modes in the duct shroud. As demonstrated by Viets, Campbell and Korkan,[25] a substantial difference in frequency between the jet and the fundamental modes greatly reduces the acoustic effect and the resultant mixing improvement. For a rectangular duct with a rectangular primary nozzle, matching the acoustic frequencies can become a problem if one simultaneously desires a reasonable

high secondary to primary flow area ratio. In addition, for jet flows of less than unit mach number at the exit, there is no distinct frequency generated but rather a broad band noise. Therefore, under conditions of an unchoken primary jet or a choked primary in conjunction with a larger secondary to primary area ratio, an alternate acoustic generator is required if an acoustic interaction is to be provoked.

One possibility for use as an unsteady primary jet under these conditions is the "whistler nozzle" described in Reference 17, since it can operate at subsonic mach numbers. The acoustic feedback fluidic jet[13] is also a possibility if sufficiently high frequency can be generated. A rotor jet based on the mechanical devices described in Refs. 20 and 21 is also a possible choice for a primary and offers the additonal advantage of allowing a number of primary nozzles to have not only the same frequency but also a fixed phase relationship and is currently being studied. This is also true of a modified version of the acoustic feedback jet nozzle[13] described in Ref. 26 as a gust tunnel application.

A Subsonic Acoustic Generator

Still another nozzle which offers the required acoustic properties at subsonic exit velocities was originally developed as a two phase injector,[27] operating with a liquid primary into a gaseous secondary. The nozzle has the advantage of no moving parts and hence high reliability. Operating in a single phase condition in air, the nozzle produces distinct frequencies which can be tuned both by changes in the nozzle geometry and by the operating conditions. The nozzle schematic is shown in Figure 1. The nozzle operation simply requires that the jet attach to one wall within the nozzle body. Then part of the jet is scooped off, fed back and impressed on the jet flow just downstream of the contraction. This causes the jet to attach to the opposite

wall and the process begins anew. The strongly unsteady quasi-sinusoidal flowfield is clear in Figure 2 which illustrates the two phase operation of water flow into air.

The remainder of this paper will consider the flowfield generated by this nozzle and its acoustic interaction with the duct geometry. If the acoustic interaction is substantial, then the nozzle can be optimized in terms of scale, frequency and spreading rate relative to a particular duct geometry to allow its application to an ejector-type device.

The acoustic interactions observed by Quinn[22,28] were attributed to standing transverse waves in the duct due to a tuning of the screech tones produced by the choken jet to the transverse dimension. This interaction probably causes the jet itself to oscillate. In the present case, the jet is driven unsteady even without an acoustic interaction. Thus the effect of the acoustics on the jet may be rather small.

Free Jet Acoustics

Three unsteady jets and one slot jet were investigated in this program. Two of the unsteady nozzle designs are shown in Figure 3. The primary difference between the two designs is the length of the feedback loop. The different designs lead to a frequency difference of roughly a factor of three at nozzle stagnation pressure ratios of about 1.15 based on ambient pressure. Nozzle 3 is essentially the same design as Nozzle 2 except for a somewhat shorter feedback loop which increases the frequency by about 20%.

In order to correlate the flow inside the oscillating jet with the acoustic structure outside, hot wire measurements within the jet were compared with pressure transducer measurements and microphone measurements taken outside the jet. A Flow Corp. (now Datametrics) Model 900 constant temperature hot

wire anemometer was employed inside the jet and an Endevco Model 8506-2 high frequency response pressure transducer as well as a B&K Model 4136 microphone and amplifier system were employed outside the jet. The output from each of the systems was input to a Hewlett-Packard Model 3582A spectrum analyzer which yields the magnitude as a function of frequency. Thus the dominant frequencies present in any signal could be easily determined. A typical spectral output for Nozzle #2 at a stagnation pressure ratio of 1.17 is shown in Figure 4 as determined with the Endevco pressure transducers.

The two lowest frequency modes present in the flowfield on Nozzle #2 are compared in Figure 5 as they are determined both in the jet (hot wire) and out of the jet (microphone and pressure transducer). The apparent frequency steps in the hot wire case are only caused by the finite bandwidth employed by the spectrum analyzer. The conditions inside and outside the jet flow clearly indicate the same frequency content. The pressure is non-dimensionalized with the ambient pressure while the frequency is reduced to a Strouhal number form by V/D (exit velocity/exit dimension).

The dominant frequencies outside the jet flow are compared in Figure 6 for the microphone and pressure transducer results. In each case the instrument is located in the exit plane of the jet and at a distance equal to half the major dimension of the ejector shroud (in other words, located at the same position as the shroud wall, when the shroud is mounted).

Each of the frequency modes A-G can be identified and explained. Mode A is the driving mode of the jet oscillation. Mode B is the second harmonic, being double the frequency of Mode A. Mode C is very weak. In some of the spectra it hardly appears. The fourth harmonic is Mode E, while Modes F and G are again only multiples of Modes E and F respectively. The intermediate Mode D can be explained based on the nozzle results in 3311 Hz, which is the Mode D. Since

the Mode D, based on the nozzle scale is so close to Mode C, the third harmonic of the driving motion, the energy from Mode C appears to be contributing to Mode D and thereby reducing its own amplitude.

The frequency of Nozzle #3 is increased over that of Nozzle #2 as shown by Figure 7. The first harmonic exists at approximately 1300 Hz or a Stroudal number of .059. At higher pressures, the second harmonic clearly exists at approximately 2600 Hz (i.e. curve B) and the third harmonic at curve D. The intermediate mode, curve C is caused by the duct mode based on the depth of the rectangular nozzle, 5.08 cm. as was the case in Nozzle #2.

As the pressure is lowered, the frequency of Mode B rises while the frequency of the duct Mode C decreases. The two modes coalesce by P = 1.08. At higher pressures a third harmonic (Mode D) is evident but weak, while at lower pressures a higher frequency value appears. The fourth harmonic exists at low pressures while at higher values Mode E appears to be the multiple of the average of Modes B & C.

Free Jet Flowfields

As might be expected based on previous flapping free jet experiments (Refs. 13, 15, 18 & 27), the unsteady jet mixes more rapidly with the ambient fluid than jets without a time dependent driver. The centerline velocity decay and the half width growth of Nozzles 1 & 2 are shown in Figures 8 and 9 respectively and are compared to the two dimensional slot jet value. Based on the velocity decay, Figure 8, there appears to be a small frequency dependence showing improved mixing (decay) as the frequency decreases. This result is opposed to that of Reference 19 which found a mixing improvement with frequency.

The two apparently conflicting results can fit into a coherent picture of the vortex growth in the unsteady jet. As clearly shown by Brown[29] and

others, a forced unsteady jet leads to large vortex formations. For the case of the flapping jet, these vortices have been found by both flow visualization and by conditioned sampling with a hot wire anemometer.[15] For low frequencies, these vortices would be widely spaced and weak and exert little influence on the the entrainment. Under these conditions, an increase in frequency would improve the mixing properties. On the other hand, at higher frequencies there is little to be gained by having the vortices even more closely spaced.

The effect of vortex growth may also be seen in the half width growth results of Figure 9. For each frequency, there appears to be a plateau or leveling of the half width growth at a different streamwise location. The most obvious case is the frequency of 980 Hz and occurs at approximately 13 nozzle width downstream. For higher frequencies, this occurs progressively farther downstream and for f = 3500 Hz the plateau is twice as far downstream as for 980 Hz. Apparently the near field entrainment depends upon the frequency. Brown has observed that the vortices entrain in the near field but do not entrain external fluid farther downstream. Thus the plateaus may reflect the end of the near field entrainment caused by the vortex structure.

Duct Acoustics

A rectangular duct was chosen as the ejector shroud as shown in the schematic of Figure 10. The inside dimensions of the duct are 5.1 cm by 17.8 cm. The duct length was varied during the experiment. The longer transverse dimension of the duct was chosen to achieve resonance with a driving frequency of approximately 1000 Hz.

As described by Succi, et al.[30] and employed by Viets et al.,[25] the frequencies of the modes corresponding to resonant transverse waves are related to the speed of sound C_o and the duct dimensions b and d by

$$F_{m,n} = \frac{C_o}{2} \left[(m/b)^2 + (n/d)^2 \right]$$

where m and n are integer values.

If the speed of sound is assumed to be 335 m/sec (1100 ft/sec), then the frequencies corresponding to some particular resonant modes are shown below for duct dimensions 5.1 cm by 17.8 cm.

m	n	F(Hz)
1	0	946
2	0	1887
3	0	2833
0	1	3289
0	2	6578
1	1	3422
2	1	3791

It should be noted that these values do not take into account the flow in the duct nor any real fluid or real wall effects. Actual resonant frequencies are expected to approximate these values but are not precisely equal to them.

In order to test the duct acoustics, white noise (produced by a General Radio Type 1390 A Random Noise Generator) was introduced at the duct inlet and the resulting acoustic levels measured at the exit plane of the duct (located at $L/D = 6.1$). A typical spectrum of the acoustic output on the duct exit centerline is shown in Figure 11a. The clearly defined peaks indicate a response of the duct to those frequencies. Calibration of the level of the white noise source shows that the peaks between 150 and 400 Hz are exaggerated out of proportion due to the fact that the input levels are high. The lowest transverse resonant frequency was shown to be approximately 946Hz. The peaks between 400 Hz and the lowest transverse frequency are attributed to the organ pipe modes described by Morse and Ingard,[31] which have a lowest mode of 150 Hz (for this length).

If the acoustic measurements are taken off the duct centerline, even to the point of reaching the far wall location, the peaks between 400 and 900 Hz are not greatly affected as seen in Fig. 11b. This is consistant with their dependence on the duct length. However, the modes near the 1000 Hz transverse resonance value do vary with transverse position as might be expected.

To test the longitudinal modes, the end of the duct is filled with sound absorbing foam which should eliminate the organ pipe mode by now allowing reflections of the waves. That this is accomplished is seen in Figure 11c (with the microphone inserted through the foam) especially in comparison with Figure 11a. It is interesting that there remains a small peak at 990 Hz (remember that the apparent low frequency modes are caused by the input signal.

Transverse Waves

The overall objective of the oscillatory duct flow is to examine the transverse wave structure to see if such waves are actually generated. High frequency response Endevco transducers are mounted to the duct walls at a streamwise position equal to two duct dimensions (35.6 cm). The output signals are fed to a Hewlett-Packard Model 358A Spectrum Analyzer which decomposes the signal into its frequency components.

(a)   Resonance in a long duct, $X/D = 6.1$, Nozzle #2

The variation of each component magnitude across the duct is shown in Figure 12 for Nozzle #2, having a lowest harmonic frequency approximately equal to the anticipated transverse resonant duct frequency. The first harmonic, 1060 Hz, produces a standing wave of a half wavelength with a node at the center. The second harmonic yields an entire wave with two node points. The third and fourth harmonics are very consistant with $1\frac{1}{2}$ and two waves respectively.

The same procedure applied across the short side of the rectangular duct yields the result of Figure 13 which clearly shows that the standing wave structure is not a function of that direction.

Taking the same pressure measurements at an upstream position, $x = .28$ (near the ejector inlet), and decomposing the signals into their frequency components results in Figures 14 and 15. The structure of the first, second, and fourth modes are similar to the downstream structure (Figures 12 and 13) except for several data points near the center of the duct. This discrepancy is caused by the primary jet, which has a high velocity at that streamwise location and interferes with the pressure measurement. An additional discrepancy between the upstream and downstream modes is shown in the two third (3200 Hz) modes. The problem is resolved by the fact that 3200 Hz is the transverse duct mode corresponding to the nozzle depth as was discussed in relation to the free jet modes, Figures 6 and 7.

(b) Resonance in long duct, $X/D = 6.1$, Nozzle #1).

The spectra developed by the pressure traverse of the duct at $S/D = 2$ downstream exhibit a strong peak at the primary frequency of Nozzle #1, 3300 Hz, as shown in Figure 16. Based on the results of Figure 12, a waveform of $1\frac{1}{2}$ waves is expected at the 3300 Hz frequency. However, only a full wave is found. There may be an effect due to the nozzle duct frequency which is almost equal.

The next substantial wave structure, at 7800 Hz, shows no definite pattern. However, if the resonant frequency of the longer transverse dimension of the duct is 1060 Hz (from Figure 12), a corresponding resonance in the short duct dimension is 3700 Hz. The 7800 Hz frequency is roughly double that value, so one might expect a waveform similar to that of the 2120 Hz case in Figure 12, but in the short dimension. That is indeed a possible waveform as seen in Figure 17.

At frequencies of 10,300 and 15,500 Hz, higher order mode shapes are possible. The former could, for example, correspond to the mode $M = 5$, $n = 2$ while the latter may correspond to $M > 5$, $n = 2$. Of course as the order of the modes increases, it is more difficult to determine the precise modes since the spectrum becomes very crowded with possible modes. From the point of view of the unsteady ejector, the higher order modes are really of less interest because they are expected to contain less energy.

(c) Resonance in long duct $X/D = 6.1$, Nozzle #3

The lowest dominant frequency for this nozzle, 1300 Hz, effectively produces resonance in the duct according to Figure 18 and verified by the uniform magnitude in the other direction, Figure 19.

The next appreciable wave is at 4640 Hz and is not a harmonic of the first mode but is related to both duct dimensions. From Figures 18 and 19, $M = 2$ and $n = 1$. The calculated frequency for this mode structure is 3791 Hz, which is, of course, for the zero flow condition.

The 6000 Hz case does not indicate a clear wave shape. It is a mixed mode depending on both transverse dimensions and is almost a combination of the lower frequencies. It may be a result of an oscillation among several modes which exist near this frequency. Additional minor mode peaks exist at higher frequencies and there it becomes increasingly difficult to distinguish between modes.

Thus, when the forced oscillation is near the resonant frequency, it achieves a manner of resonance which is not as strong as it would be if the frequency were better matched. It does, however, produce similar pressure waves.

(d) Resonance in shorter ducts

The standing waves described above appear even for very short ejector shrouds. The transverse waves in an ejector of length equal to its major width, i.e. $L/D = 1$, are shown in Figure 20 driven by nozzle #2. The mode

structure is essentially the same as in Figure 12 and shows the same primary
nozzle interference as in Figure 14.

Mass Augmentation

In order to examine the potential application to an ejector device, the
mass augmentation was determined by integrating the exit velocity profiles and
dividing by the primary mass flow as determined by the venturi measurement.
The mass flow ratios are shown in Figure 21 as a function of duct length for
the slot nozzle and three different oscillating nozzles. The actual levels
of mass augmentation are not significant because the nozzles have not been
optimized in terms of thrust efficiency and spreading rate relative to the duct
size.

The trends in mass flow ratio show that for a long duct the use of
unsteady flow in general and acoustic interaction in particular is not warranted.
The loss in nozzle thrust efficiency suffered by the unsteady jets has over-
powered any mixing and acoustic advantages. However, for shorter duct lengths,
the performance does not deteriorate as rapidly with length for the oscillating
jets as compared to the slot jet. It is for these very short ducts that the
unsteady effects discussed here are expected to be of significance.

The monotonic decrease in performance with decreasing length is only
interrupted at a length of 2.1 shroud widths. This position will be examined
in greater detail but the preliminary indications are that there is no strong
streamwise organ type of resonance. That is, there is a coherent streamwise
wave but it is not greater in magnitude than the wave which exists for a duct
length of $L/D = 3$.

Conclusions

The fluidically controlled, positive feedback jet has exhibited the
potential to generate a significant acoustic interaction between parallel

walls. The frequencies can be controlled by the nozzle design in order to match the scale of the duct geometry. The resonant condition (i.e. a match between the jet oscillation frequency and the natural frequency of the wall separation) yields a strong interaction and standing transverse waves between the walls. The existence of this interaction expected to be a prerequisite for a significant energy transfer through the acoustic mechanism. Actual proof of this transfer will require additional work.

The transverse waves generated by the unsteady jet have potential application to ejectors, both for thrust augmentation and pumping. The performance of such devices remains to be optimized. In particular, the design of the nozzle geometry must take into account not only the matching of the duct geometry to the frequency but also simultaneously matching the spreading rate to the duct geometry. In order to accomplish this result, preliminary nozzle experiments are required to determine the frequencies and spreading rates of a number of various designs. From these a design can be chosen which satisfied both the acoustic and mixing requirements.

References

1. Quinn, B., "Compact Ejector Thrust Augmentation," J. Aircraft, Vol. 10, No. 8, Aug. 1973, pp. 481-486.

2. Bevilaqua, P. M., "Evaluation of Hypermixing for Thrust Augmenting Ejectors," J. Aircraft, Vol. 11, No. 6, June 1974, pp. 348-354.

3. Porter, J. L. and Squyers, R. A., "A Summary/Overview of Ejector Augmentor Theory and Performance," Vought Corp., ATC Report No. R-91100-9CR-47, April 1981.

4. Lockwood, R. M., "Investigation of the Process of Energy Transfer from an Intermittent Jet to a Secondary Fluid in an Ejector-Type Thrust Augmentor," Hiller Aircraft Corp. Report No. APR-64-4, March 1964.

5. Johnson, W. S. and Yang, T., "A Mathematical Model for the Prediction of the Induced Flow in a Pulsejet Ejector with Experimental Verification," ASME Paper WA/FE-33, 1968.

6. Foa, J. V., "A Vaneless Turbopump," AIAA Journal, Vol. 1, No. 2, Feb. 1963, pp. 466-7.

7. Hohenemser, K. H. and Porter, J. L., "Contributions to the Theory of Rotary Jet Flow Induction," J. Aircraft, Vol. 3, No. 4, 1966, pp. 339-46.

8. Maise, G., "Effects of Shroud Design on the Performance of Rotary-Flow Augmentors," Grumman Aerospace Corp. Report. PXP-001-38, June 1974.

9. McCormack, P. P.; Cockran, D. and Crane, L., "Periodic Vorticity and its Effect on Jet Mixing", Physics of Fluids, Vol. 9, No. 8, Aug. 1966, pp. 1550-60.

10. Binder, G. and Favre-Marinet, M., "Mixing Improvement in Pulsating Turbulent Jets," Symposium on Fluid Mechanics of Mixing, ASME, 1973.

11. Curtet, R. M. and Girard, J. P., "Visualization of a Pulsating Jet," Symposium on Fluid Mechanics of Mixing, ASME, 1973.

12. Binder, G. and Didelle, H., "Improvement of Ejector Thrust Augmentation by Pulsating on Flapping Jets", Symposium of Jet Pumps & Ejectors and Gas Lift Techniques, Cambridge, England, 1975. (Published by BHRA Fluid Engineering, Cranfield, Bedford, England).

13. Viets, H., "Flip Flop Jet Nozzle", AIAA Journal, Vol. 13, No. 10, Oct. 1975, p. 1375. (Also AIAA Paper No. 74-1189, AIAA 10th Propulsion Conf., San Diego, California, Oct. 1974).

14. Piatt, M. and Viets, H., "Conditioned Sampling in an Unsteady Jet," AIAA Paper No. 79-1857, AIAA Aircraft Systems and Technology Mtg., New York, Aug. 1979.

15. Viets, H., "Coherent Structures in Time Dependent Flow," Proceedings of the NATO/AGARD Specialists Meeting on Turbulent Boundary Layers, The Hague, Netherlands, CP-271, Sept. 1979.

16. Rockwell, D. O., "External Excitation of Planar Jets", J. Applied Mech., Dec. 1972, pp. 883-890.

17. Hill, W. G. and Green, P. R., "Increased Turbulent Jet Mixing Rates Obtained by Self Excited Acoustic Oscillations", J. Fluids Engin., Vol. 99, No. 3, 1977, pp. 520-525.

18. Simmons, J. M.; Platzer, M. F. and Smith, T. C., "Velocity Measurements in an Oscillating Plane Jet Issuing into a Moving Air Stream", J.F.M., Vol. 84, Part 1, 1978, pp. 33-53.

19. Collins, D. J.; Platzer, M. F.; Lai, J. C. S. and Simmons, J. M., "Experimental Investigation of Oscillating Subsonic Jets", Symposium on Numerical and Physical Aspects of Aerodynamic Flows, Calif. State Univ., Long Beach, Calif., Jan. 1981.

20. Viets, H.; Piatt, M. and Ball, M., "Boundary Layer Control by Unsteady Vortex Generation," Journal of Wind Eng. and Ind. Aero., Vol. 7, 1981, pp. 135-144.

21. Viets, H.; Ball, M. and Bougine, D., "Performance of Forced Unsteady Diffusers," AIAA Paper No. 81-0154, AIAA Aerospace Sciences Mtg., St. Louis, Mo., Jan. 1981.

22. Quinn, B., "Effect of Acoustic Interactions on Ejector Performance," J. Aircraft, Vol. 12, No. 11, Nov. 1975, pp. 914-916.

23. Powell, A., "On the Mechanism of Choked Jet Noise," Proc. Phys. Soc., Vol. B66, 1953, p. 1039.

24. Krothapalli, A; Baganoff, D; Hsia, Y. and Karamcheti, K., "Some Features of Tones Generated by an Underexpanded Rectangular Jet", AIAA Paper 81-0060, Aerospace Sciences Mtg., St. Louis, Mo. Jan. 1981.

25. Viets, H.; Campbell, J. and Korkan, K., "Acoustic Interactions in Ejectors", AIAA Paper No. 81-2045, AIAA 7th Aeroacoustics Conf., Palo Alto, Calif., Oct. 1981.

26. Viets, H.; Ball, M. and Piatt, M., "Experiments in a Subscale Pilot Gust Tunnel," AIAA Journal, Vol. 19, No. 6, June 1981, pp. 820-822.

27. Viets, H.; Balster, D. and Toms, H. L. Jr., "Time Dependent Fuel Injectors," AIAA Paper No. 75-1305, AIAA Propulsion Mtg., Oct. 1975.

28. Quinn, B., "Interactions Between Screech Tones and Ejector Peformance," J. Aircraft, Vol. 14, No. 5, May 1977, pp. 467-473.

29. Brown, G. B., "On Vortex Motion in Gaseous Jets and the Origin of Their Sensitivity to Sound", Physical Society, Vol. 47, Pt. 4, 1935, pp. 703-732.

30. Succi, G. P. Baumeister, K. J. and Ingard, K. V., "Interaction of a Turbulent Jet Noise Source with Transverse Modes in a Rectangular Duct", NASA Technical Paper 1248, June 1978.

31. Morse, P. M. and Ingard, K. V., "Theoretical Acoustics, McGraw-Hill, 1968, p. 474.
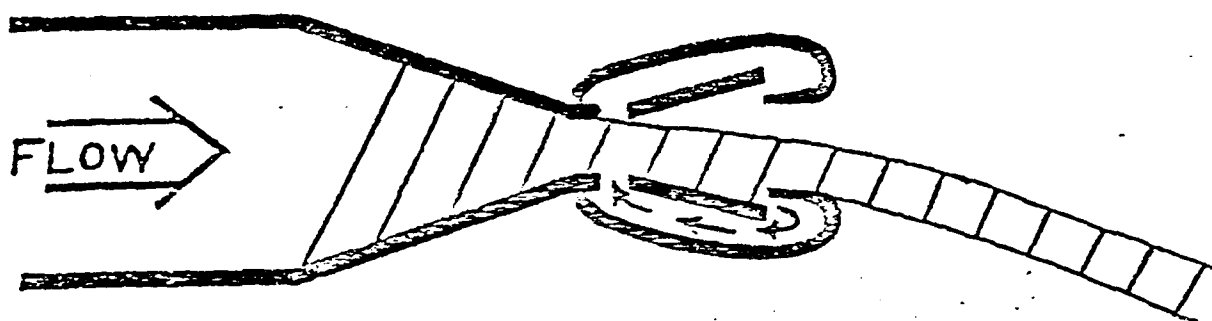
Figure 1. Schematic of the nozzle operation.
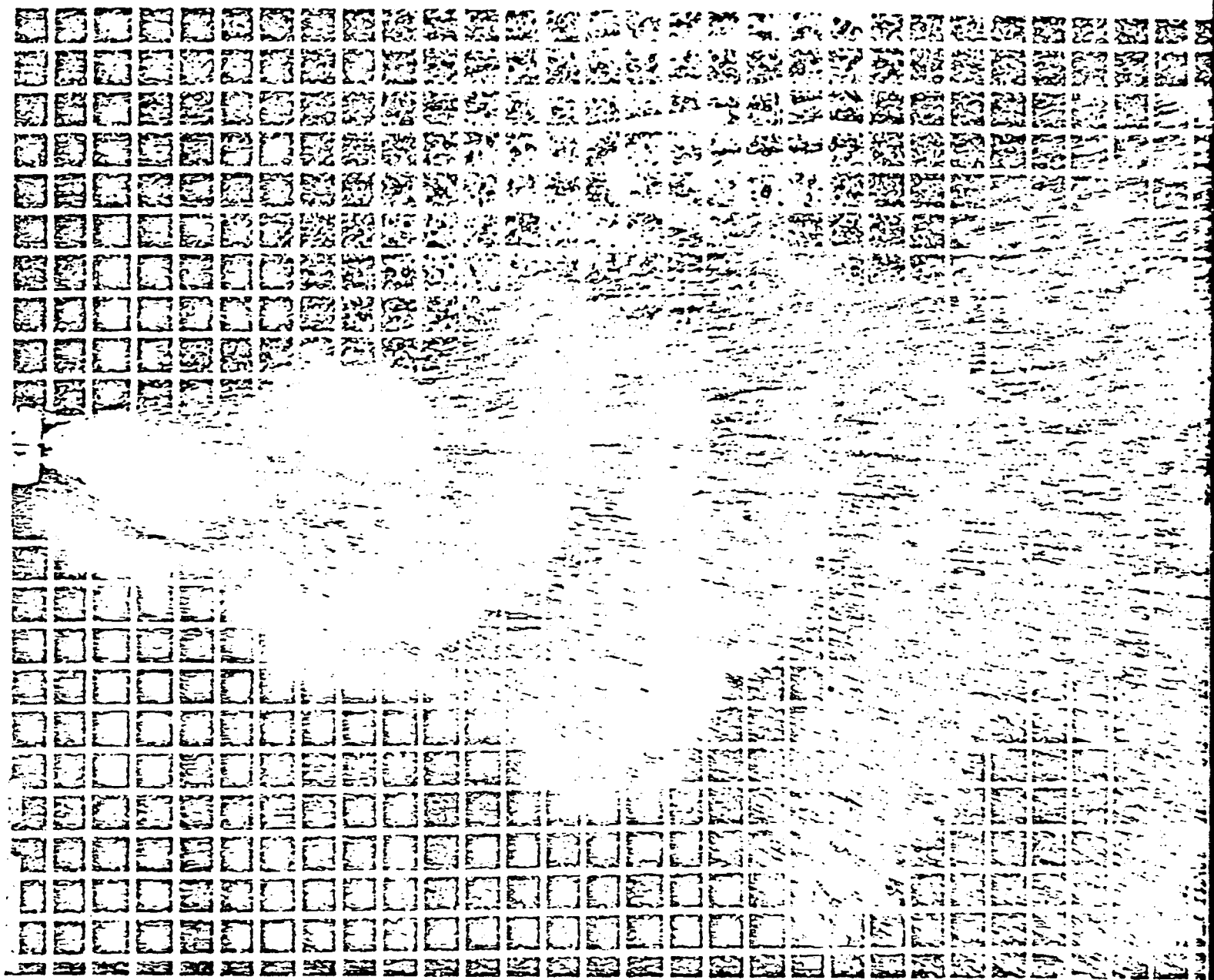
Figure 2. Two phase operation of Nozzle 1, water flow into air.
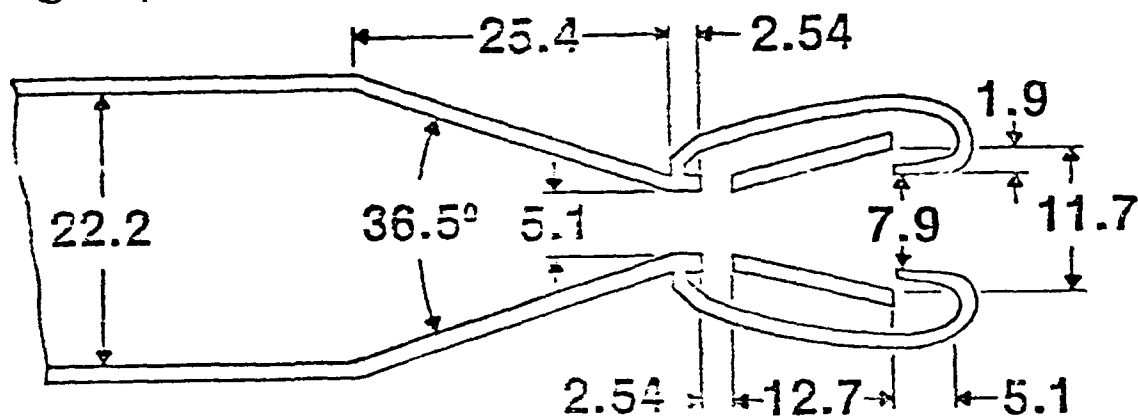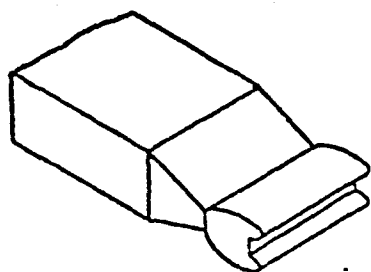
Figure 3a. Geometry of Nozzle 1.

Nozzle 2 dimensions in millimeters

Figure 3b. Geometry of Nozzle 2.
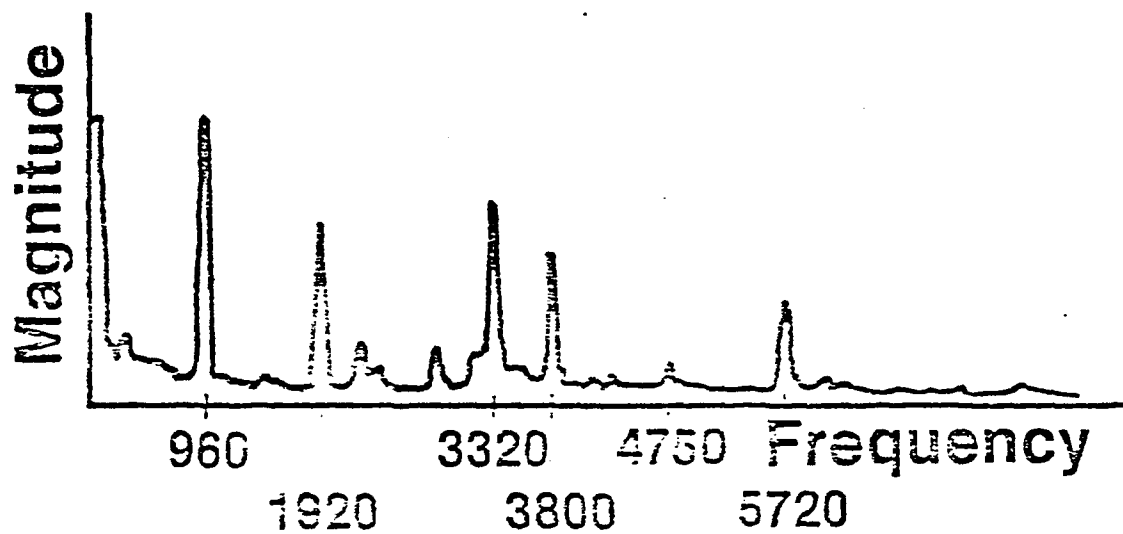
Figure 4. Frequency spectrum of Nozzle 2.
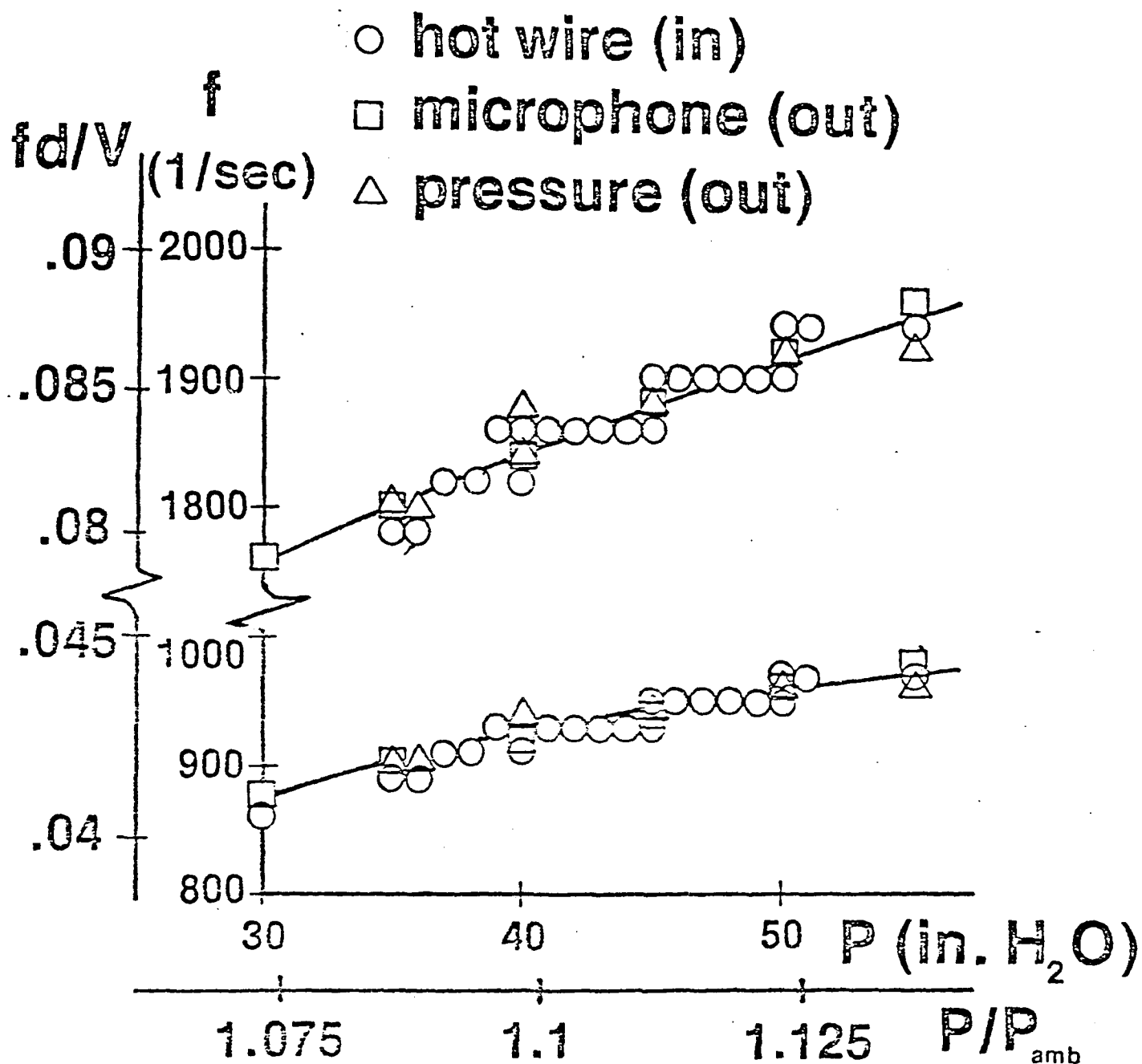
Figure 5. Frequency variation with pressure level for
Nozzle 2 by three different methods.
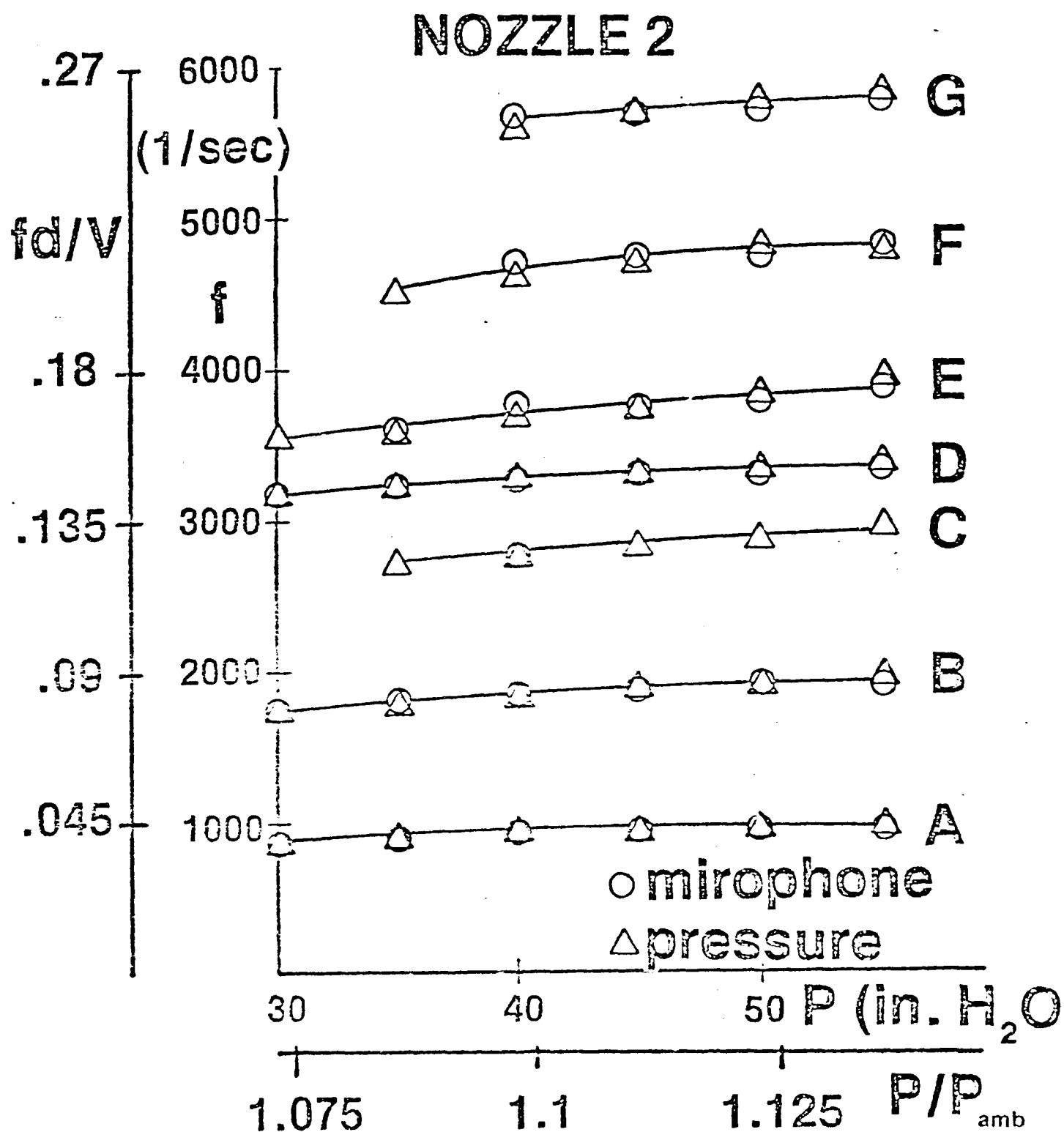
Figure 1. Frequency modes with pressure for Nozzle 2.
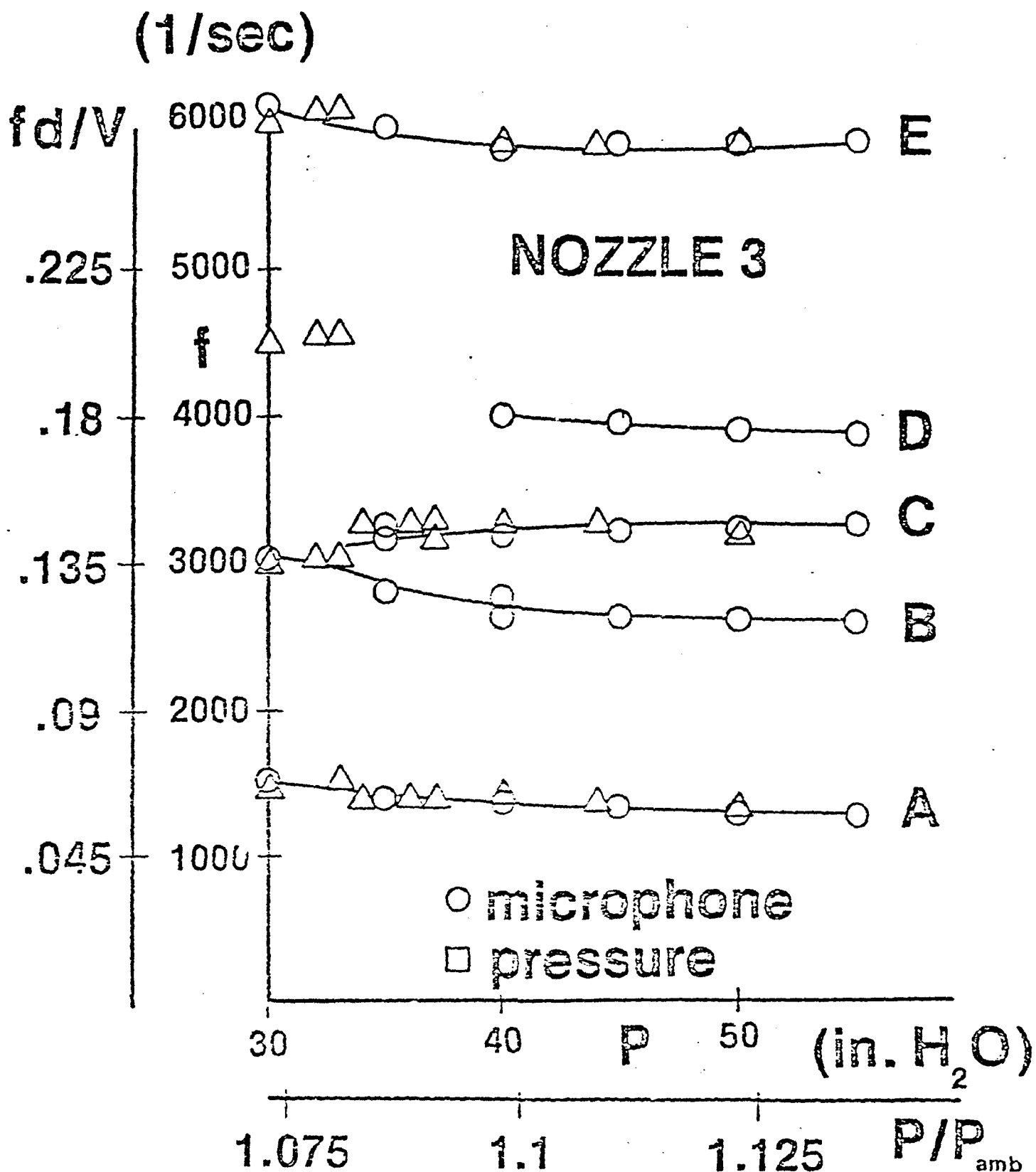
Figure 7. Frequency modes with pressure for Nozzle 3.
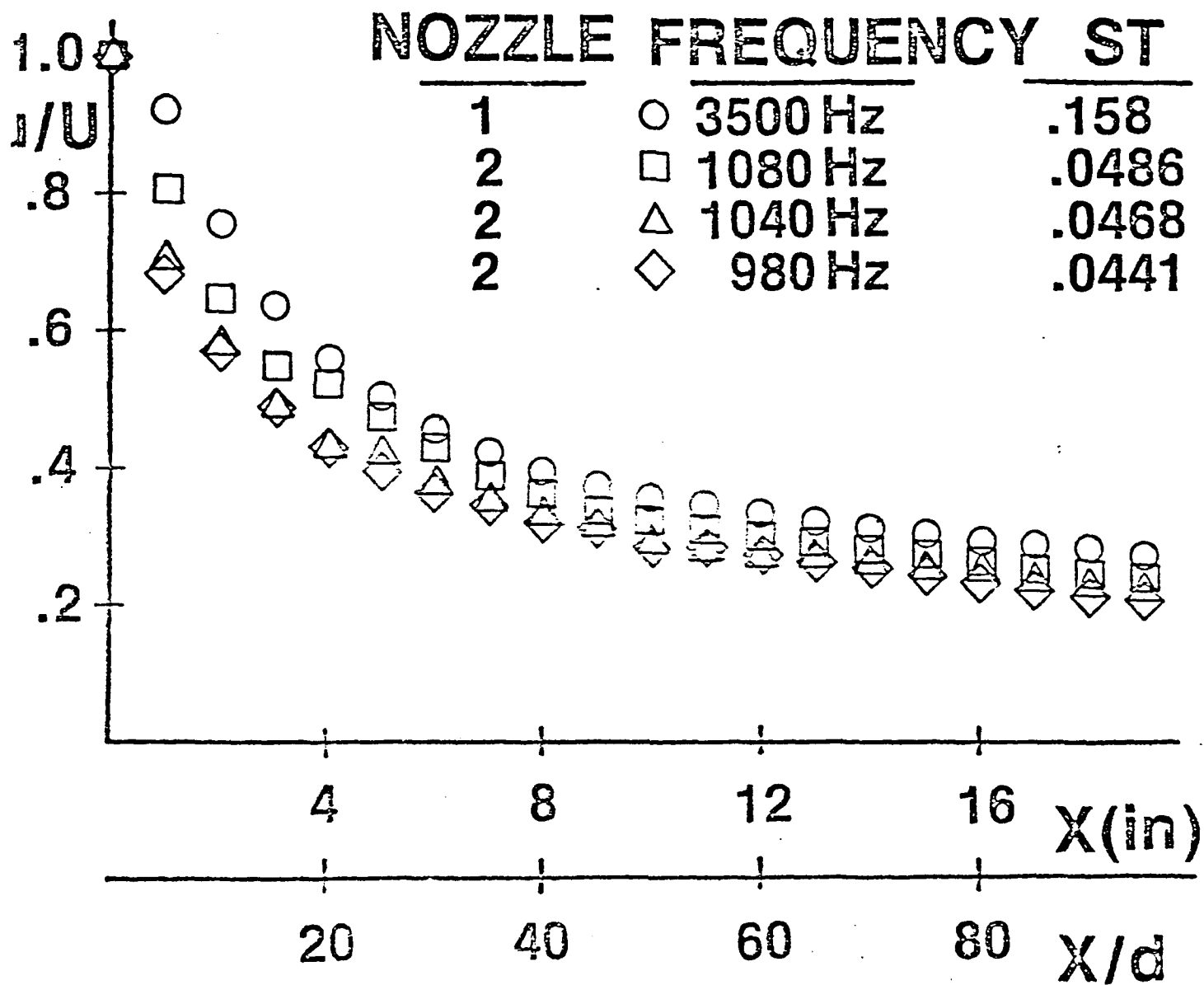
Figure 8. Velocity decay for unsteady jet flows.
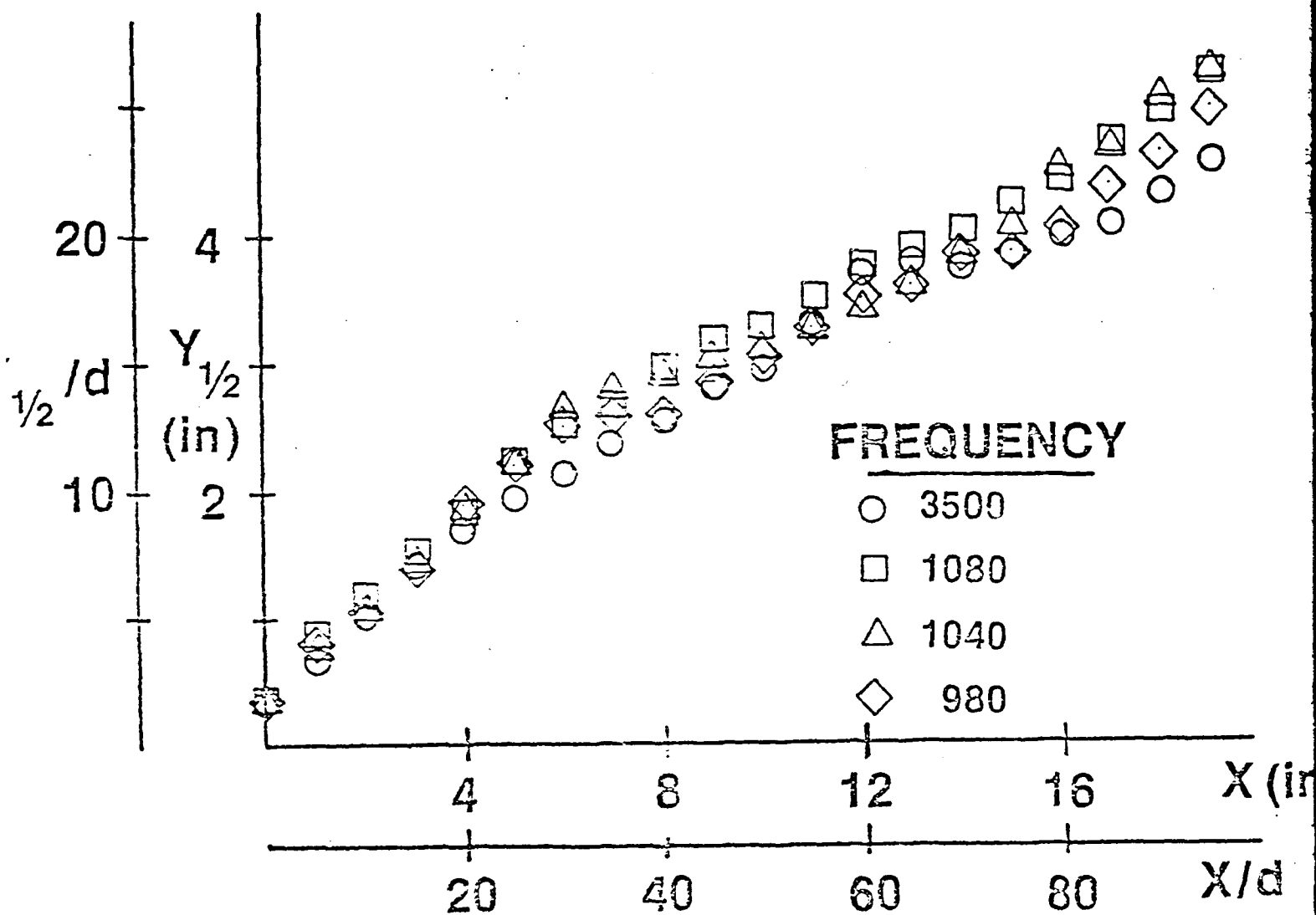
Figure 9. Half width growths for unsteady jet flows.
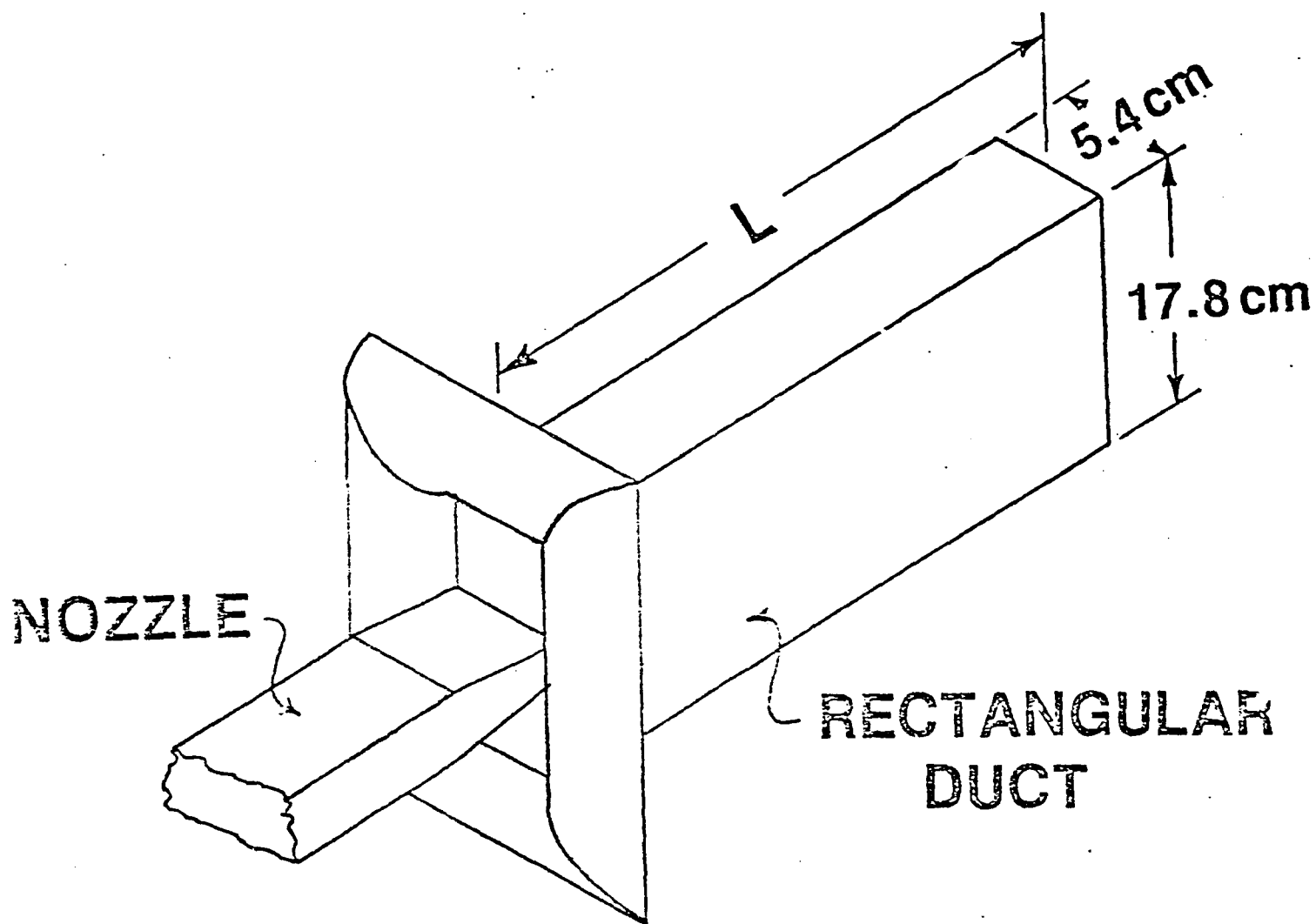
Figure 10. Schematic of the acoustic ejector experiment.
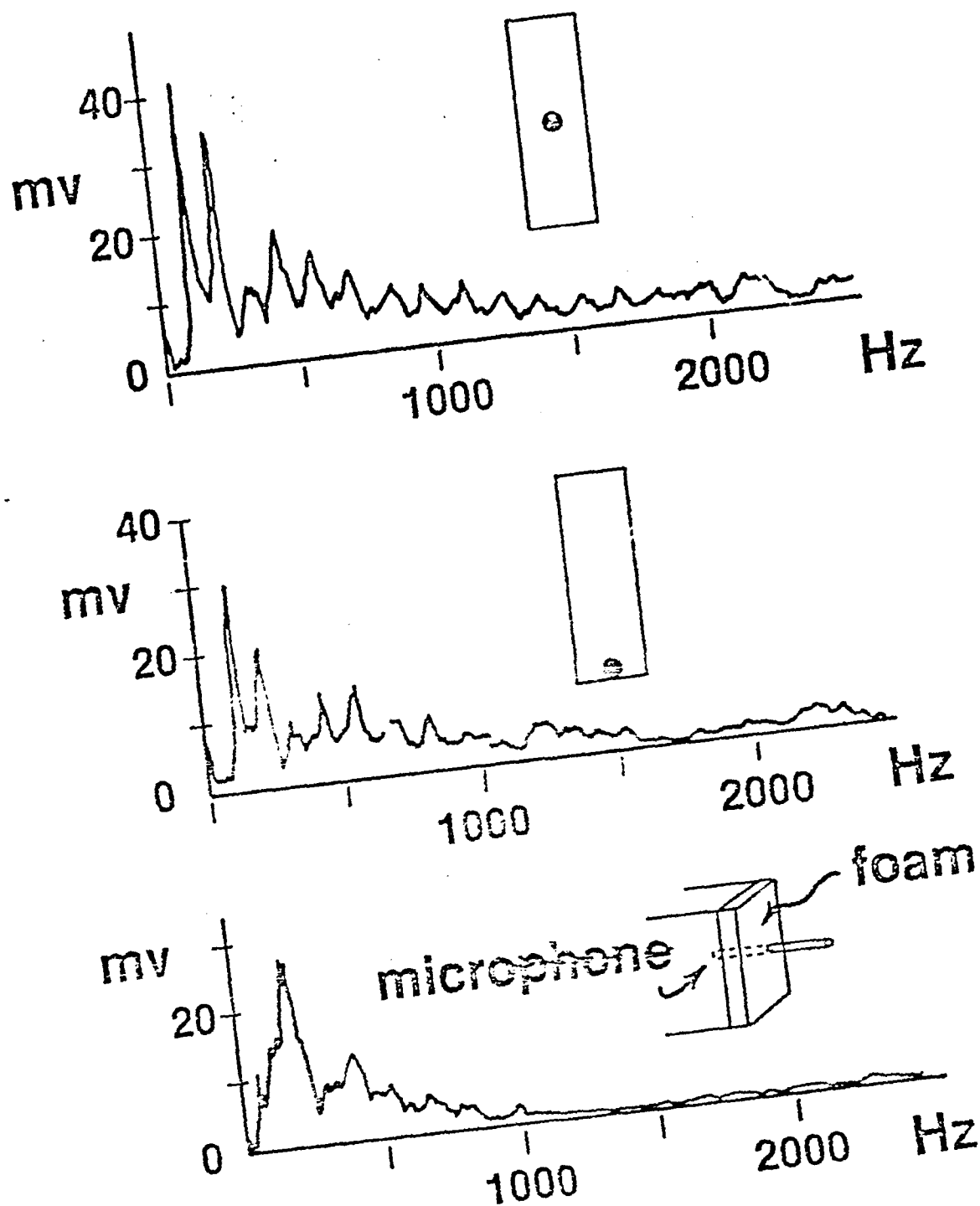
Figure 11. Frequency spectra with the microphone at two locations at the duct exit and with foam at the exit plane.
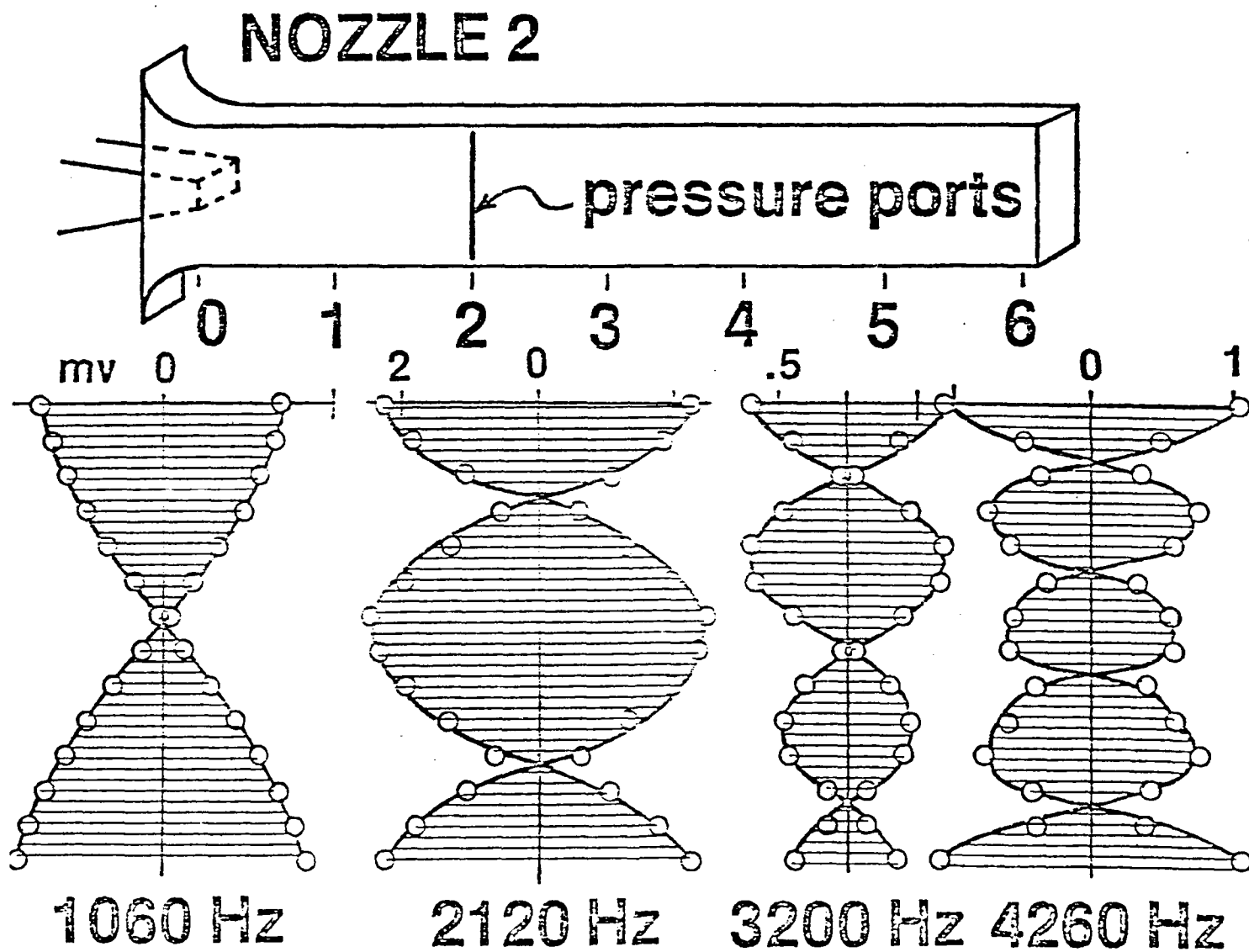
Figure 12.   Pressure level distributions of the lower
frequency components (taken at X/D = 2, across
the longer duct width), Nozzle 2, L/D = 6.1.

NOZZLE 2 pressure ports

0   1   2   3   4   5   6

5   0   5   2   0   2   1   0   1   1   0   1

060 Hz   2120 Hz   3200 Hz   4260 Hz
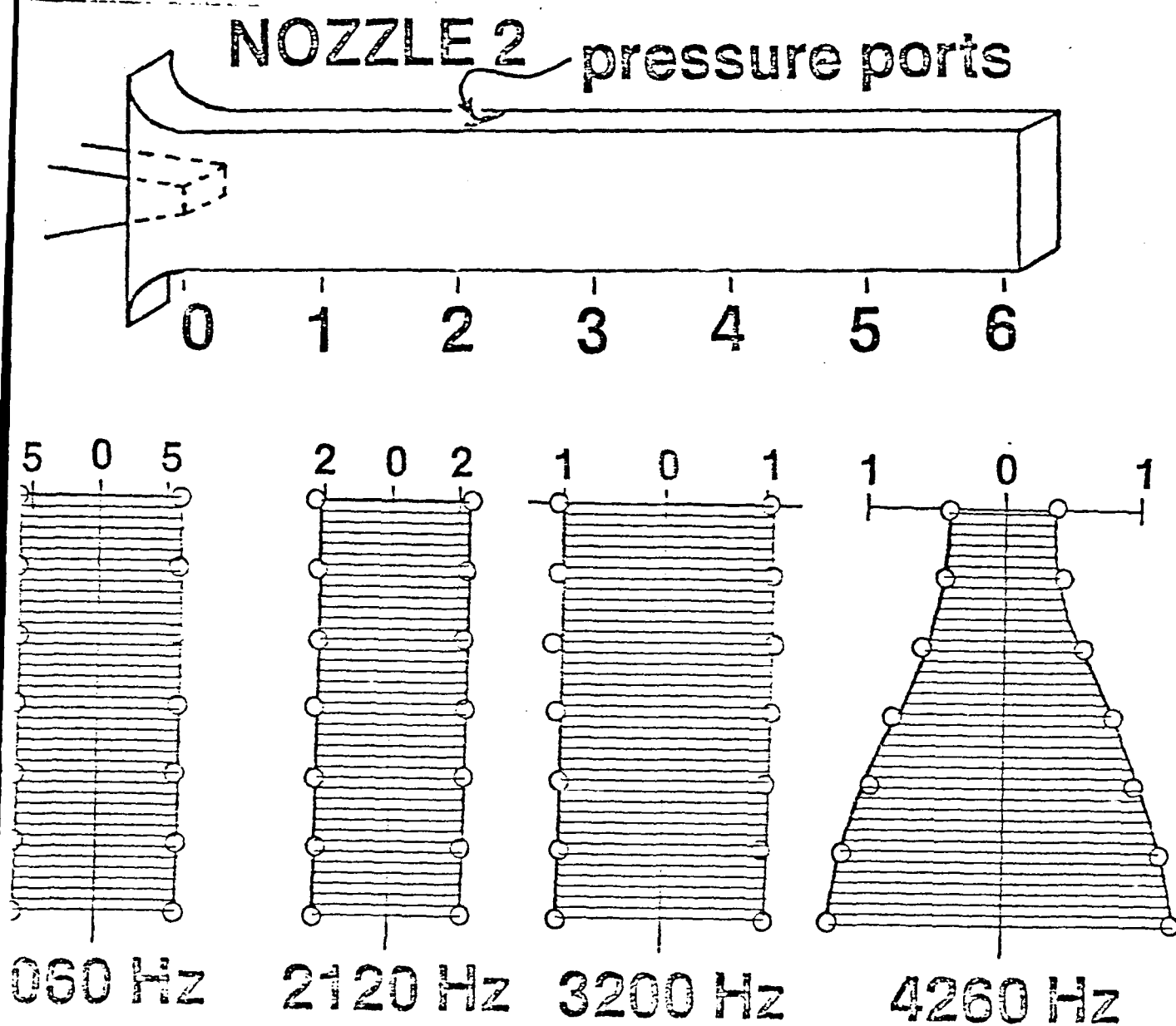
Figure 13. Pressure level distributions of the lower
frequency components (taken at X/D = 2, across
the shorter duct width), Nozzle 2, L/D = 6.1.

NOZZLE 2

pressure ports .28

0 1 2 3 4 5 6

10 mv 0   10   6 0 6   1   0   1   1 0 1

1060 Hz   2120 Hz   3200 Hz   4260 Hz
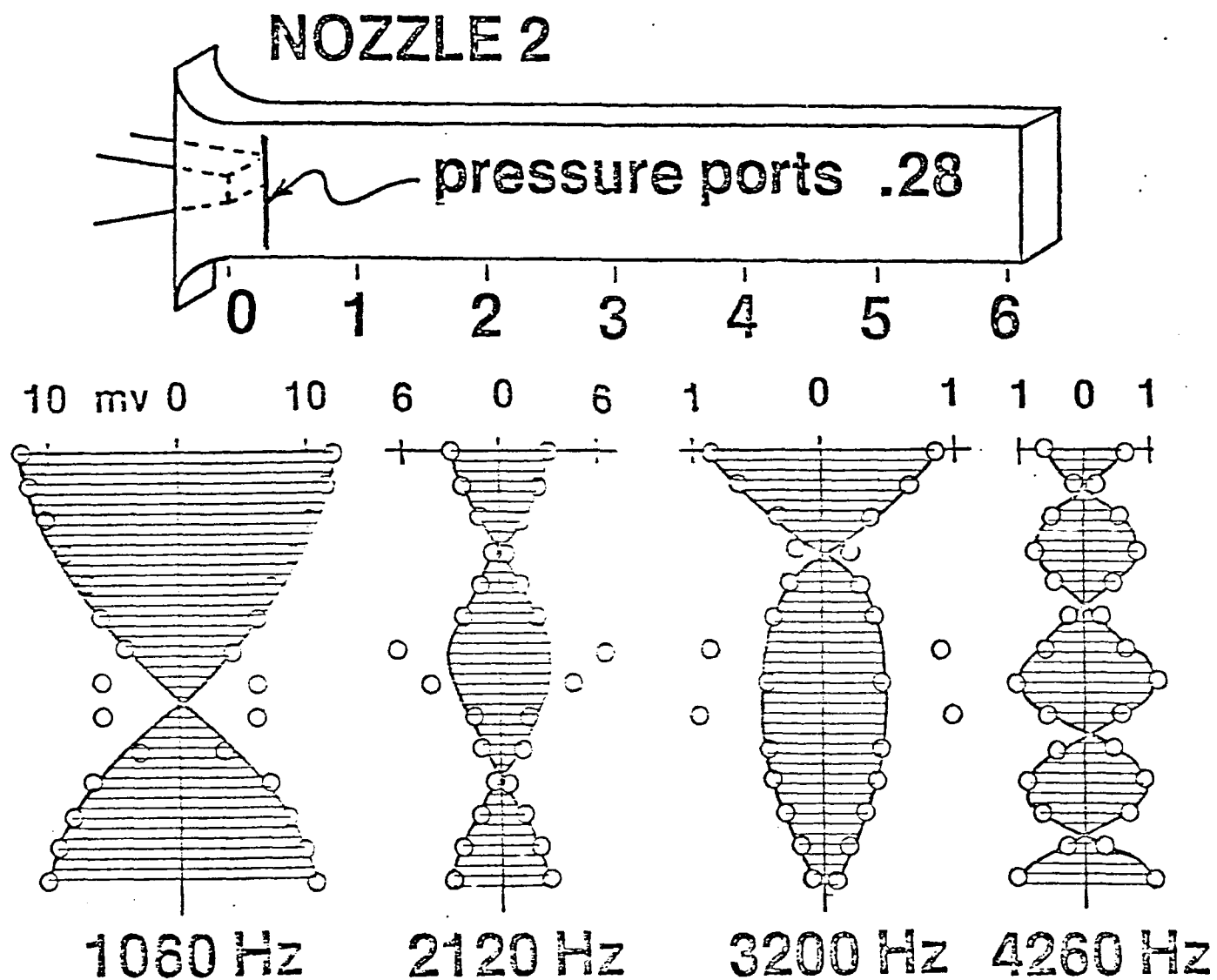
Figure 14.

Pressure level distributions of the lower frequency components (taken at X/D = .28, across the longer duct width), Nozzle 2 L/D = 6.1.

NOZZLE 2

pressure ports

0   1   2   3   4   5   6

10   0   10   3   0   3 1   0   1 1   0   1

1060 Hz   2120 Hz   3200 Hz   4260 Hz
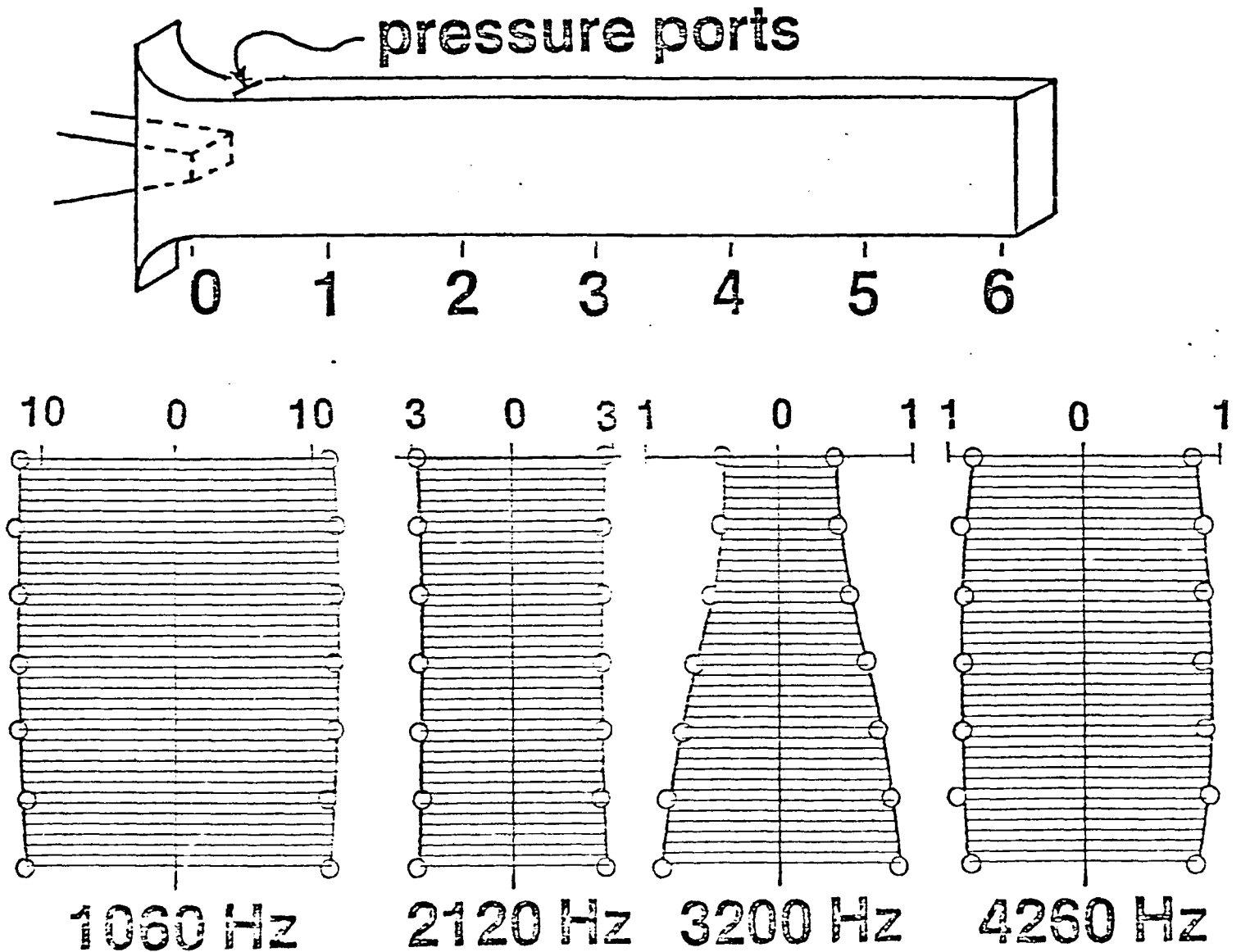
Figure 15. Pressure level distributions of the lower frequency components (taken at S/D = .28, across the shorter duct width), Nozzle 2, L/D = 6.1.
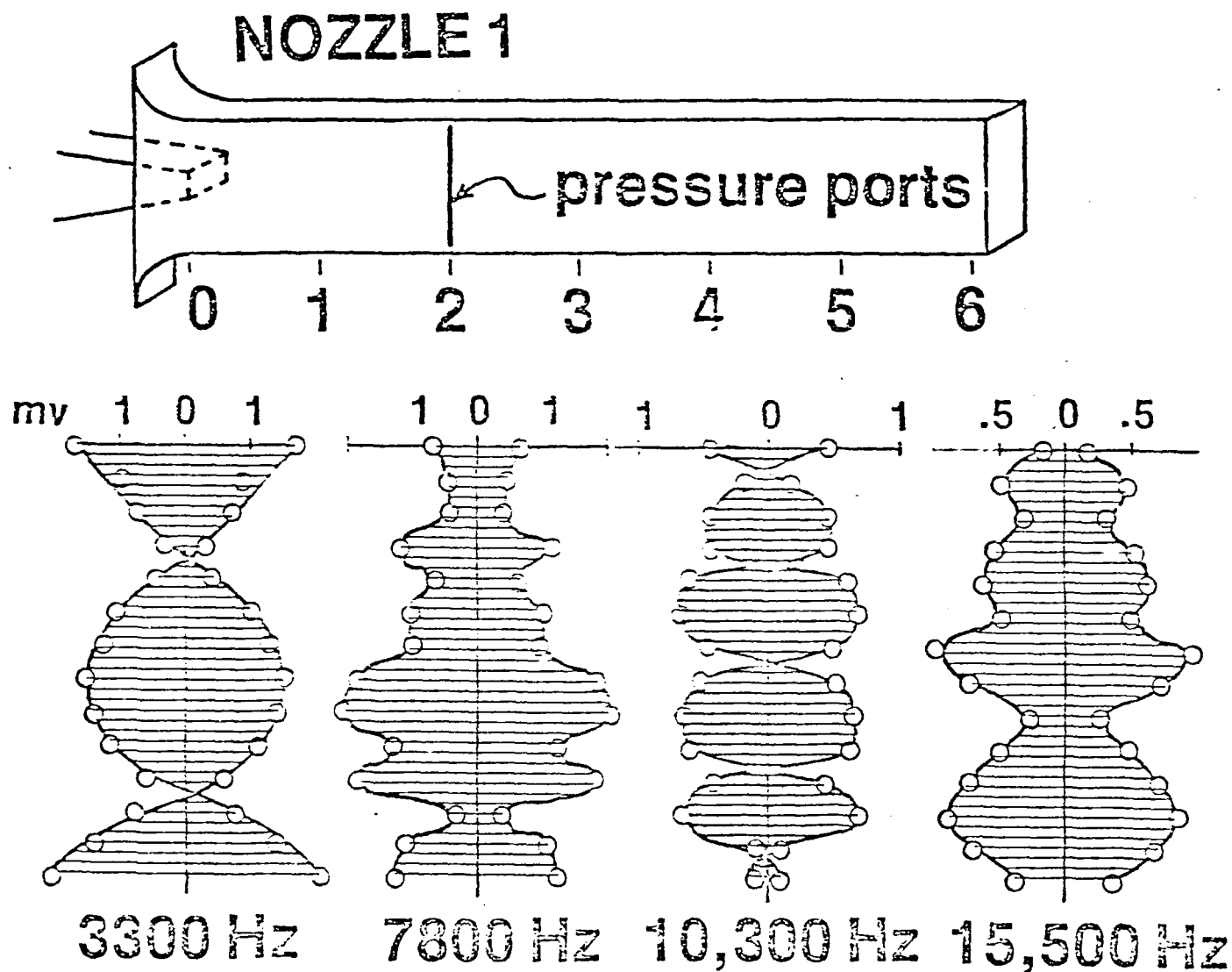
Figure 16. Pressure level distribution of the lower frequency components (taken at X/D = 2, across the *longer* duct width), Nozzle 1, L/D = 6.1.

NOZZLE 1

pressure ports

0 1 2 3 4 5 6

3300 Hz   7800 Hz   10,300 Hz   15,500 Hz
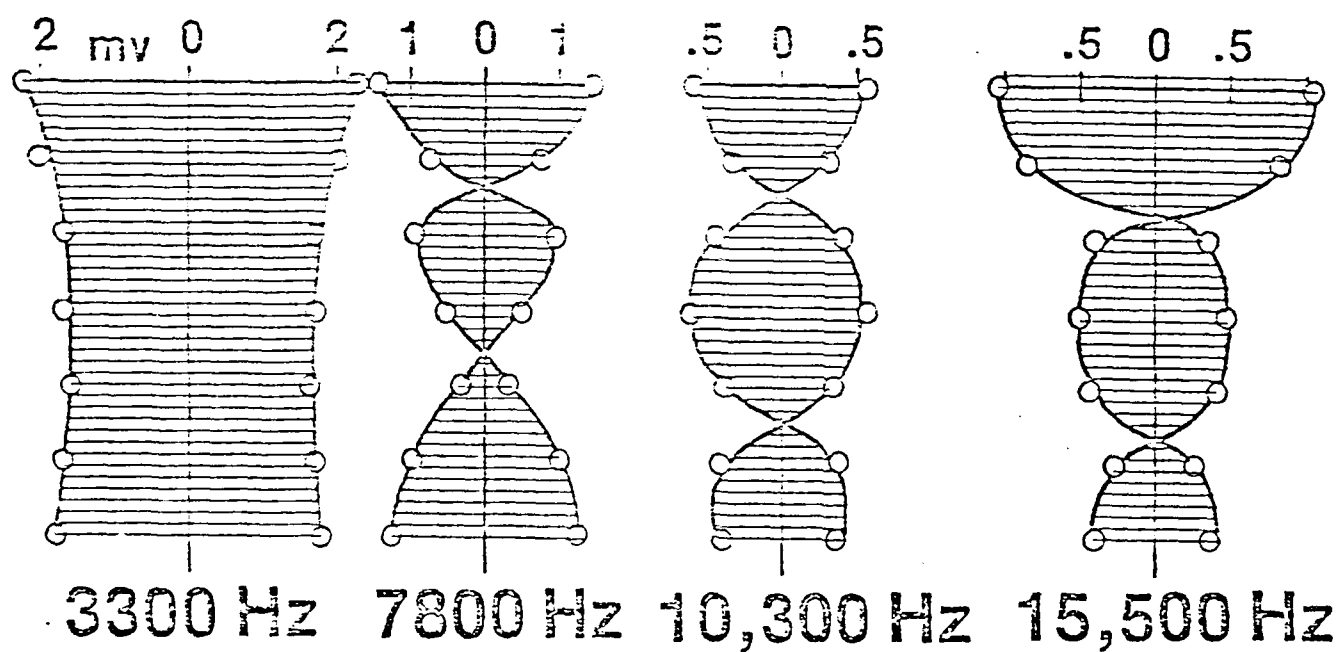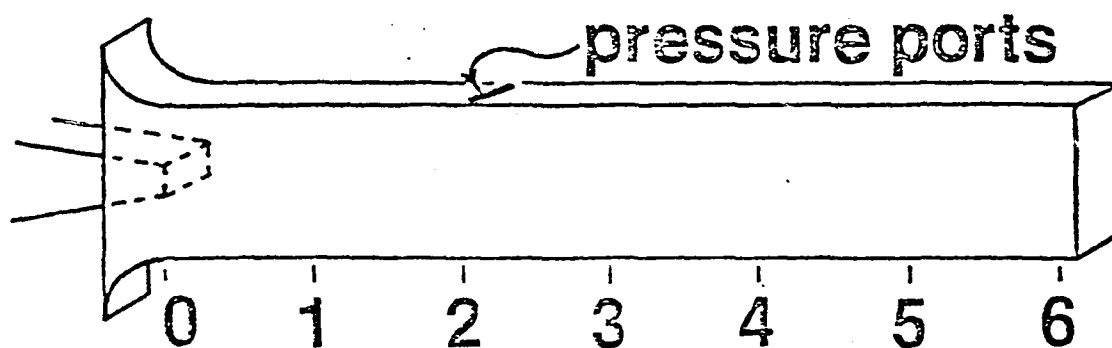
Figure 17.   Pressure level distributions of the lower
frequency components (taken at X/D = 2, across
the shorter duct width), Nozzle 1, L/D = 6.1.
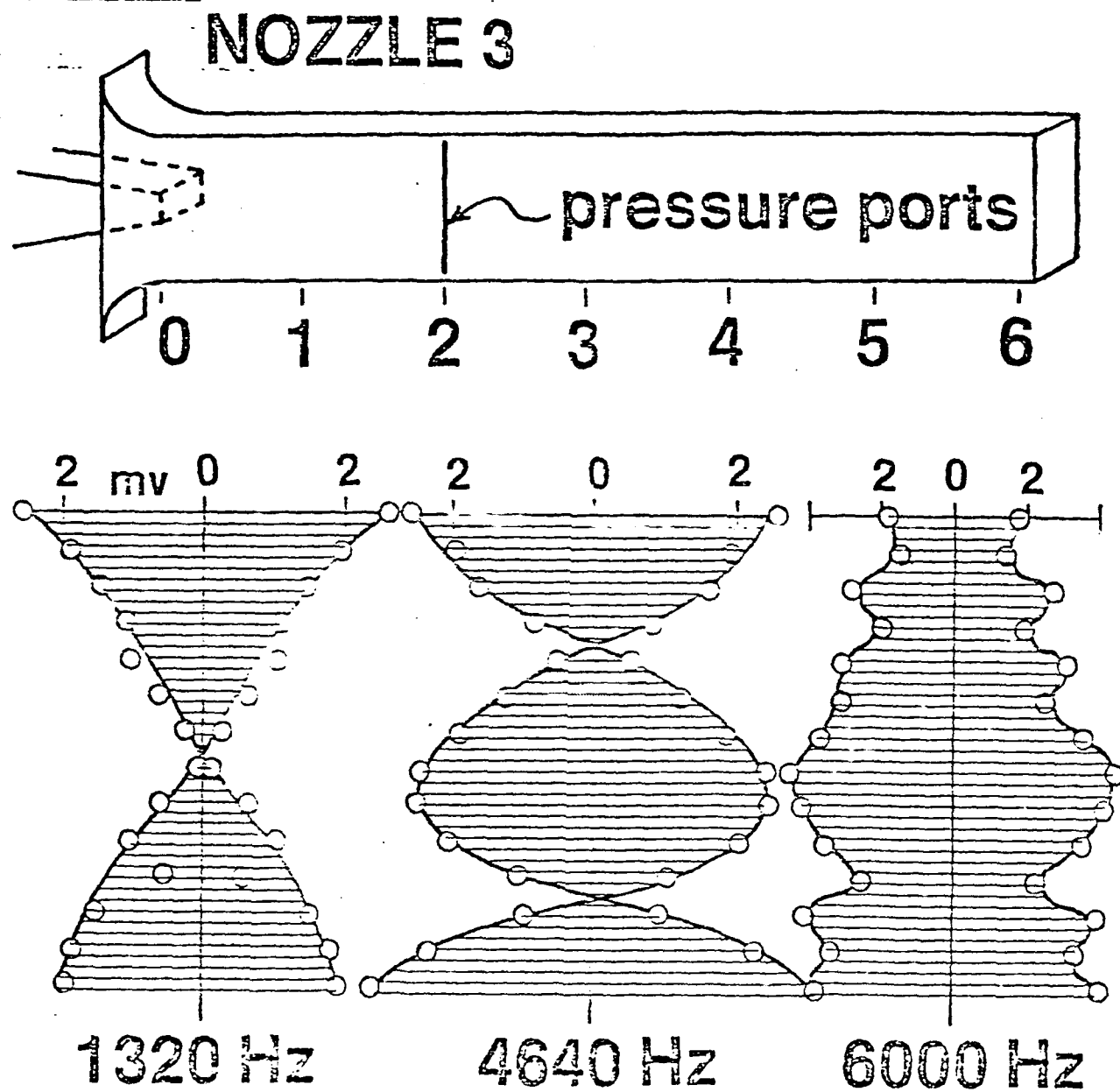
Figure 48. Pressure level distributions of the lower frequency components (taken at X/D = 2, across the longer duct width), Nozzle 3, L/D = 6.1.

NOZZLE 3
pressure ports

0 1 2 3 4 5 6

mv 2 0 2   3 0 3   4 0 4

1320 Hz 4640 Hz 6000 Hz
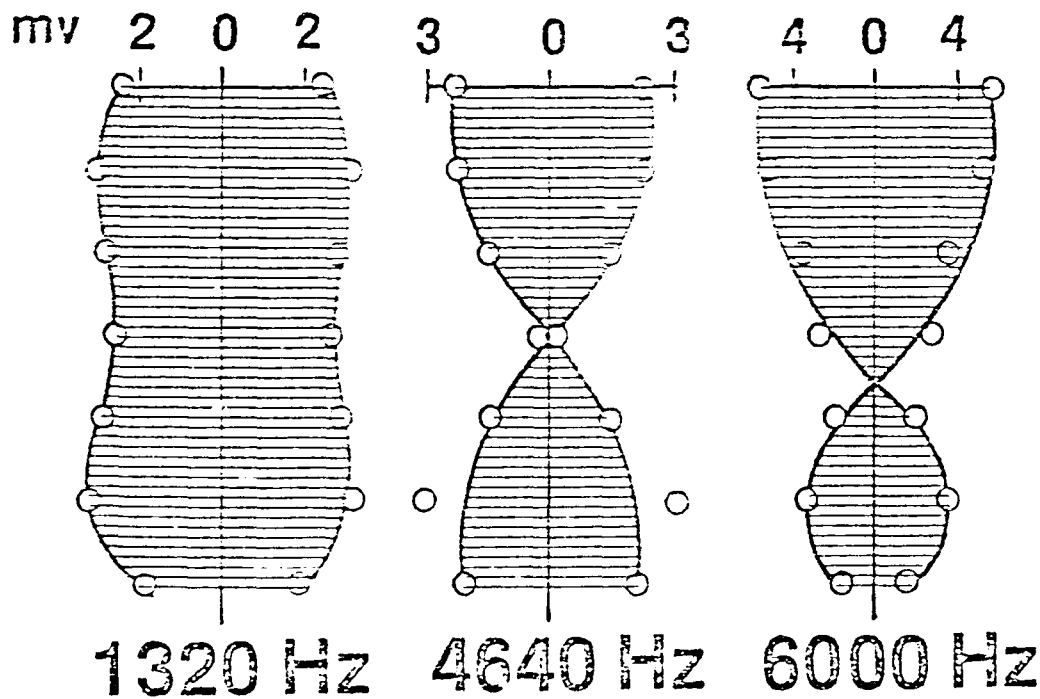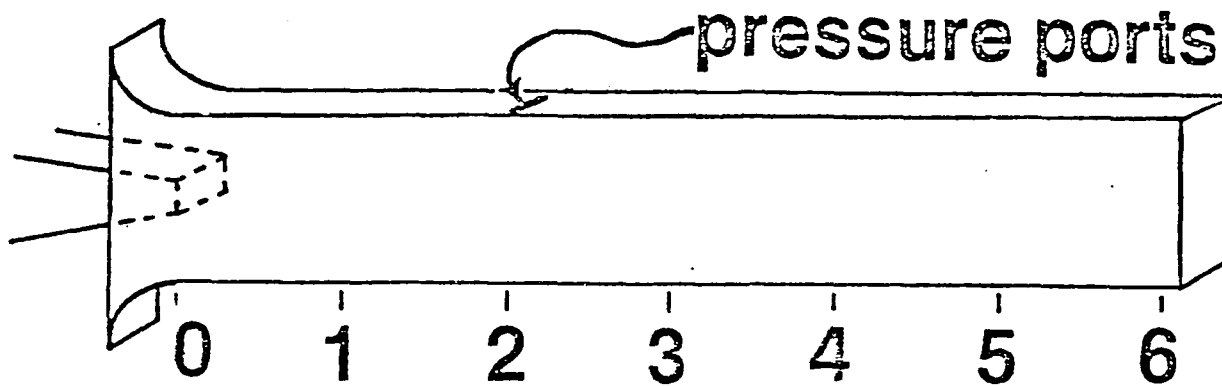
Figure 19. Pressure level distributions of the lower
frequency components (taken at X/D = 2, across
the shorter duct width), Nozzle 3, L/D = 6.1.
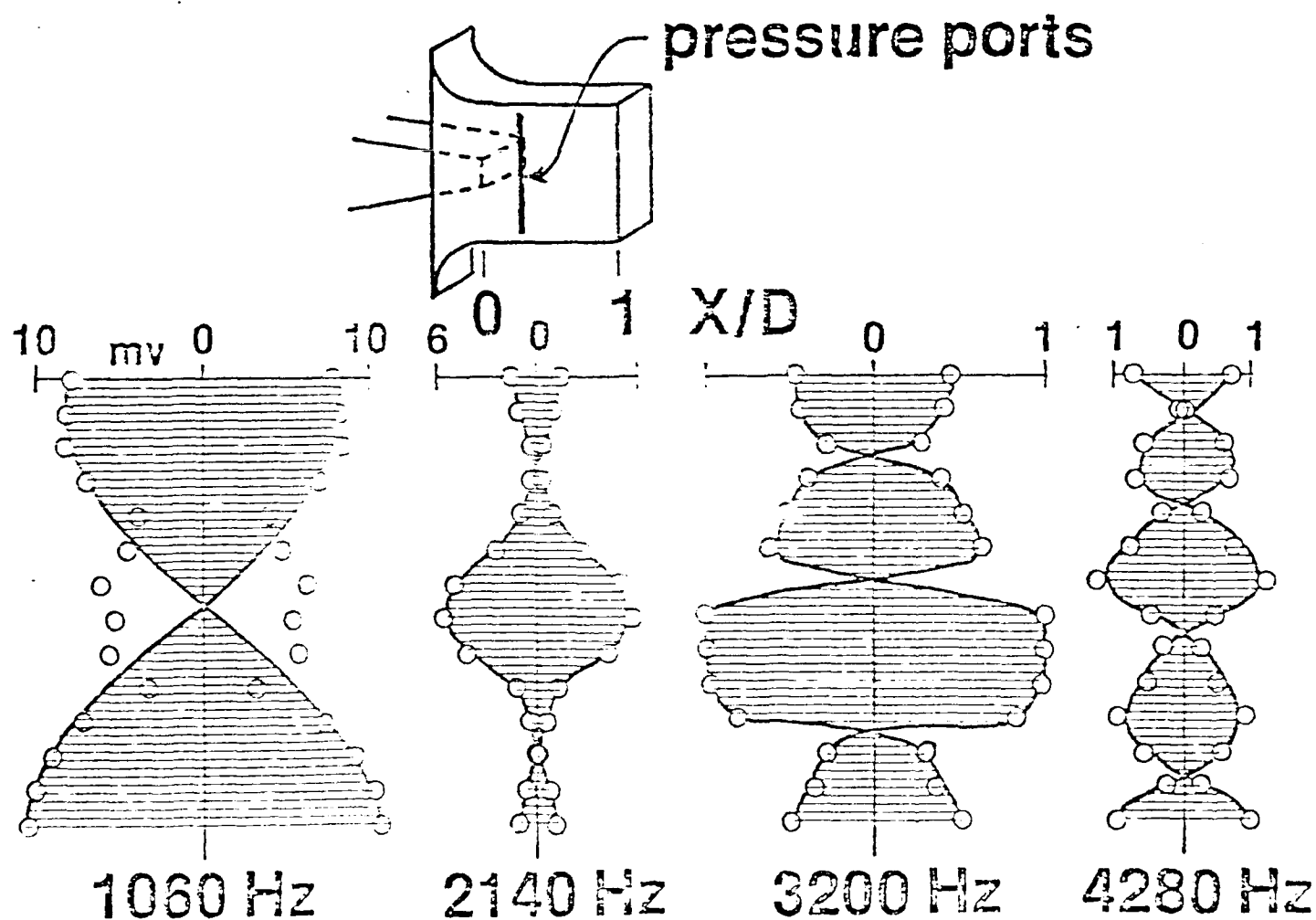
Figure 22. Pressure level distributions of the lower frequency components taken at X/D = .28, across the inner duct width, Nozzle 2, L/D = 1.
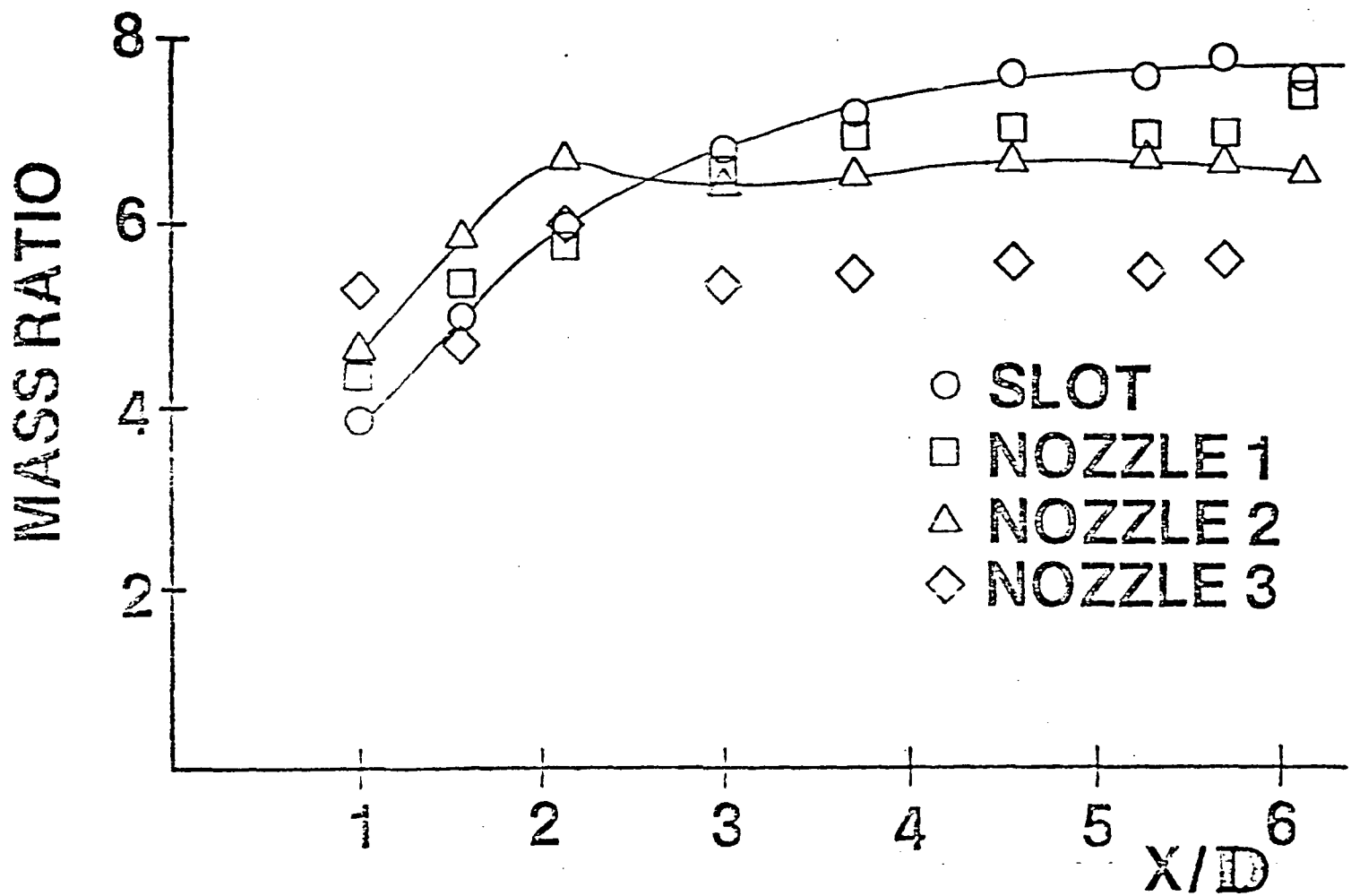
Figure 21. Mass ratio = exit mass flow/primary mass flow, as a function of duct length.

Three Dimensional Vortex Dynamics Near a Wall[+]

Hermann Viets[*]
West Virginia University
Morgantown, WV 26506

Richard J. Bethke[**] and David Bougine[***]
Wright State University
Dayton, Ohio 45435

Abstract

The three dimensional deformation of a line vortex near a flat wall is examined by means of flow visualization and quantitative conditioned sampling of a hot wire anemometer. The vortex is observed to undergo a very rapid deformation from the rectilinear form to a very high aspect ratio hairpin-like shape. Similar shapes have been observed in the case of driven flows in a laminar boundary layer. In the present case the vortices are driven by a rotor configuration.

General Background

The dynamics of vortex structures has been of interest to many researchers for a variety of reasons. Much of the early interest was analytical and motivated by the ability to model the structure in terms of inviscid hydrodynamics.[1] The ideal vortex structures were even employed at one point as a model for atomic structure[2] and successfully predicted some of the earlier observations of atomic physics. Multiple vortex interactions were also computed[3,4] and in some cases stability analyses were performed to reveal

---

potential naturally occuring vortex configurations, for example the series of axisymmetric ring vortices shown in Figure 1. Of course the most successful application of inviscid vortex structures to predict observed a .phenomenon is the well known Karman Vortex Street analysis.[5] Karman was able to predict, by actually computing the effect of a number of fortices on each other, that only a very specific spacing of vortices, shown in Figure 2, would yield a stable configuration.

Most of the early vortex analyses and experiments concerned free vortices (i.e. those removed from wall boundaries). This allowed the structure to be treated inviscidly by methods outlined by Lamb[1] and others[6]. Most of these vortex structures were ring vortices and these have been reviewed by Zaroodny[7].

The dynamics of vortex ring motion has been analyzed inviscidly by Arms and Hama.[8] An experimental and analytical treatment was performed by Viets and Sforza[9] who employed a viscous model due to Rankine[10] and a time dependent viscous model due to Hamel[11] and Oseen[12]. More recent fully viscous analyses are due to Widnall[13] and Saffman[14] and have been reviewed by Saffman and Baker[15].

The objective of the present paper is to examine the three dimensional vortex dynamics near a wall. The motivation behind looking at the methods employed for the prediction of vortex dynamics far from a wall is simply that these methods will be directly applicable ′   . is willing to model the wall in an inviscid fashion. Thus the inviscid wall would amount to a plane of symmetry in the analysis.

Vortex Near a Wall

The initial studies of vortex structure near a wall were driven by the interest in boundary layer transition. The initial stability predictions of Tollmien[16] and later Schlichting[17] were verified by the classical experiment

of Schubauer and Skramstad[18] who employed an electromagnetically oscillating ribbon in a laminar flow. The magnitude and frequency of the oscillation were controlled as well as the Reynolds number of the flow. The results, in terms of a stability diagram, are very well predicted by Tollmien's analysis (see Reference 16, pg. 460).

Even more interesting, from the point of view of vortex dynamics in the vicinity of a wall, is the structure of the unsteady flow produced near the surface. As calculated by Schlichting[19] for a neutral (i.e. neither growing nor decaying) disturbance, the closed streamlines exhibit a vortex-like structure which is convected in the streamwise direction and shown in Figure 3. This structure has been named Tollmien-Schlichting waves. Some excellent photographic evidence of this structure behind a driven oscillating ribbon of the type employed by Schubauer and Skramstad[18] has been obtained by Wortmann, who employed ink and water to generate the streakline pattern shown in Figure 4.

The deformation process of a straight vortex line of the Tollmien-Schlichting type has been illustrated by Hinze[21] and is shown in Figure 5. The vortex distorts slightly and this small distortion is amplified by the self-induced velocity distribution set up by the vortex. The region of highest curvature of the vortex has the highest self-induced velocity[8]. Thus the loop in the vortex is propelled fastest from the wall and thus finds itself in a higher streamwise velocity region. The loop is then convected faster in the streamwise direction than the straight portion deeper within the boundary layer and the vortex filiment is stretched until, by a mechanism which is not fully understood, it is said to "burst". This mechanism is currently being called into question as the actual process leading to boundary layer transition. Some recent evidence indicates that the initially turbulent region (or "spot") is actually composed of numerous vortex filiments instead of a single deformed

vortex. However, from the present point of view of vortex dynamics near a wall, the model still offers a rational deformation process in a boundary layer.

Some especially good photographs of the deformation of an initially rectilinear vortex, again behind a vibrating ribbon, have been obtained by Wortmann[5] employing the pulsed hydrogen bubble technique and an example is shown in Figure 6, a view of the deformed vortex loop from above (looking down perpendicularly to the plate).

In the deformation model proposed by Hinze[21], shown in Figure 5, the expected streamwise velocity profiles through the centerline of the deformation are shown at various streamwise positions and compared to the typical boundary layer type of profile. Actual velocity profiles of this type have been measured by Muiswinkel[22], again behind an oscillating ribbon, and are shown in Figure 7 for various times during one oscillation of the ribbon.

The objective of the portion of the study described on the following pages is to identify the deformation of an initially rectilinear vortex structure near a wall. The two techniques employed in the study are flow visualization and conditioned sampling of a hot wire anemometer signal.

Flowfield Geometry

Various techniques are possible to generate the initially rectilinear vortex. The vibrating ribbon employed by Schubauer and Skramstad[18] is one possibility which has been discussed. However, in the present experiment, the objective is to operate at a larger scale than the previous vibrating ribbon experiments. Another possibility is a technique employed by Francis et. al.[23, 24] in their study of vorticity generated on the upper surface of an airfoil. The basic mechanism is a plate, positioned perpendicularly to the surface, which alternately extends from and retracts into the surface. Each time the plate is extended it creates a recirculation region behind itself

and this region is shed and convected downstream when the plate is retracted into the surface.

From the present point of view, it is desirable to have control over the strength of the vorticity produced and thus the flat plate is rejected in favor of the rotor geometry shown in Figure 8. The rotor has discontinuity in its radius at the cusp shape. The mean flow is from the left and the rotor turns in a counter clockwise direction. The rotor tip appears periodically above the surface and each time the cusp tip is exposed to the mean flow, a transverse vortex (turning in the clockwise direction) is produced lying parallel to the surface and perpendicular to the mean flow. The strength of the vortex so produced is proportional to the relative velocity between the rotor tip and the mean flow. Thus control over the vortex strength can be achieved by simply changing the rotational speed of the rotor, including the possibility of turning the rotor in a clockwise direction.

The rotor geometry in Figure 8 has been employed to study the vorticity produced as a quasi-two-dimensional structure[25]. Only centerline data was taken and the trajectory of the vortices produced is shown in Figure 9 for a rotational speed of w = 3000 rpm counter clockwise. Both axes have been nondimensionalized with respect to the maximum height that the rotor extends above the surface, H in Figure 8.

In addition to a detailed examination of the vortex structure produced by the rotor, the geometry has been applied to various problems as shown in Figure 10, including the control of the flow over an airfoil[26], avoiding separation over a rearward facing ramp[27], driving the flow in a dump combustor[28] and studying the properties of convected structures[29]. Each of the potential applications will be strongly effected by the three dimensional nature of the vortex flow.

Since the data shown in Figure 9 was obtained, the wind tunnel has been rebuilt and usable test section length tripled. The objective is to determine the three dimensional character of the vortex structure and to follow that structure farther downstream then previously possible.

Flow Visualization Results

a. The choice of rotor speed.

The visualization of the flowfield is accomplished by the use of entrained kerosene vapor. The kerosene is vaporized by slowly dripping it on an inclined heated flat plate where it is vaporized and forced through a series of tubes which end at the inlet to the wind tunnel. Here the vapor is entrained into the tunnel, yielding the streaklines of the flowfield.

The initial results in the rebuilt wind tunnel are shown in Figures 11 - 14, at the same conditions as tested in Reference 25, a rotational speed of $w = 3000$ rpm in the counterclockwise direction.

The results have been obtained at specific phase angles, for example Figure 11 shows the flowfield for a phase angle $\theta = 0^{\circ}$ which means the rotor is in the upright or fully extended position, as may be seen in the first photograph of the Figure. The photographs are arranged such that the fields overlap each other. Thus portions of the photographs that lie under each other indicate a region of overlap.

The first conclusion drawn from Figures 11-14 is that the scale of the vortex disturbance is rather large. The transverse scale of the tunnel, from the lower wall to the top, is 30 cm. In Figure 11, the scale of the vortex at a position of roughly one transverse scale downstream can be estimated to be 15 cm. That this estimate is accurate may be seen from Figure 10 of Reference 25. Farther downstream in Figure 10 (for a phase angle of 0°) the scale becomes substantially larger. The same effect may be seen in the results at a later

phase angle ($\theta = 120^{\circ}$) in Figure 11. The newly formed vortex near the rotor has a scale of perhaps one-fourth of the transverse value but grows very rapidly. In the yet later phase angles the development of the vortex may be followed in the streamwise direction and it is clear that the overlapping photographs yield the same structure in either case.

There are two problems with the 3000 rpm results from the point of view of studying the three dimensional vortex structure. One is that the scale is too large, making it difficult to follow the details of the rather diffuse vortex. The second is that the vortices are relatively closely spaced, being only one transverse scale apart. This might create some problems in detecting influences of one vortex on another. For these reasons it was determined that a lower frequency would be preferable. In addition, a well formed vortex was desired which led to the study illustrated in Figure 15.

At a phase angle of $\theta = 30^{\circ}$ the rotor position is such that the cusp point is rotated 30° from the upright position. For various rotational speeds, the flowfields are shown in Figure 15, varying between -600 and -3000 rpm. In each case it is clear that a vortex rotating in the clockwise direction is produced, indicating that the freestream velocity, nominally 12 m/sec, is greater than the tip speed of the cusp shape. A possible exception is the case at -3000 rpm where the vortex is very weak or non-existent since the ti, speed is approximately equal to the nominal free stream velocity.

From Figure 15, the choice of a rotational speed is made. The objective is a well formed vortex with a scale that is reasonable for the tunnel scale. A rotation speed of -1600 rpm is chosen on this basis.

b. Vortex generation.

The vortex generation process employing the rotor turning in the clockwise direction at 2000 rpm and the flow from the left is shown in Figure 16 for various phase angles. At zero degrees the curling up of the

smoke streaklines behind the cusp shape is clear. A secondary frequency is
evident on the smokeline and may be related to an instability of the flow.
As the phase angle increases, the vortex moves downstream and at a phase angle
of 45° the vortex interacts with the corner of the downstream plate behind
the rotor. By a phase angle of 67.5^o the vortex is more clearly defined and
by 90° the vortex is no longer evident. This is the first indication of the
three-dimensionality of the flow, since the plane in which the photographs are
taken is not the centerline of the tunnel but rather a plane closer to the far
wall.

The data planes considered in the present investigation are shown in
Figure 17. In addition to the centerline plane, there are planes at five
and ten centimeters to either side of the centerline. The photographs of
Figure 16 are taken in plane -4 (i.e. four inches from the centerline). The
reason that the vortex appears to disappear into a cloud of smoke at a phase
angle of 90° is simply that the vortex axis has shifted to an orientation
closer to perpendicular to the wall.

c. Flowfield for $\theta = 0^o$

Figures 13-22 illustrate the streaklines in the flowfield for a phase
angle of 0° (i.e. the rotor in the fully extended position) and in the various
planes shown in Figure 17. In each plane the curling behind the rotor is
evident and in the centerline case, Figure 20, a vortex is clear at 70 cm
downstream and approximately 12 cm off the wall (See vortex A). Looking for
this vortex in the $\pm$ 2 and $\pm$ 4 planes shows in the $\pm$ planes, the presence
of the vortex is clear while in the $\pm$ 4 planes only the secondary effect of
the vortex is evident, i.e. the curved streaklines in Figure 18. Thus the
vortex is perpendicular to the plate in the $\pm$ 2 planes.

d. Flowfield for $\theta = 90^o$

For a phase angle of 90° the streaklines in various planes are shown
in Figures 23-27. The vortex located immediately behind the rotor in the

last sequence has now moved to position B in the centerline photograph of Figure 25. In the $\pm$ 2 planes, the effect of this vortex may be seen while in the $\pm$ 4 planes the effect is small but present. Thus the vortex appears to assume a three dimensional shape very rapidly, in this case within a quarter rotation of the generator. The downstream vortex ("C") has moved to 80 cm. downstream and 15 cm. above the wall. Again, the effect of this vortex is very small in the $\pm$ 4 planes but quite clear in the $\pm$ 2 planes.

e. Flowfield for $\theta = 120°$ and $\theta = 180°$

The vortex presence is located by D & E at $\theta = 120°$ and F at $\theta = 180°$ in Figures 28-37. In each case the vortex has moved farther downstream, so that at $\theta = 180°$ only one vortex is evident in the field, approximately 30 cm. downstream. The presence of the weak vortex lying right on the wall itself is clear in the -4 plane at approximately 25 cm. downstream. Thus the dynamics of the vortex process involve a violent curling up and distortion of the control portions of the originally rectilinear vortex but a weak remainder of the vortex which continues to move near the wall.

f. Flowfield for $\theta = 240°$ & $\theta = 270°$

By a phase angle of $240°$, the vortex in the centerline plane has moved to a streamwise position of 40 cm and a height of 10 cm. as denoted by position in Figures 38-42. The presence of the vortex is strongly felt in the centerline plane (Figure 40) and still clear in the $\pm$ 2 planes. Farther from the center-line only a slight effect is seen, consistent with a weak vortex still moving near the wall. Some evidence of a secondary vortex ("H") may be seen at approximately 90 cm. This effect may be due to the fact that at certain speeds the rotor may shed more than one vortex per cycle. This effect was observed during some studies of a rotor positioned on the back of a van as well as on the back of a car[30]. The secondary vortex has also been seen in the case of an oscillating orthogonal plate[24].

The same general effect is evident in the case of a phase angle of 270°

Figures 43-47. The vortex ("I") is identified at a streamwise position of

50 cm, 5 cm above the plate. Again the vortex is strong on the centerline,

smeared at the ± 2 positions and weak and near the wall away from the

centerline.

g. Conclusions based on flow visualization.

The flowfield structure depicted by the visualization results of

Figures 18-47 can be summarized by Figure 48. The initially rectilinear

vortex deforms very rapidly as it is convected downstream. Initially there

is some evidence that the vortex lines extend out to the front and back walls

of the tunnel. However, farther downstream the connection is tenuous and it

is possible that the vorticity lines end on the surface of the flat plate

instead of the wind tunnel walls.

It is probably that the single deformed vortex is due to the end conditions

on the wind tunnel walls. That is, if the rotor were infinitely long, the

initially rectilinear vortex would still deform into a similar pattern as that

in Figure 48 and that the pattern would be repeated with a certain scale length

which would be determined by a question of the stability of the rectilinear

vortex to an applied disturbance. In the real experimental case, the applied

disturbance is the end walls which supply a boundary layer which will cause

the vortex ends to move downstream more slowly than the vortex center. This

initial deformation then progresses into the shapes observed. The aspect

ratio of the deformed vortex (i.e. its height above the plane/distance between

the legs perpendicular to the plate, is approximately unity by 30 generator

heights downstream.

References

1. Lamb, Jir H., _Hydrodynamics_, Cambridge University Press, London, 1932; reprint; Dover Publication Inc., New York, 1945.

2.

3. Levy, H. and Forsdyke, A.G., "The Stability of an Infinite System of Circular Vortices,

4. Levy, H. and Forsdyke, A.G., "The Vibrations of an Infinite System of Vortex Rings"

5. Karman, Th. Von, "Uber den Mechanismus des Widerstandes, denein bewegter Korper in einer Flussigkeit erfahrt," Gottinger Nachrichten, mathematisch-physikalische Klasse, 1911, pp. 509-511.

6. Karamcheti, K., _Principles of Ideal-Fluid Aerodynamics_, John Wiley and Sons, Inc., New York, 1966.

7. Zaroodny, S. J., "Revised Theory of Vortex Rings- a simplified review of the state of the art," U.S. Army Limited War Laboratory, T. M. 66-01, April 1966.

8. Arms R.J., and Hama, F. R., "Localized Induction Concept on a Curved Vortex and Motion of an Elliptical Vortex Rings," Physics of Fluid, April 1965, pp. 553-559.

9. Viets, H. and Sforza, P. M., "Dynamics of Bilaterally Symmetric Vortex Rings," Physics of Fluids, Vol. 15, No. 2, Feb. 1972.

10. Rankine, W.J.M., _Manual of Applied Mechanics_, C. Griffen and Co., London, 1st Edition, 1858.

11. Hamel, G., "Sprialformige Bewegung zaher Flussigkeiten," Jahesberd. Dt. Methematiker-Vereinigung 34(1916).

12. Oseen, C. W. Ark. f. Math. Astron. och. Fys. $\underline{7}$, 1911; Hydromechanik p. 82, Leipzig 1927.

13. Widnall, S.E., "The Structure and Dynamics of Vortex Filiments," Annual Review of Fluid Mech., Vol. 7, 1975, pp. 141-165.

14. Saffman, P. G., "The Number of Waves on Unstable Vortex Rings", J. Fluid Mech., Vol. 84, 1978, pp. 625-639.

15. Saffman, P. G. and Baker, G. R., "Vortex Interactions", Annual Review of Fluid Mech., Vol. 11, 1979, pp. 95-122.

16. Tollmien, W., "Uber die Entstehung der Turbulenz." 1. Mitteilung, Nachr. Ges Wiss. Gottingen, Math. Phys. Klasse 21-44, 1929 (Also NACA TM 609, 1931).

17. Schlichting, H., "Amplitndenverteilung und Energieb lanz der kleinen Storungen bei der Plattenstromung." Nachr. Ges. Wiss. Gottingen, Math. Phys. Klasse, Fachgruppe I, 1, 47-48, 1935.

18. Schubauer, G. B. and Skramstad, H. K., "Laminar Boundary Layer Oscillations and Stability of Laminar Flow," NBS Research Paper 1772 (originally NACA, April 1943, confidential) also JAS, Vol. 14, pp. 69-78, 1947 and NACA Report 909.

19. Schlichting, H., Boundary Layer Theory, Sixth Edition, McGraw-Hill, 1968.

20. Wortmann, F. X., "The Incompressible Fluid Motion Downstream of Two Dimensional Tollmien-Schlichting Waves," AGARD/NATO CP224 on Laminar-Turbulent Transition, May 1977.

21. Hinze, J.O., Turbulence, Second Edition, McGraw-Hill, 1975.

22. Van Muiswinkel, J.C., Unpublished results, Fluid Mechanics Laboratory, Delft University, 1970 (quoted in Reference 6).

23. Francis, M.S., Keese, J.E., Lang, J.D., Sparks, G.W., Jr., and Sisson, G.E., "Aerodynamic Characteristics of an Unsteady Separated Flow", AIAA Journal, Vol. 17, No. 12, Dec. 1979, pp. 1332-1339.

24. Francis, M.S., Lang, J.D., and Keese, J. E., "Water Tunnel Measurements of Unsteady Separation", A.F.S.C. Report SRL-TR-78-0011, Dec. 1978.

25. Viets, H., Piatt, M. and Ball, M., "Forced Vortices Near a Wall", AIAA paper 81-0256, AIAA 19th Aerospace Science Meeting, St. Louis, Jan. 1981.

26. Viets, H., Piatt, M. and Ball, M. "Unsteady Wing Boundary Layer Energization," AIAA paper 79-1631, Atmospheric Flight Mechanics Conf., Boulder, Colo., Aug. 1979.

27. Viets, H., Piatt, M. and Ball, M., "Boundary Layer Control by Unsteady Vortex Generation," Journal of Wind Eng. and Ind. Aero., Vol. 7, 1981, pp. 135-144.

28. Viets, H. and Piatt, M., "Induced Unsteady Flow in a Dump Combustor," in Combustion in Reactive Systems (Bowen, Manson, Oppenheim and Soloukhin, eds). Vol. 76 of Progress in Astro. and Aero., 1981.

29. Viets, H., "Coherent Structures in Time Dependent Flow," Proceedings of the NATO/AGARD Specialists Meeting on Turbulent Boundary Layers, The Hague, Netherlands, CP-271, Sept. 1979.

30. Viets, H., Catalano, G. and Ball, M., "Vortex Production Near the Back of an Automobile or Van", in preparation.
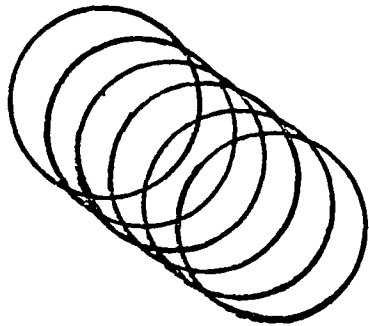
Figure 1. Stability of an infinite set of vortex rings.
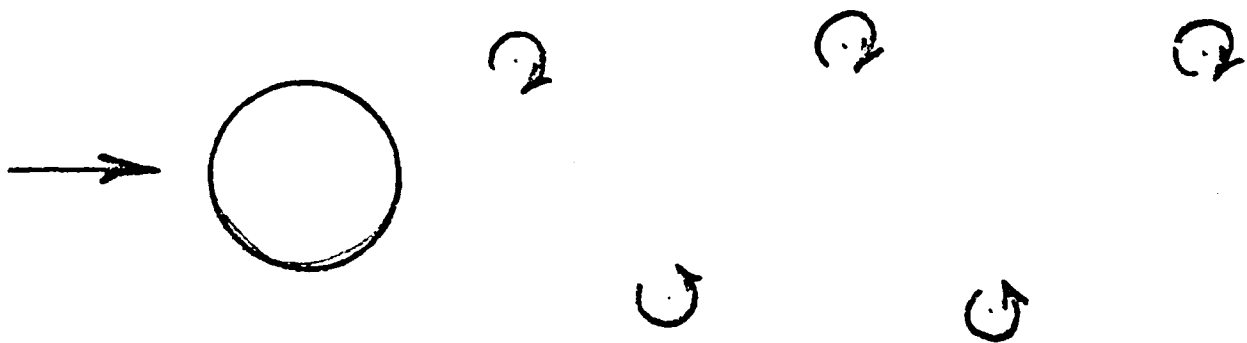
Figure 2. Karman Vortex Street[5]
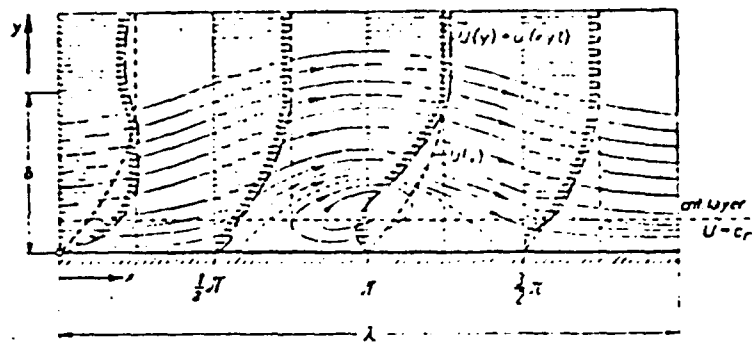
Figure 3. Streamline pattern associated with a
neutral disturbance. Calculations by
Schlichting.[19]
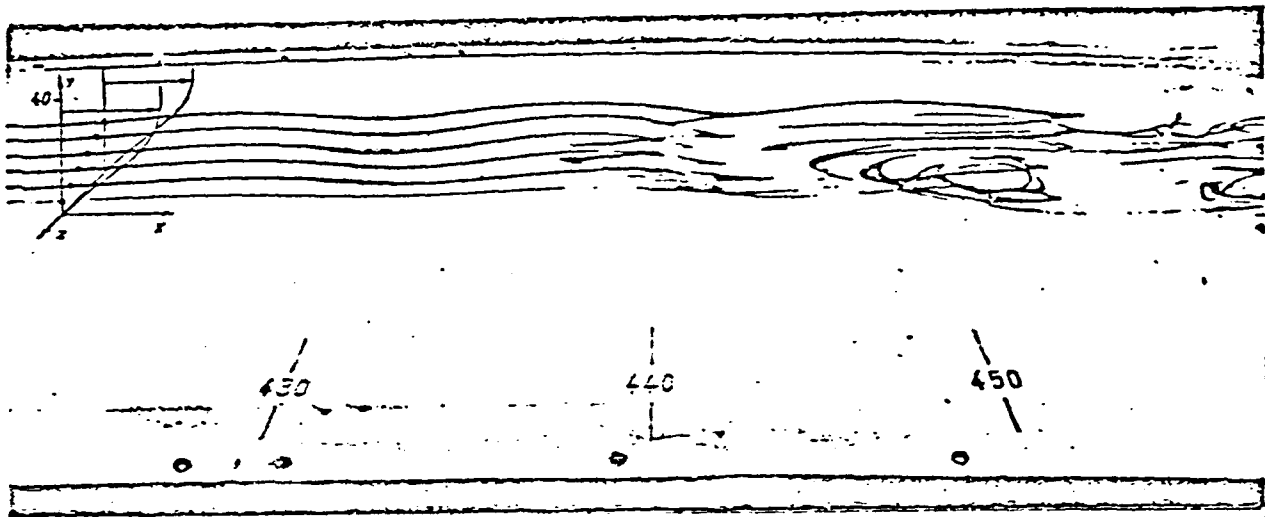
Figure 4. Dye streaklines illustrating Tollmien-Schlichting
waves (due to Wortmann[20]).
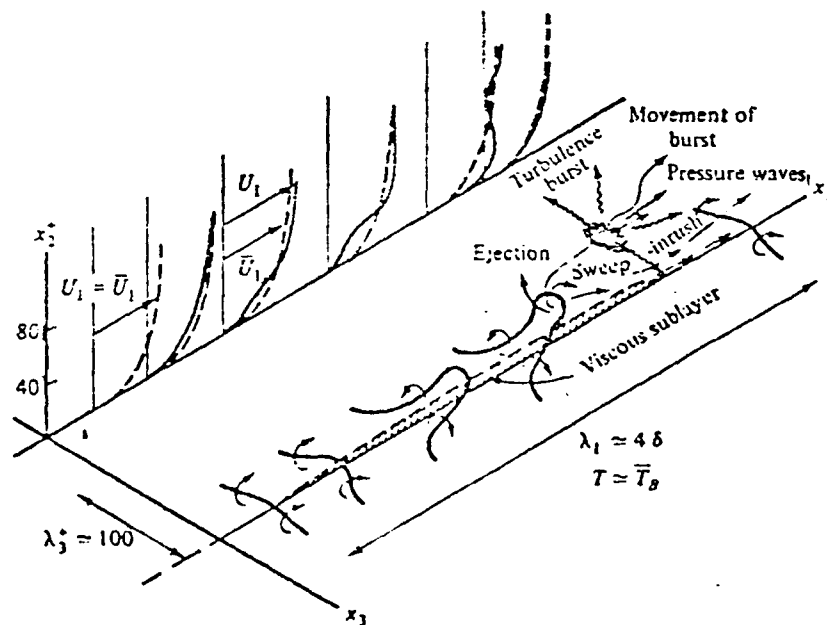
Figure 5. Conceptual model of the vortex dynamics
near a wall, due to Hinze[21].
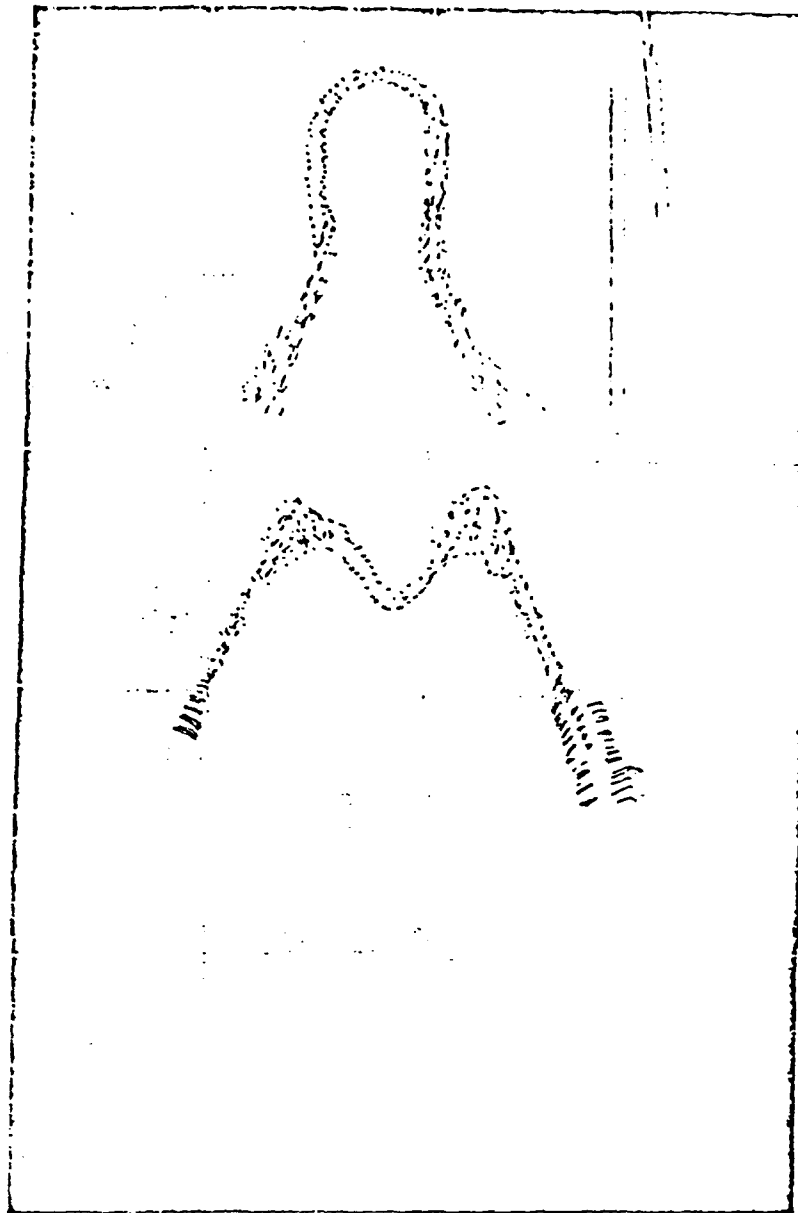
Figure 6 . Deformation of the vortex structure
produced by an oscillating ribbon as
seen from above (due to Wortmann[20]).
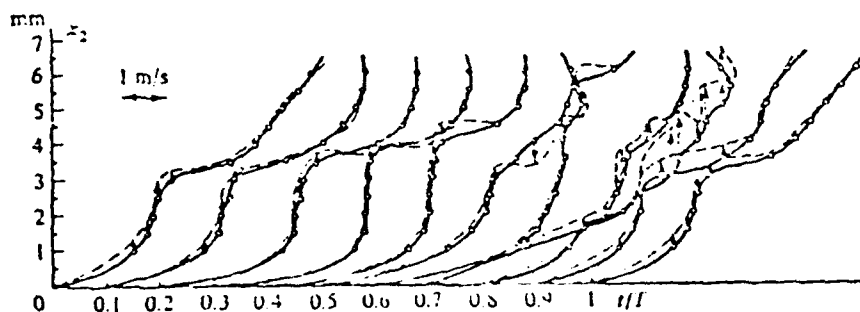
Figure 7. Instantaneous velocity profiles at various times
during one cycle, at one streamwise position,
employing an oscillating ribbon (due to
Nuiswinkel[22].
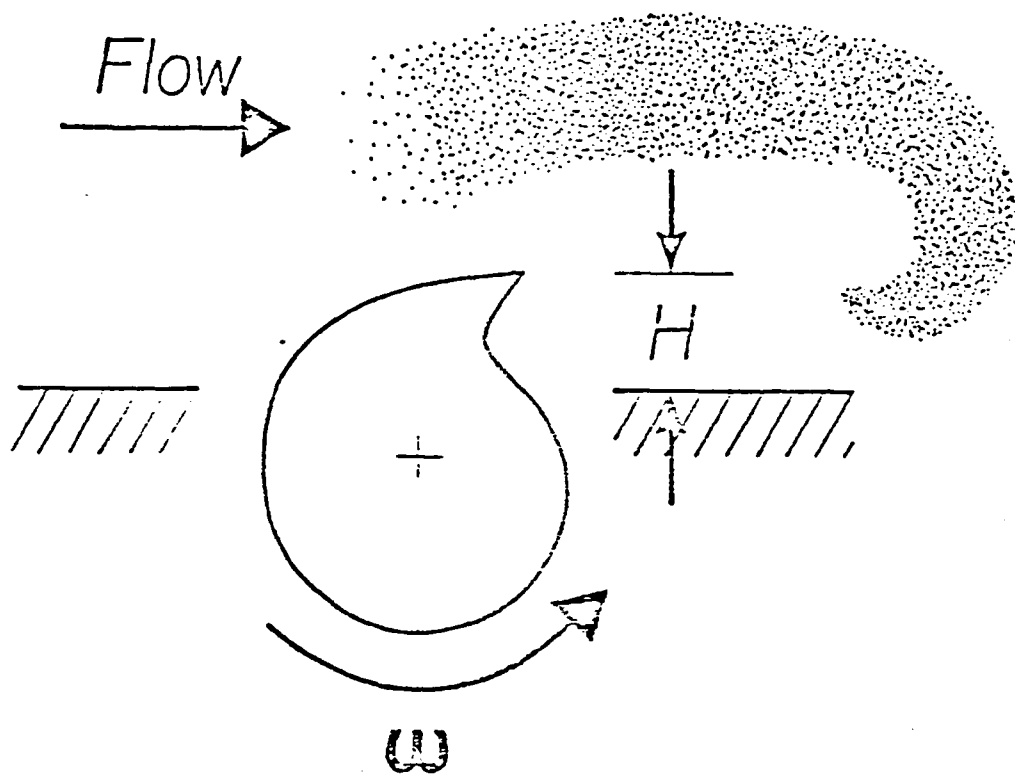
Figure 8. Rotor Geometry Employed for the
Vortex Generation.
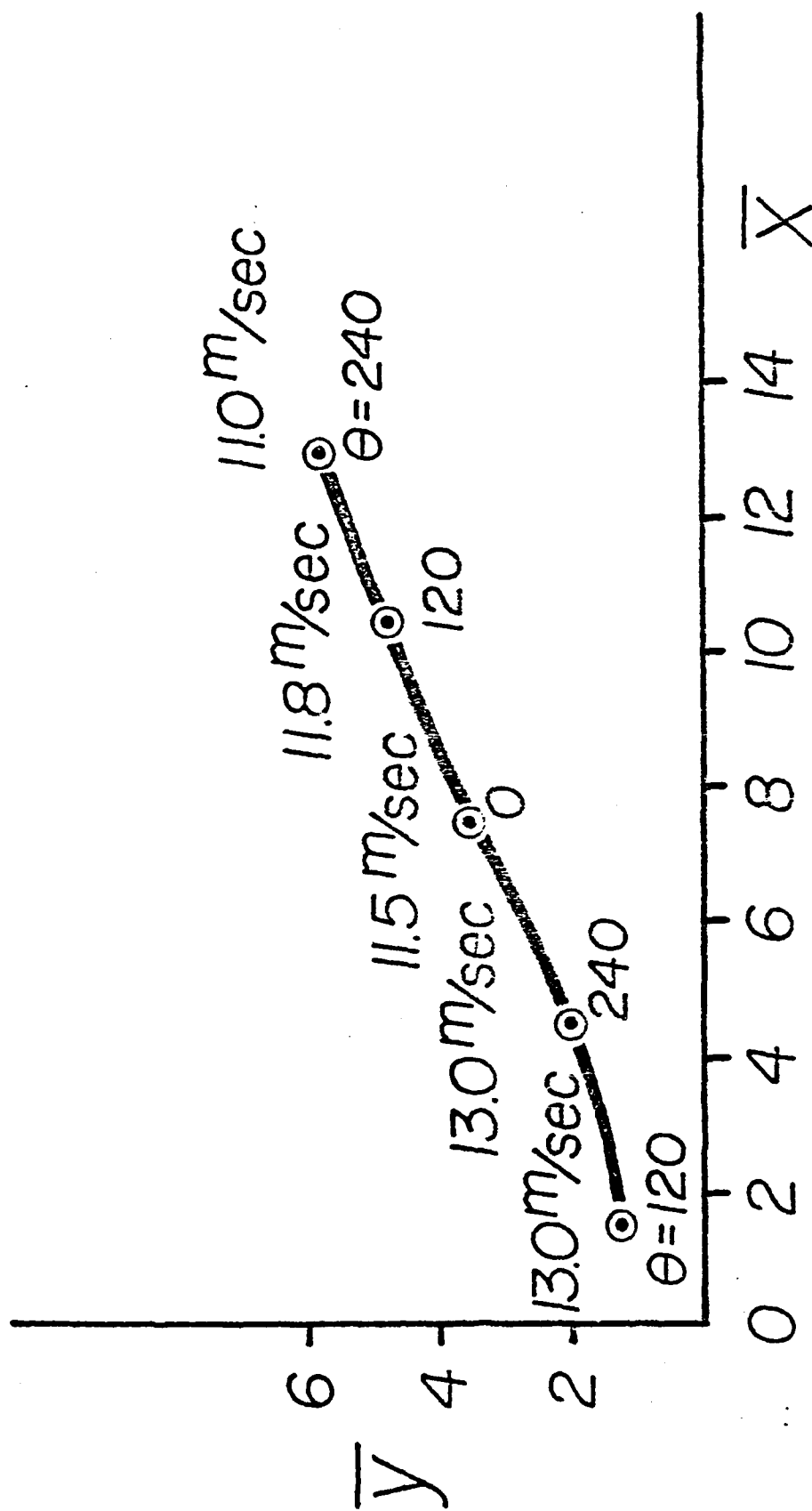
Figure 9. Trajectory of the vortex in the centerline plane, w = 3000 rpm ccw
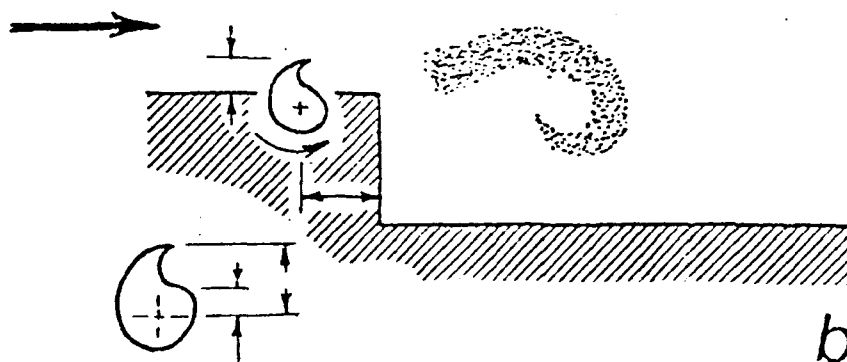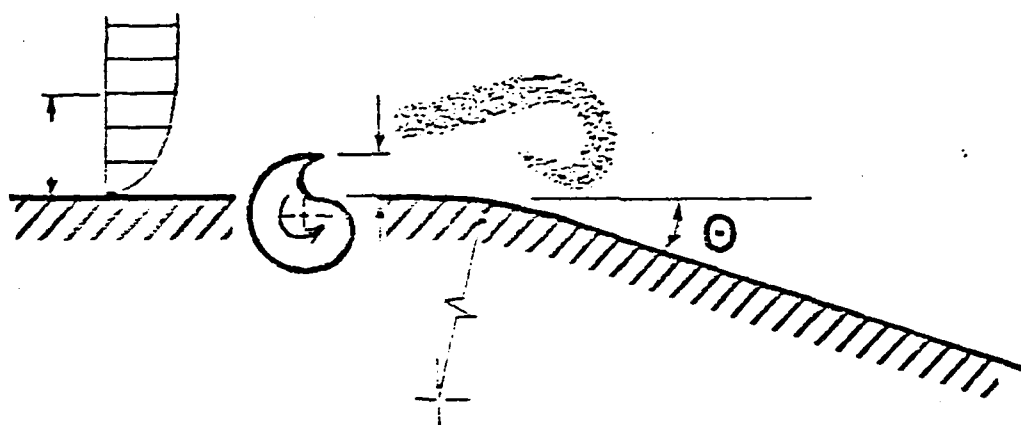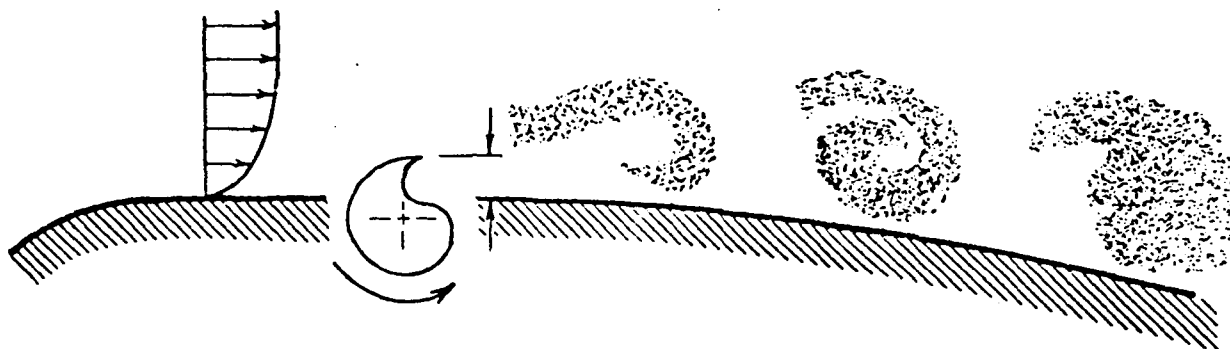
Figure 10. Potential applications of rotor
induced unsteady flows.

Θ = 0°

3000 rpm

Figure 11. Centerline flow visualization results for w = 3000 rpm counterclockwise and phase angle θ = 0°.

$\Theta = 120°$

3000 rpm

Figure 12. Centerline flow visualization results for w = 3000 rpm counterclockwise and phase angle $\theta = 120°$.

$\Theta = 150°$

3000 rpm

Figure 13. Centerline flow visualization results for $w = 3000$ rpm counterclockwise and phase angle $\theta = 150°$.
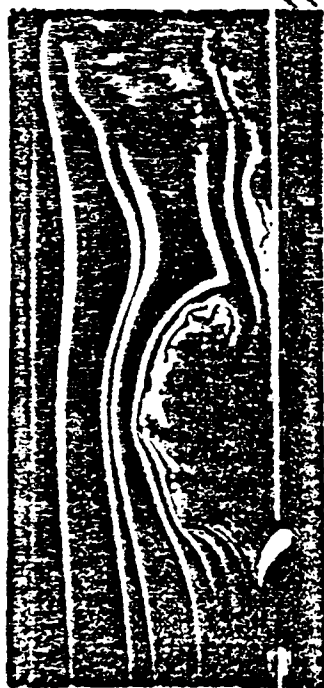
Θ = 240°

3000 rpm

Figure 14. Centerline flow visualization results for w = 3000 rpm counterclockwise and phase angle θ = 240°.
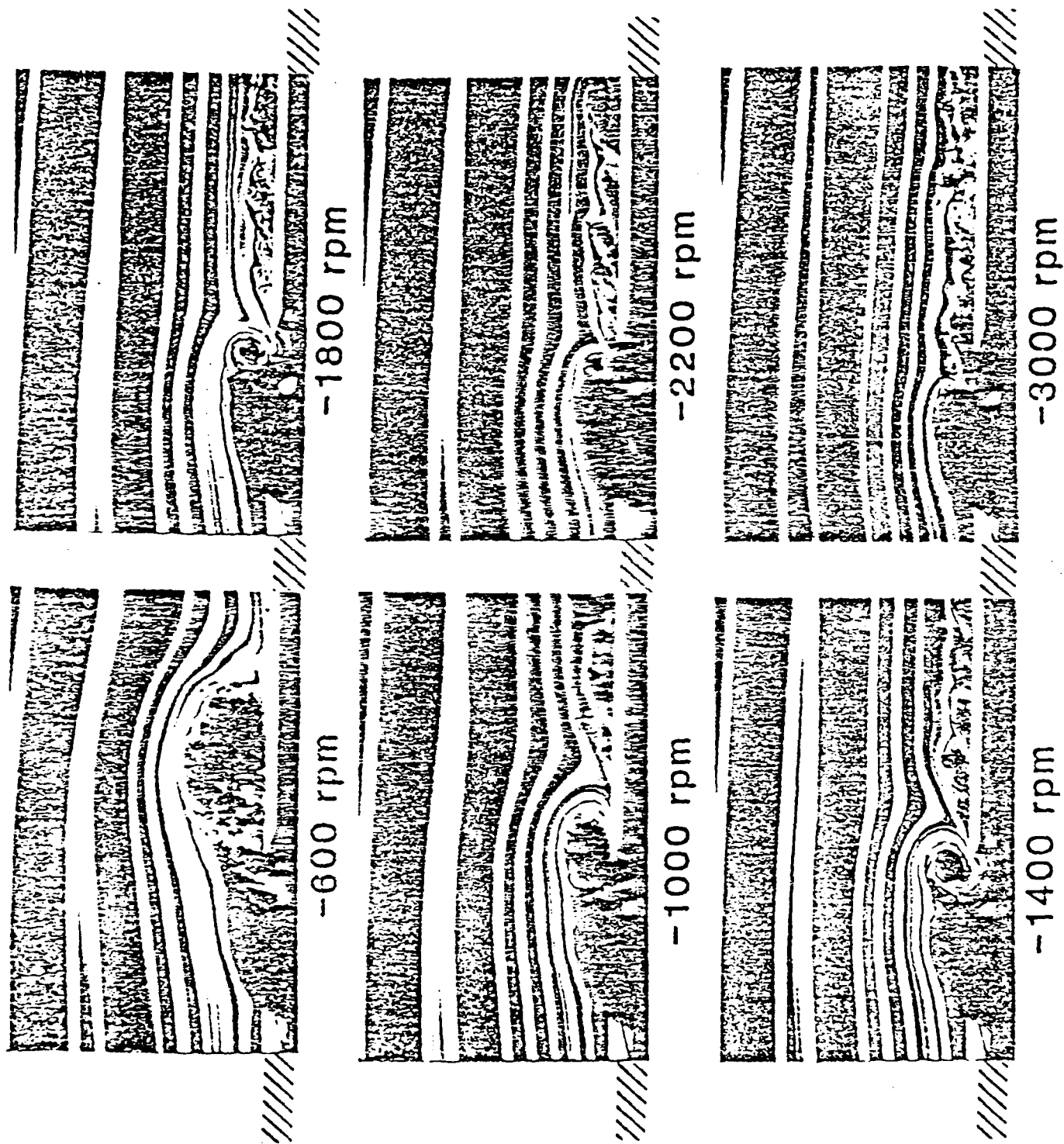
Figure 15. Formation (at θ = 30°) of the vortices formed at various rotor speeds, all in the clockwise direction.

−600 rpm

−1000 rpm

−1400 rpm

−1800 rpm

−2200 rpm

−3000 rpm

Θ = 30°

67.5° 90° 270°

0° 22.5° 45°
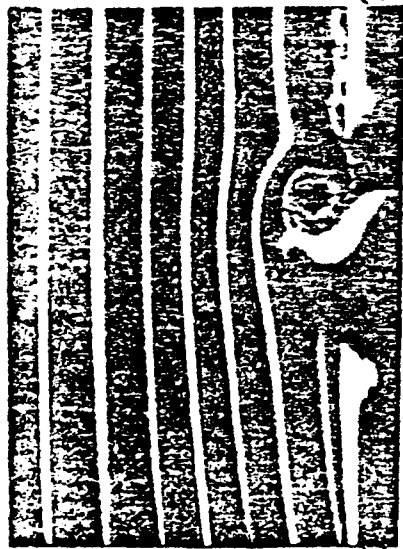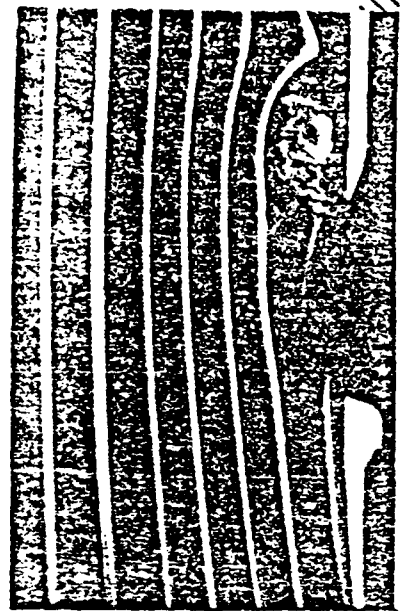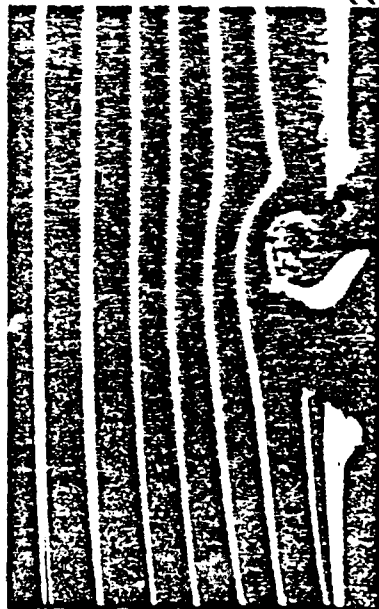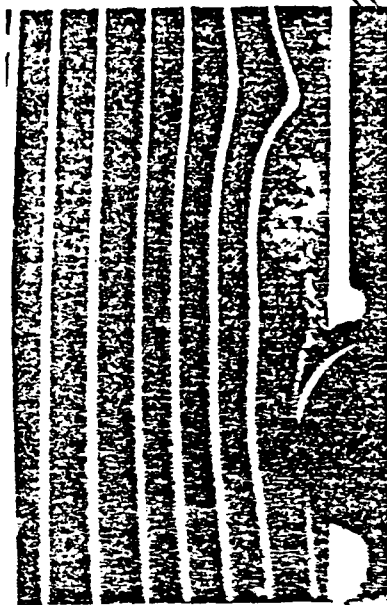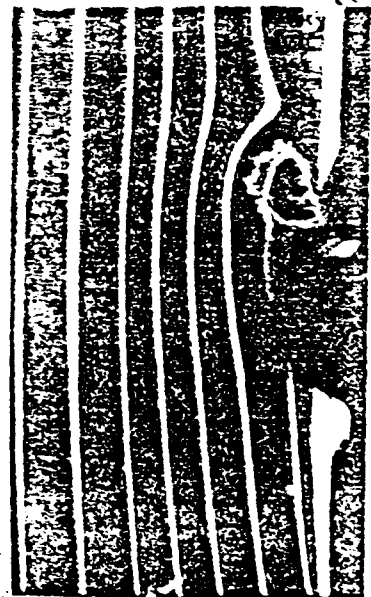
−2000 rpm

Figure 17. DATA STATIONS

FREE STREAM VELOCITY
APPROXIMATELY
70 ft/sec

ROTOR ℄

17⅞"

←2⅝"→

FLOW

PLANE −4 inches

PLANE −2 inches

PLANE ZERO

PLANE +2 inches

PLANE +4 inches

1 2 3 4 5 6 7 8 9 11 12 22

θ = 0°
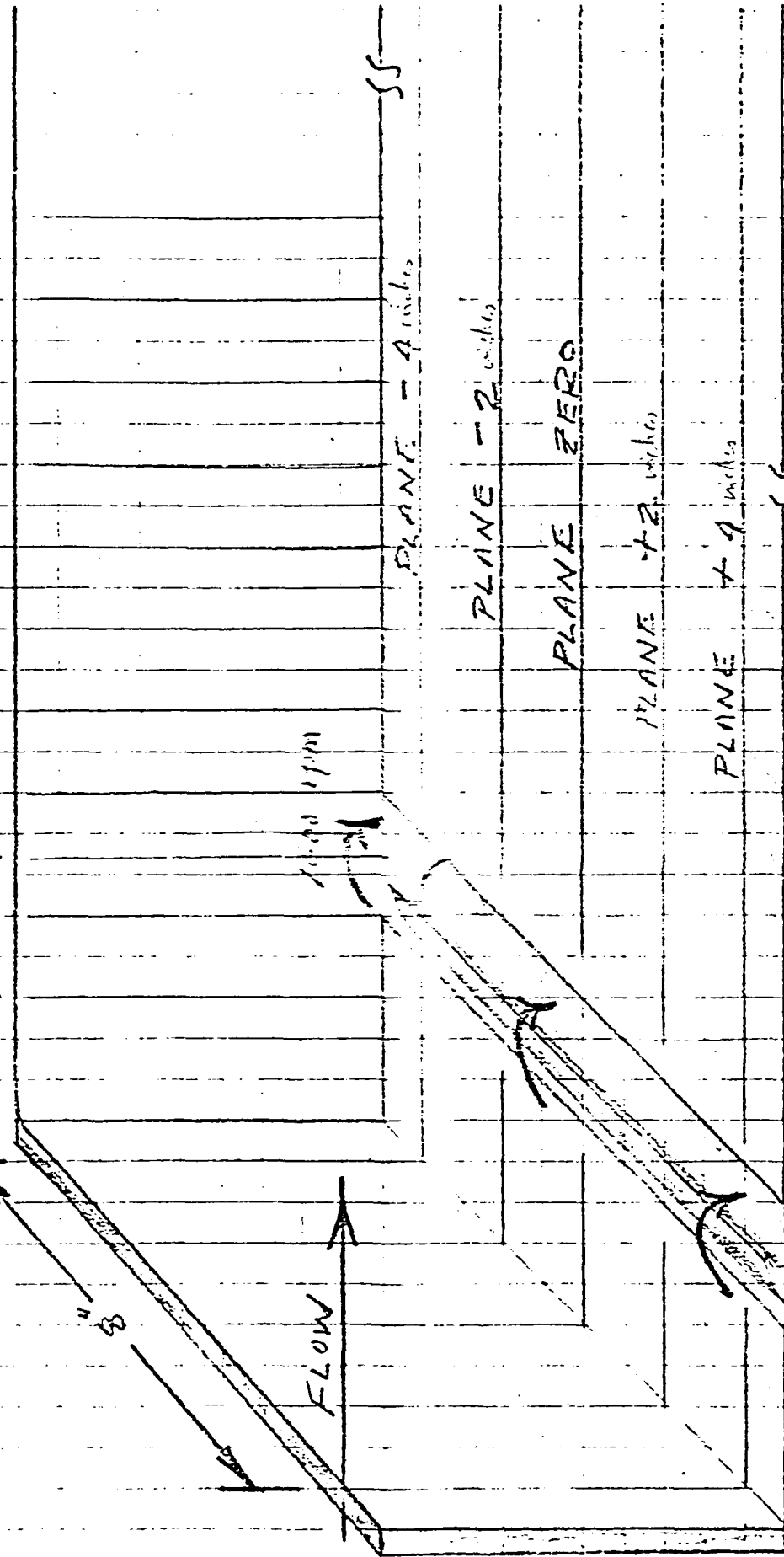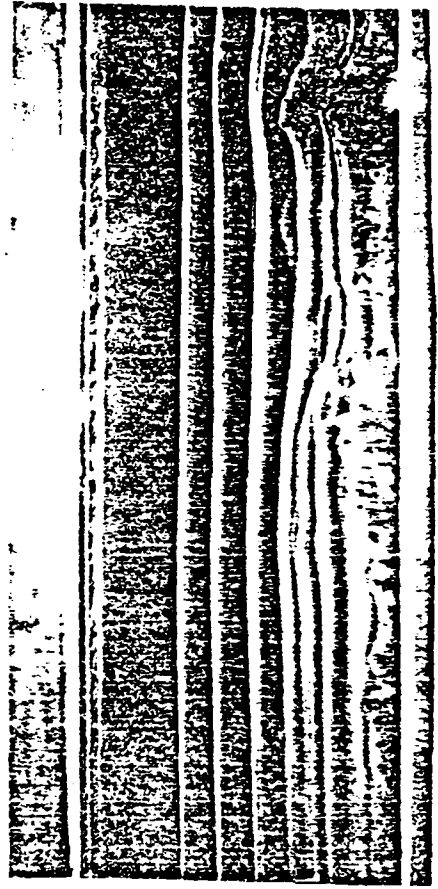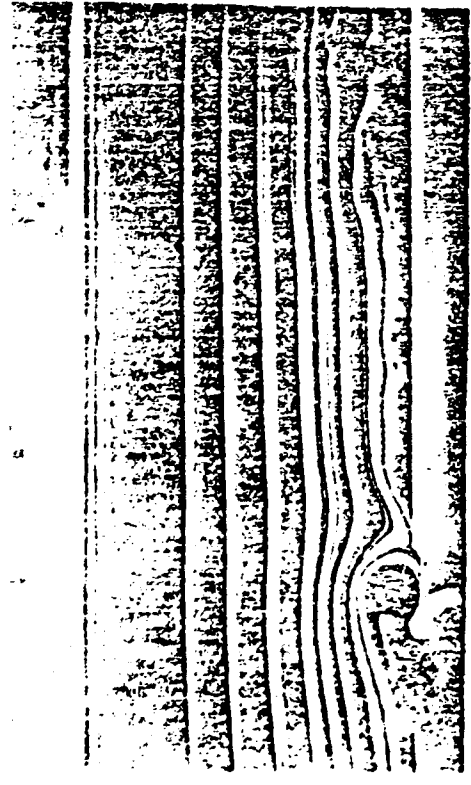
PLANE = -4 INCHES

Figure 18.

PLANE = -2 INCHES

θ = 0°

Figure 19

PLANE = CENTERLINE

= 0°

Figure 20.

PLANE = +2 INCHES

+0°

Figure 21h

= 0°
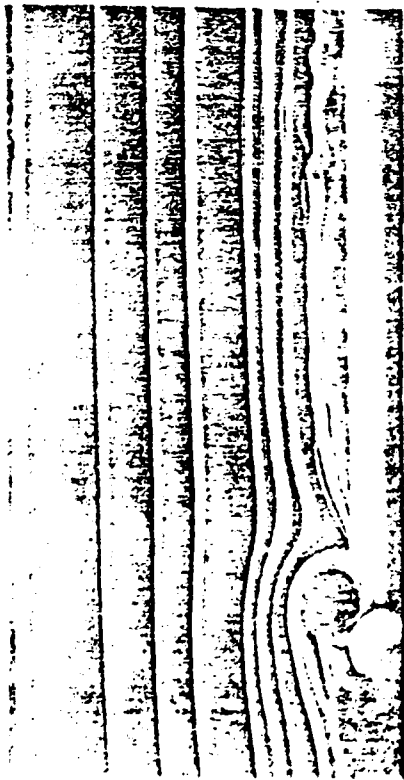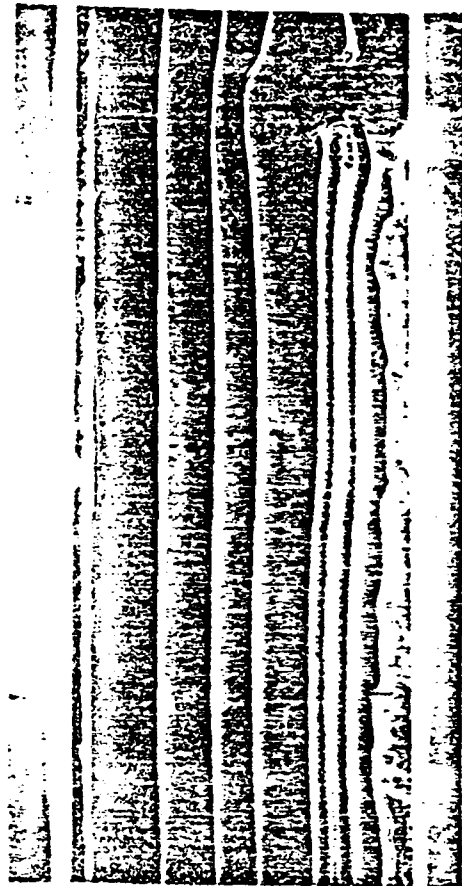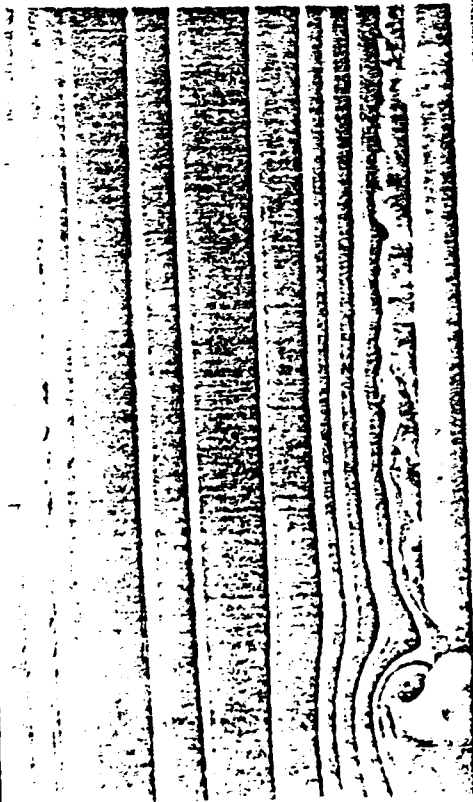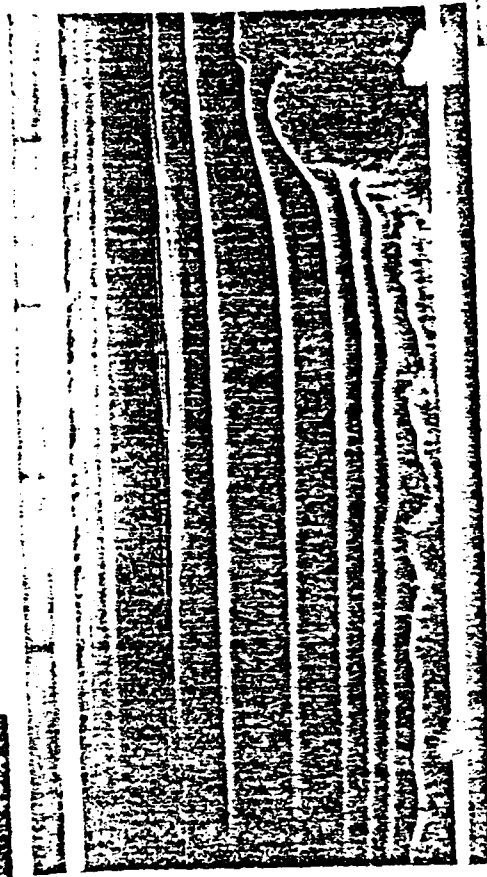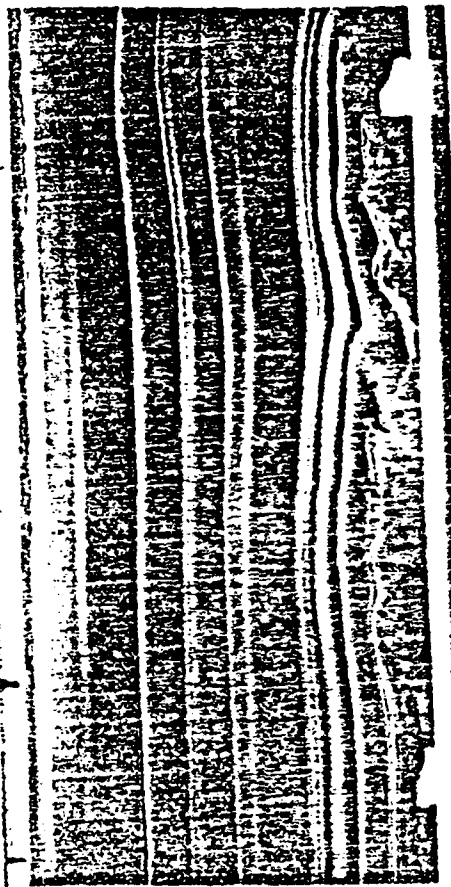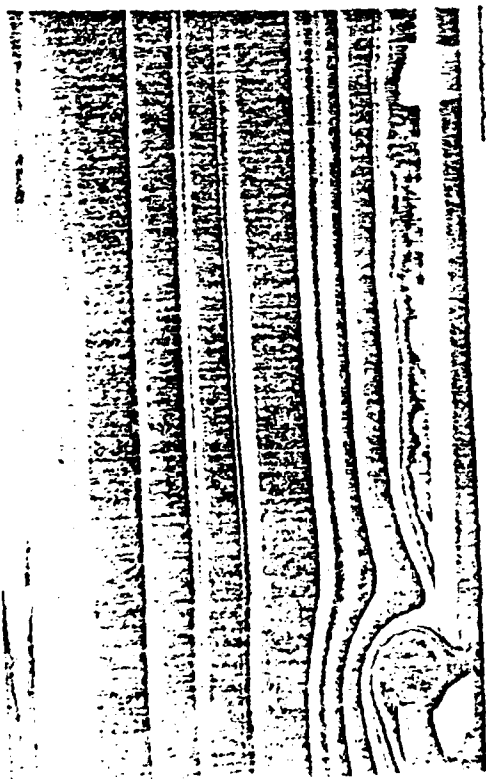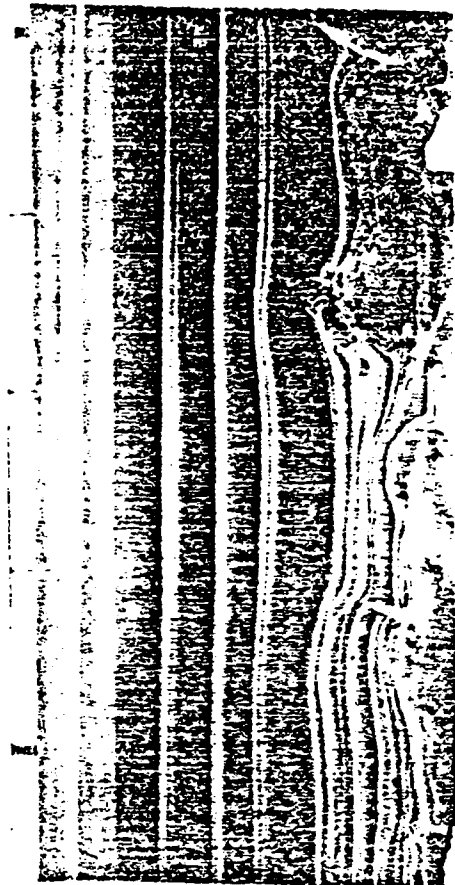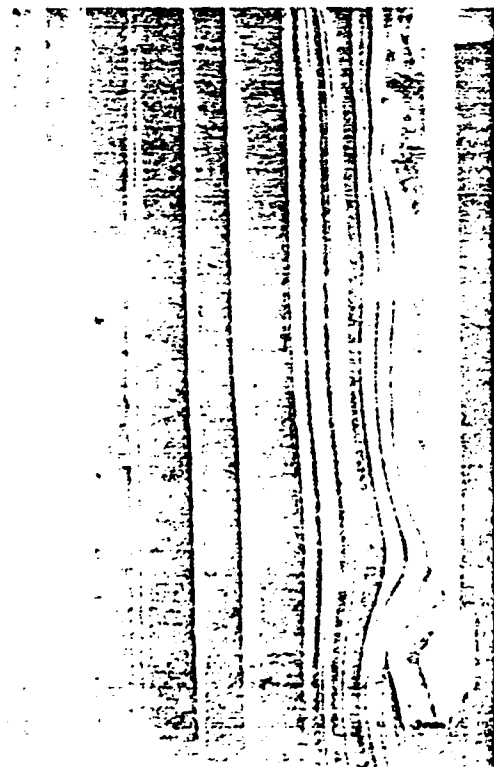
PLANE = +4 INCHES

Figure 22.
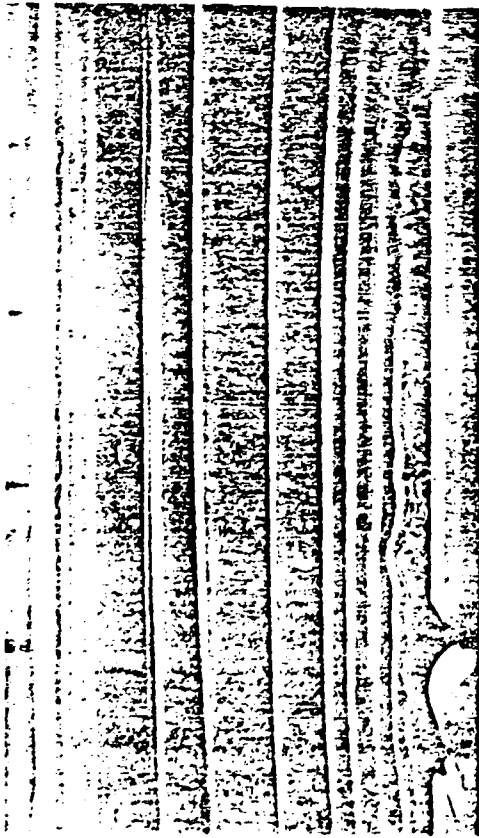
$= 95°$.
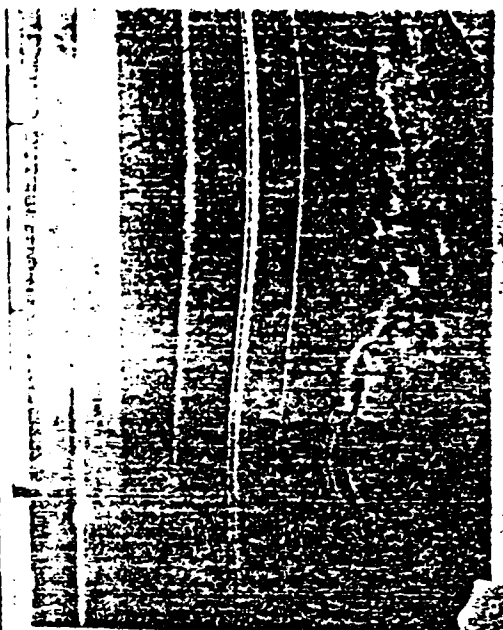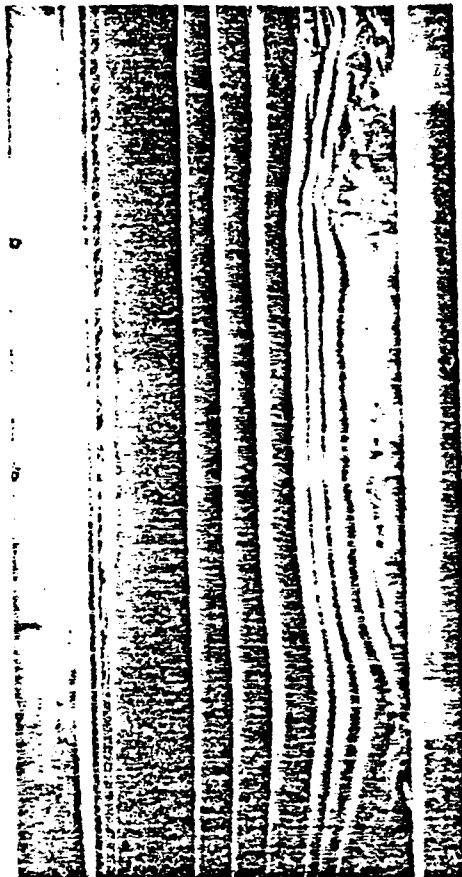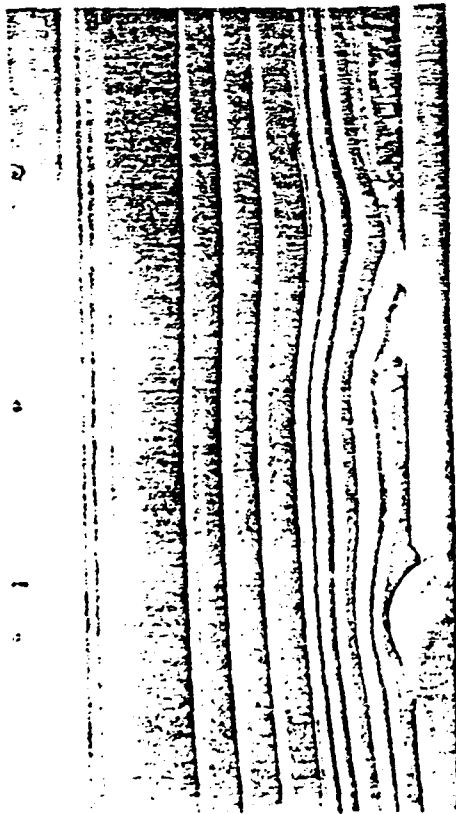
PLANE $= -4$ INCHES

Figure 23.

$\phi = 90°$
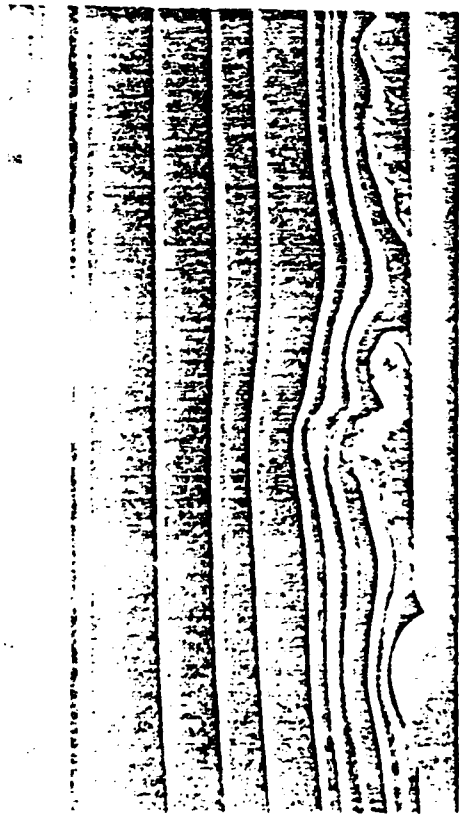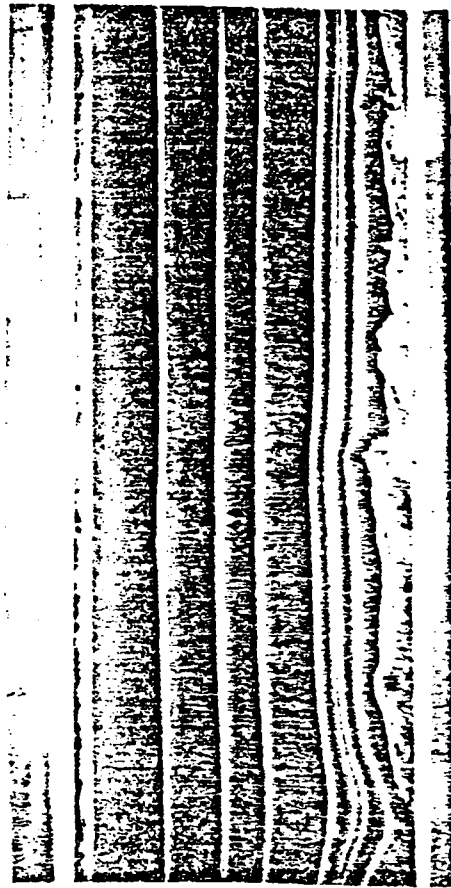
PLANE = -2 INCHES
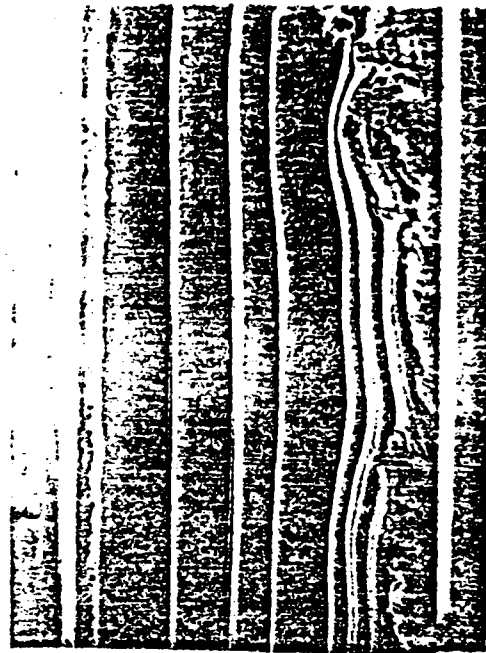
Figure 24.
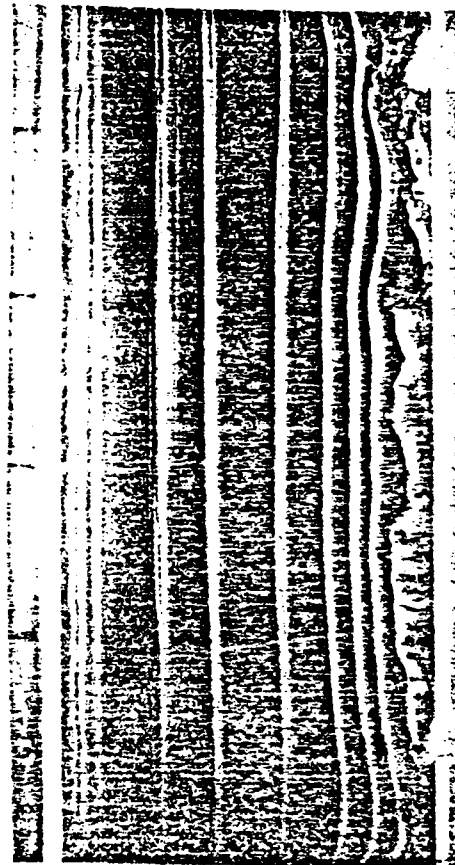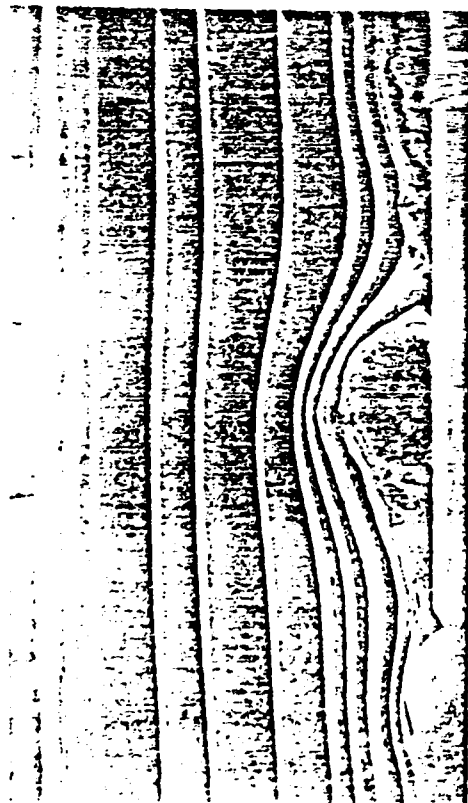
θ = 90°

PLANE = CENTERLINE

Figure 25.

$= 90°$
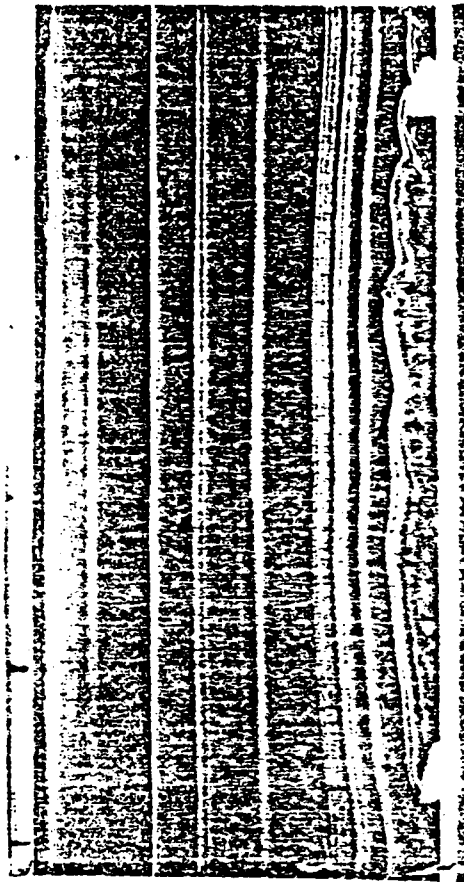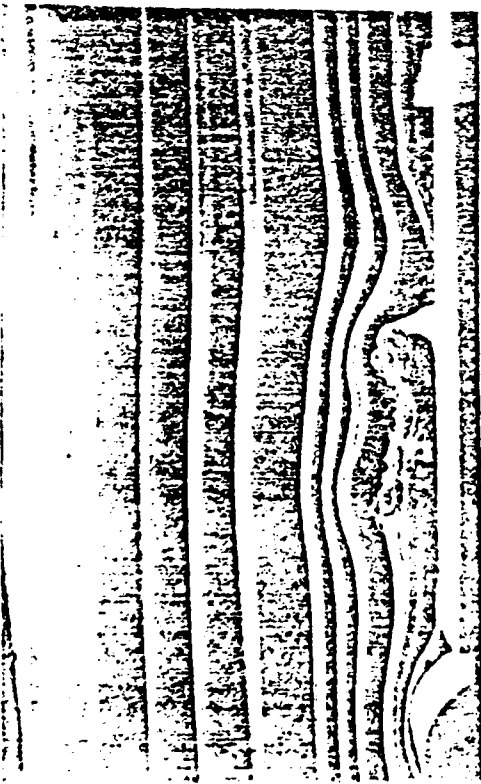
PLANE = +2 INCHES

Figure 26.
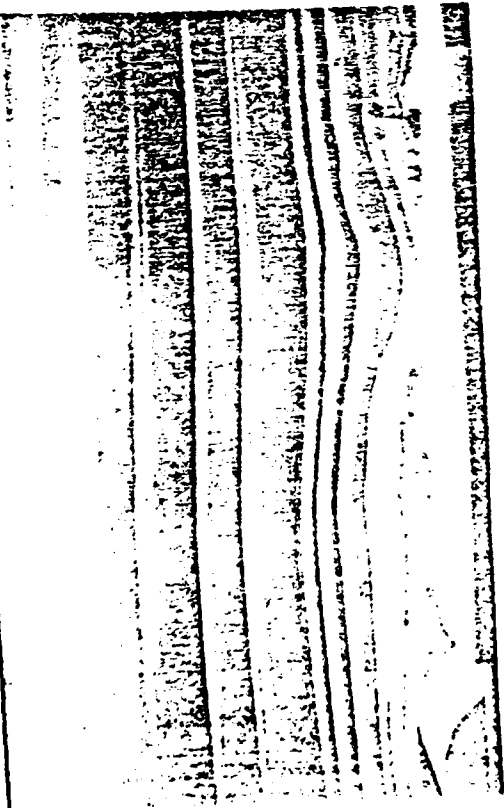
θ = 90°
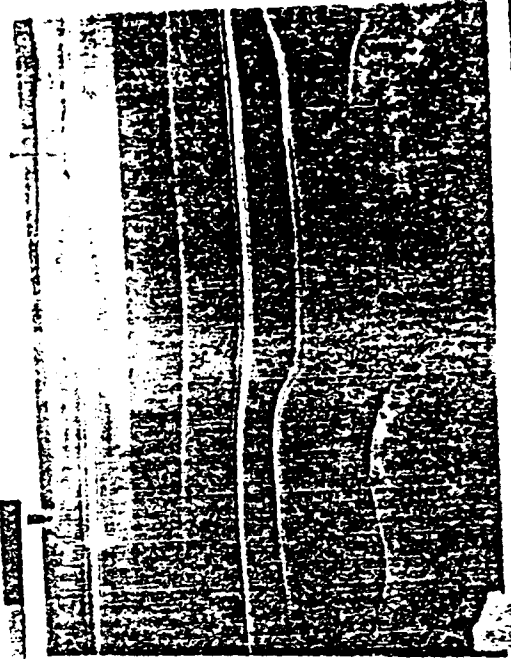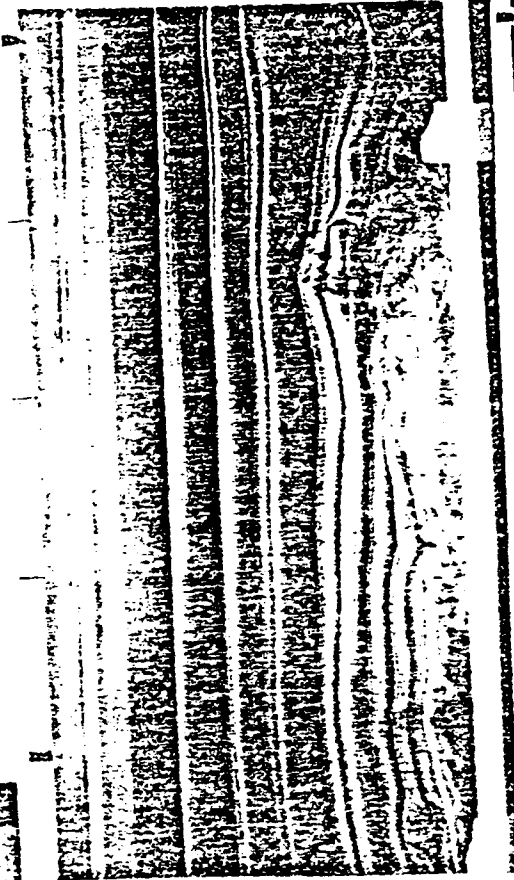
PLANE = +4 INCHES

Figure 27.

$= 120°$
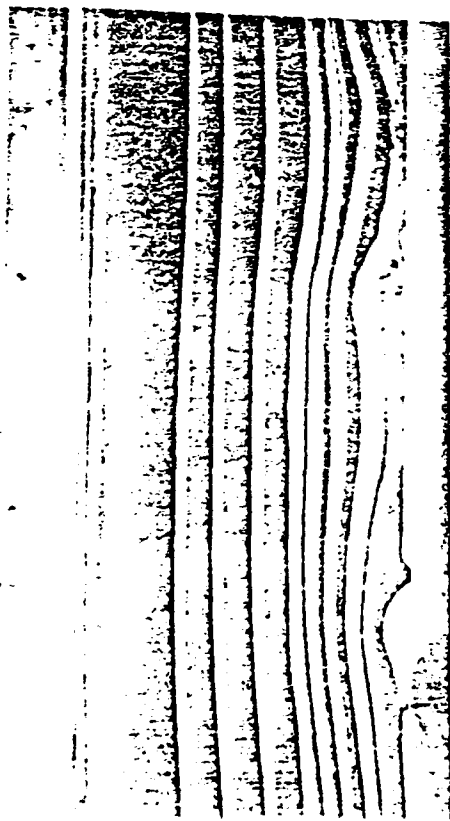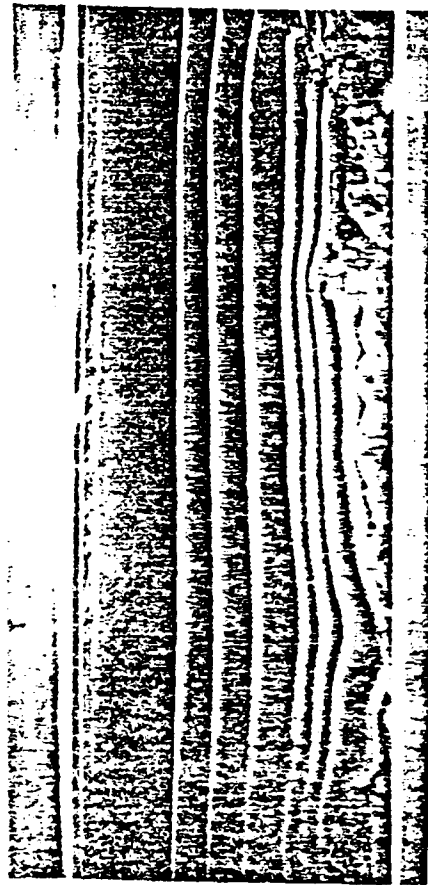
PLANE = -4 INCHES
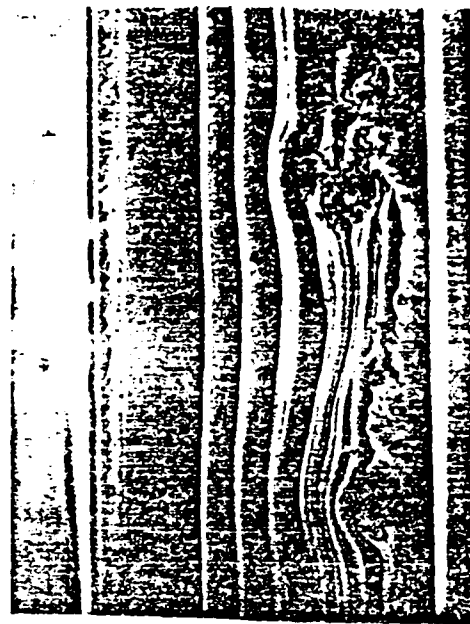
Figure 28.

= 120°
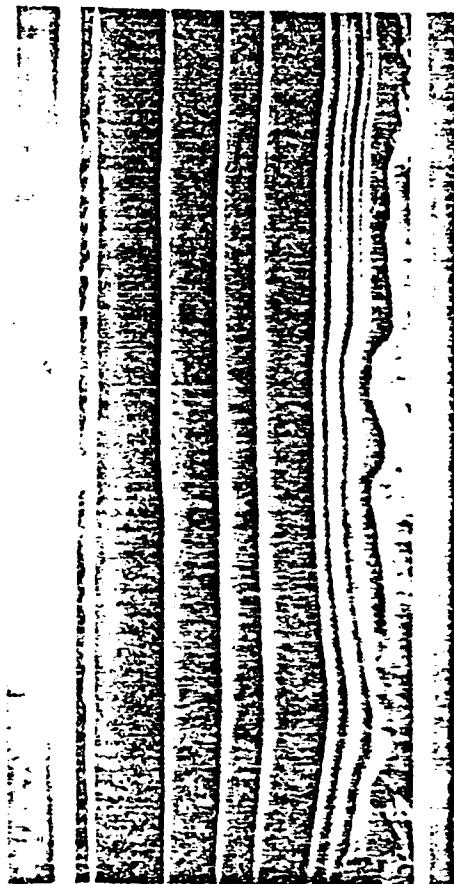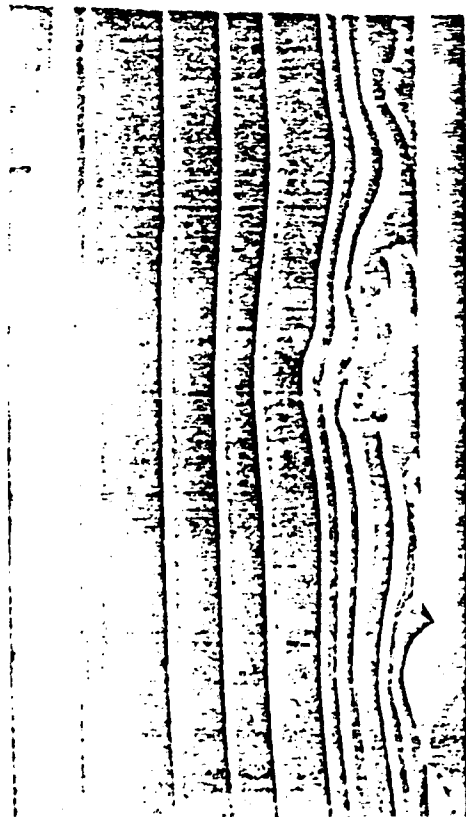
PLANE = -2 INCHES

Figure 29
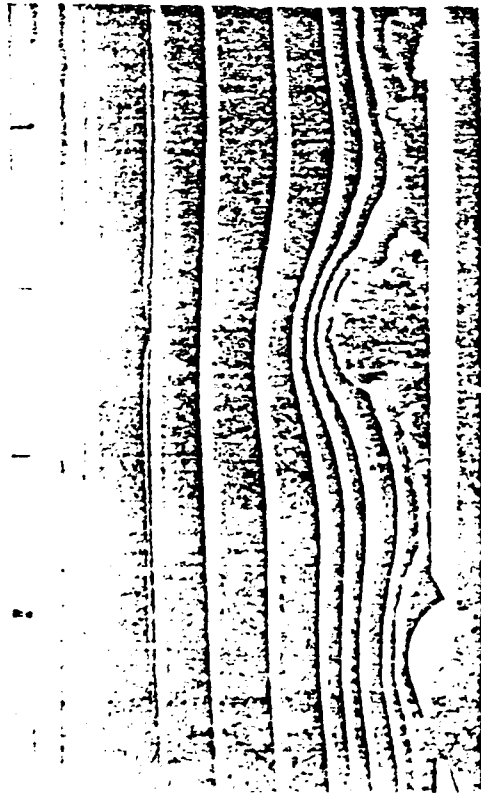
= 120°

PLANE = CENTERLINE
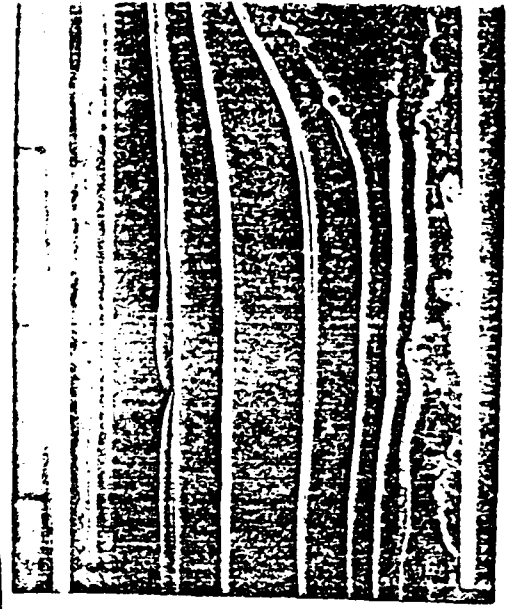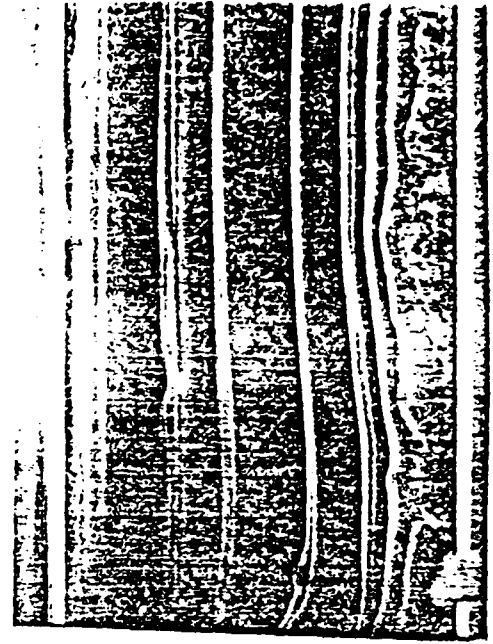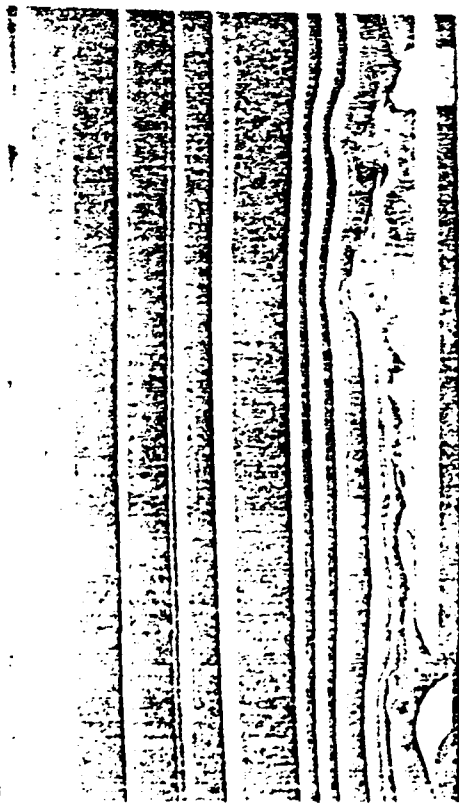
Figure 30.

= 120°
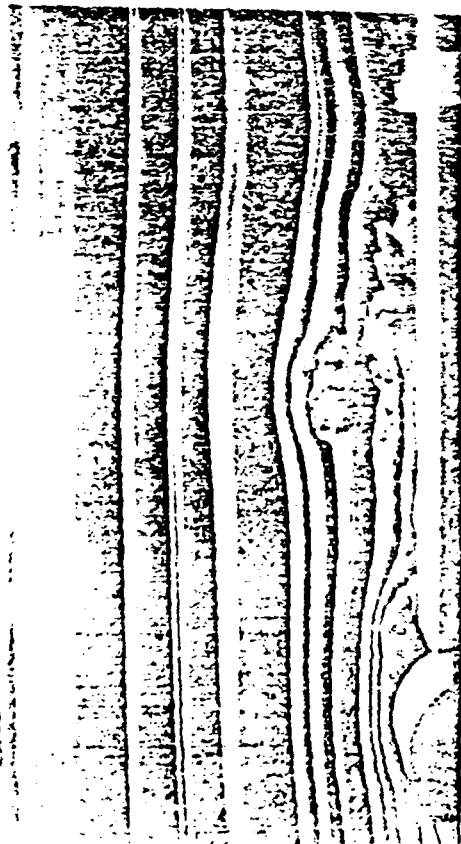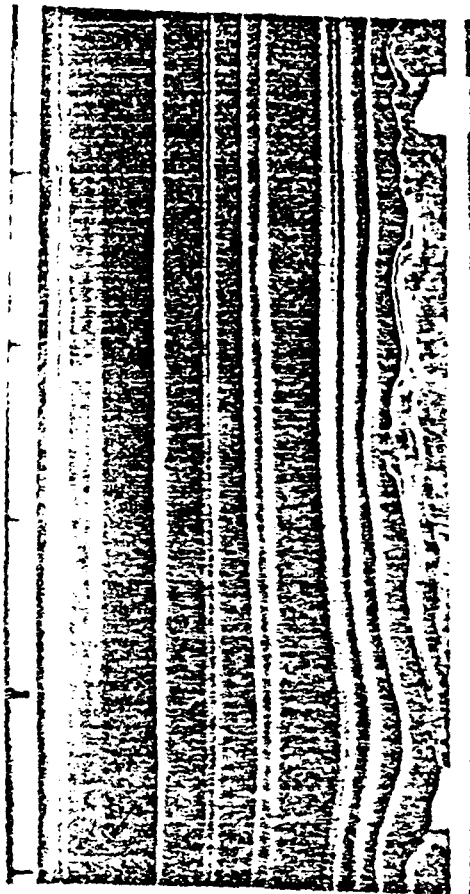
PLANE = +2 INCHES

Figure 31.

= 120°
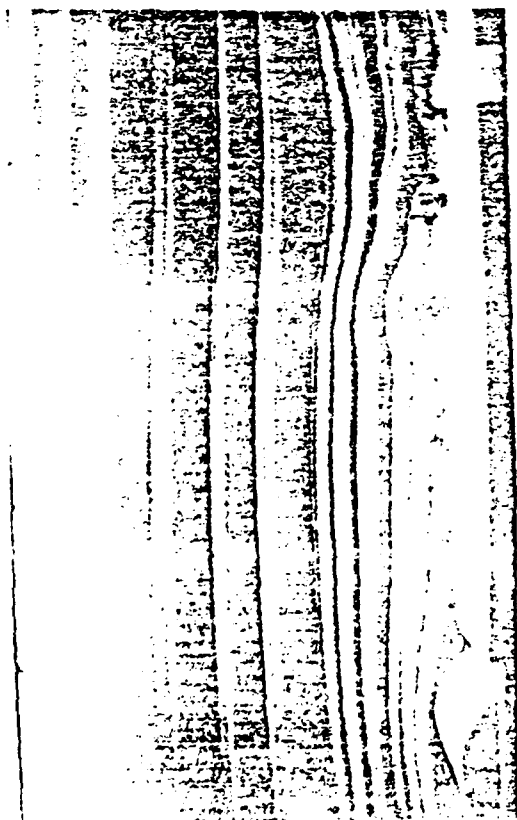
PLANE = +4 INCHES
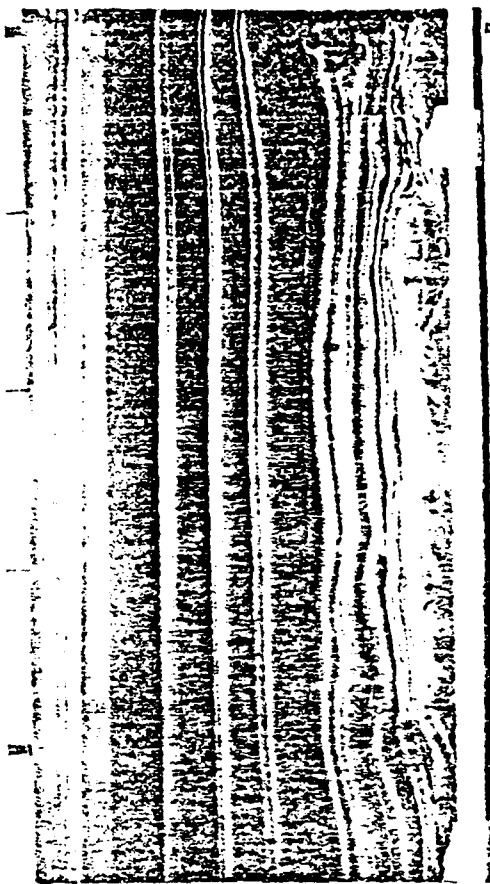
Figure 32.
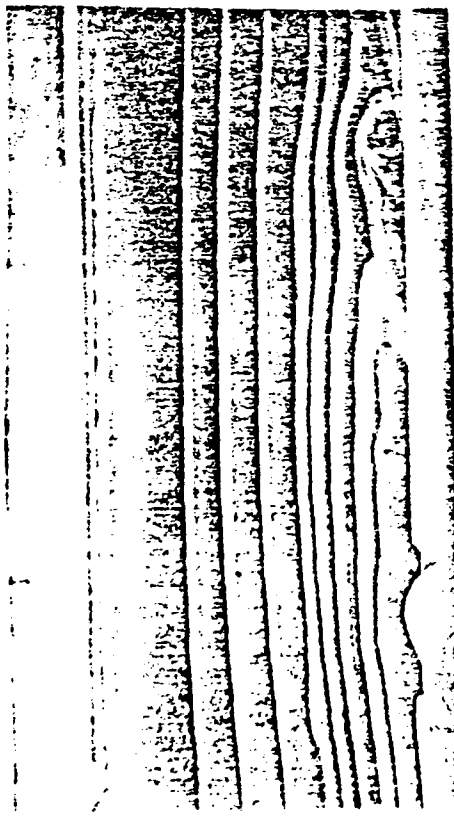
= 180°
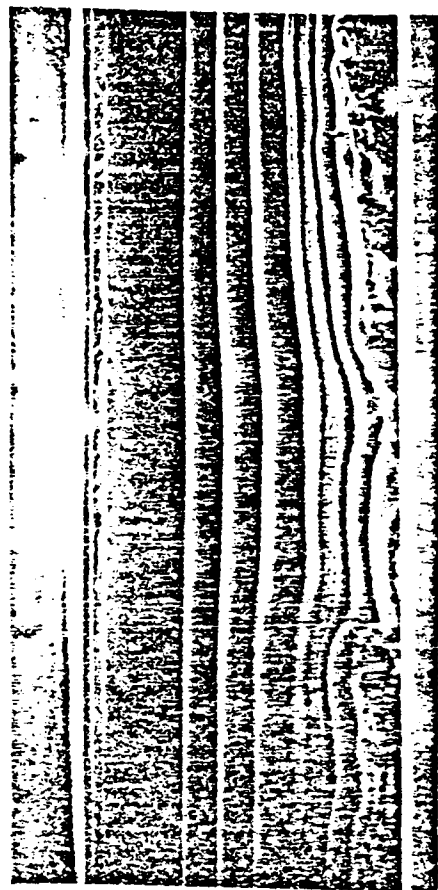
PLANE = -4 INCHES
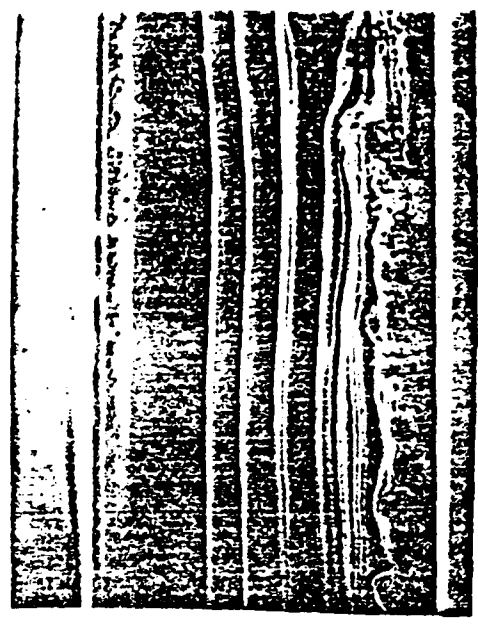
Figure 33.
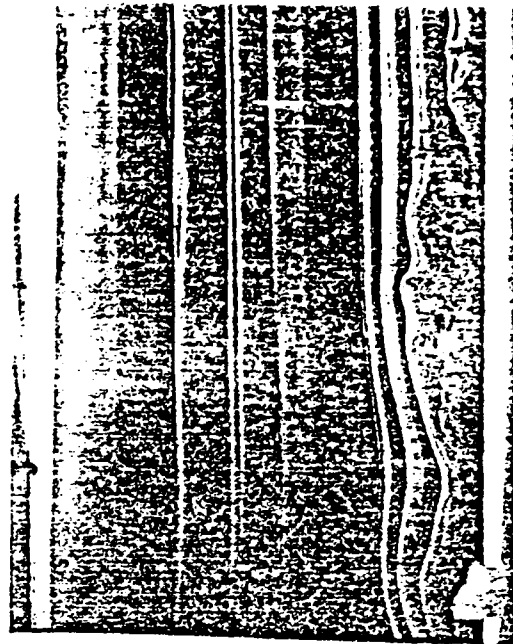
= 180°
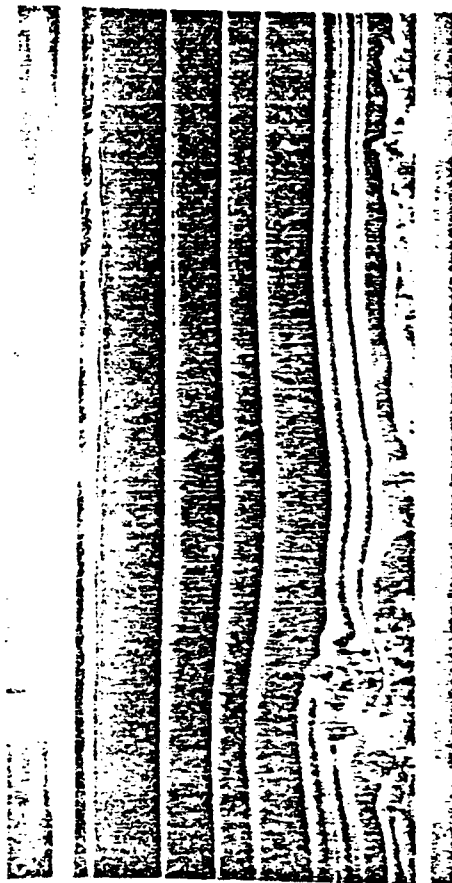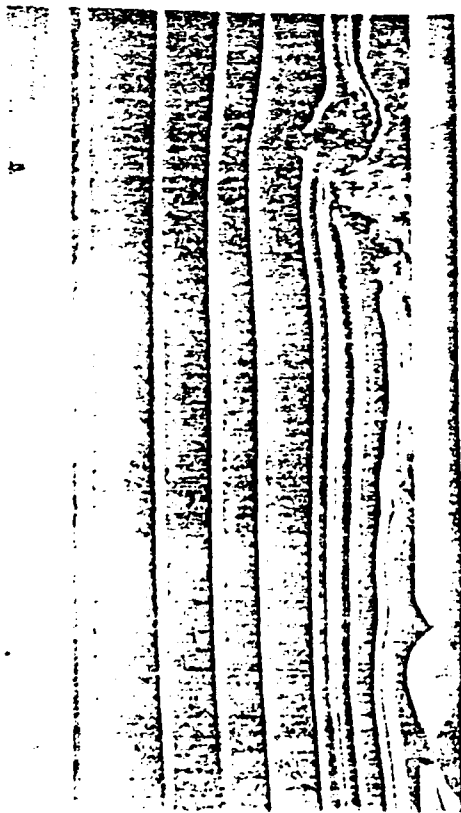
PLANE = -2 INCHES
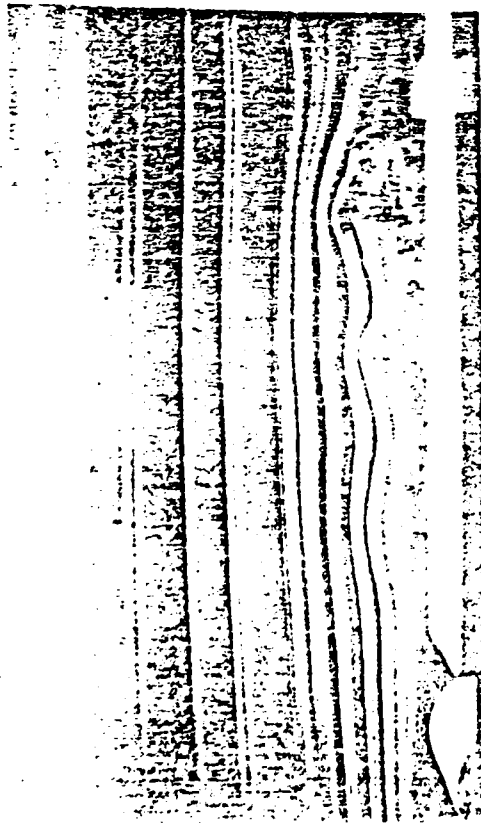
Figure 34.

= 180°
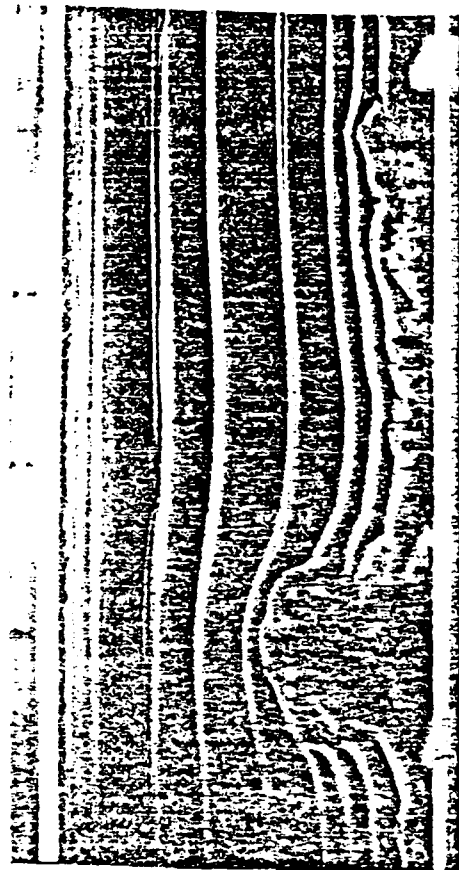
PLANE = CENTERLINE

Figure 35.

= 180°
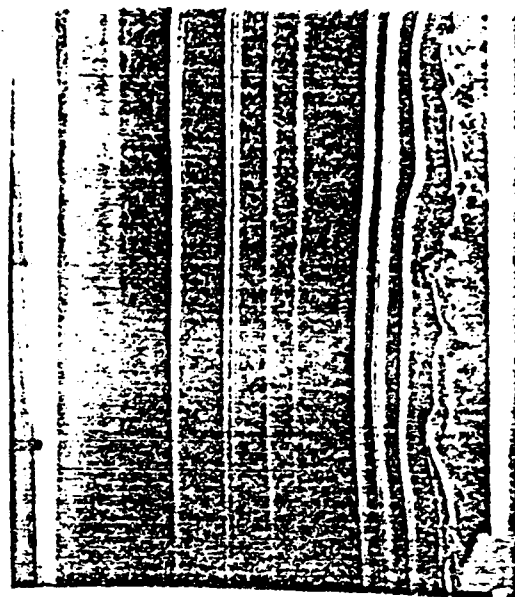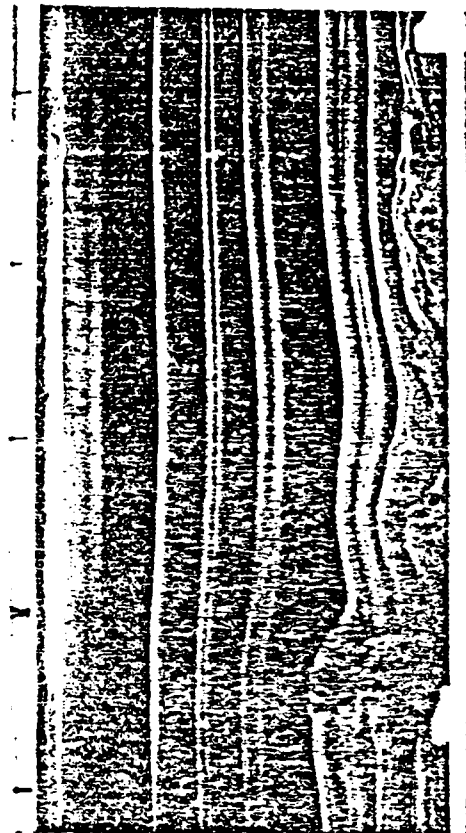
PLANE = +2 INCHES

Figure 36.

PLANE = +4 INCHES

= 180°
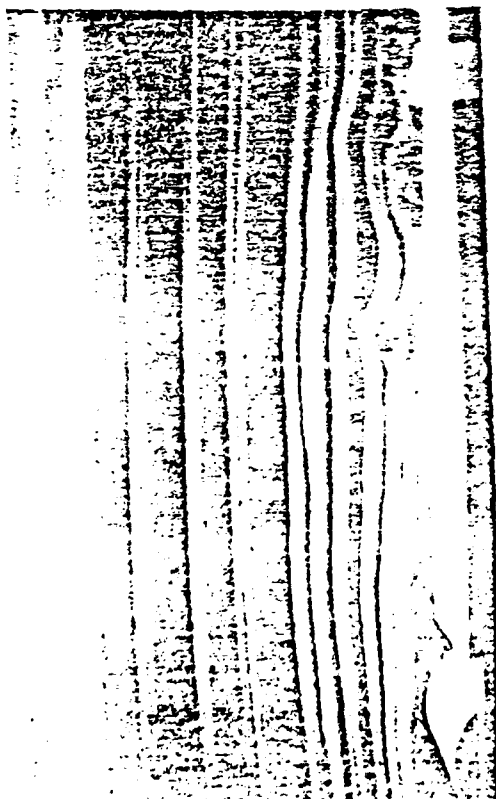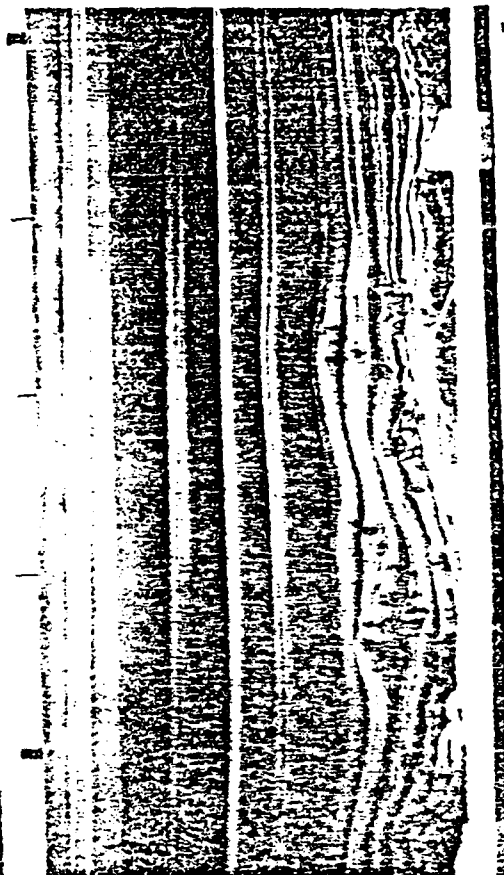
Figure 37.

= 240°
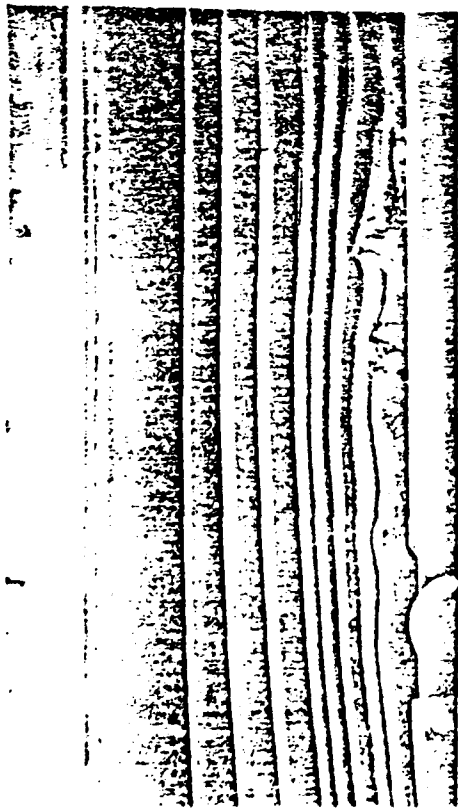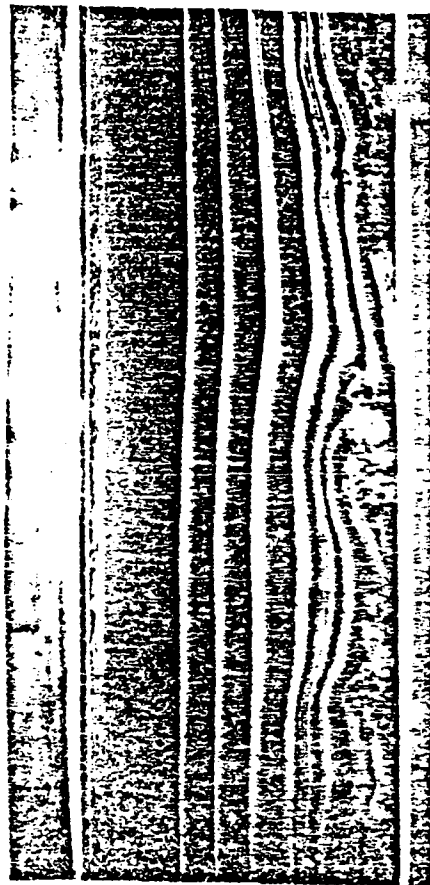
PLANE = -4 INCHES

Figure 38.
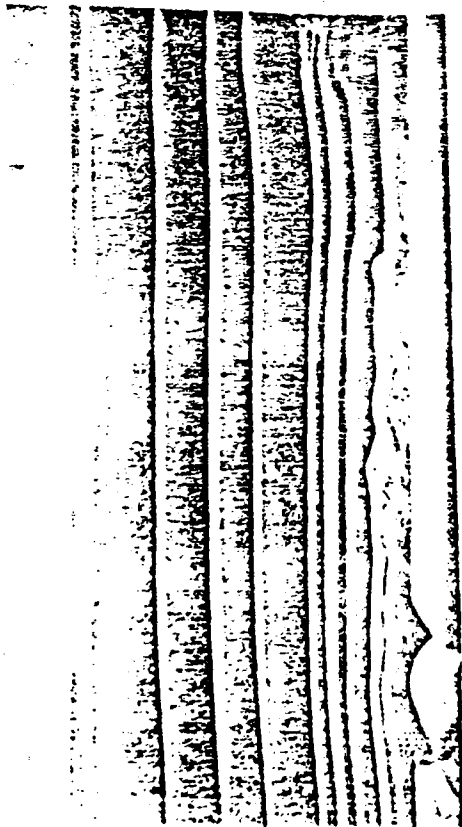
= 240°
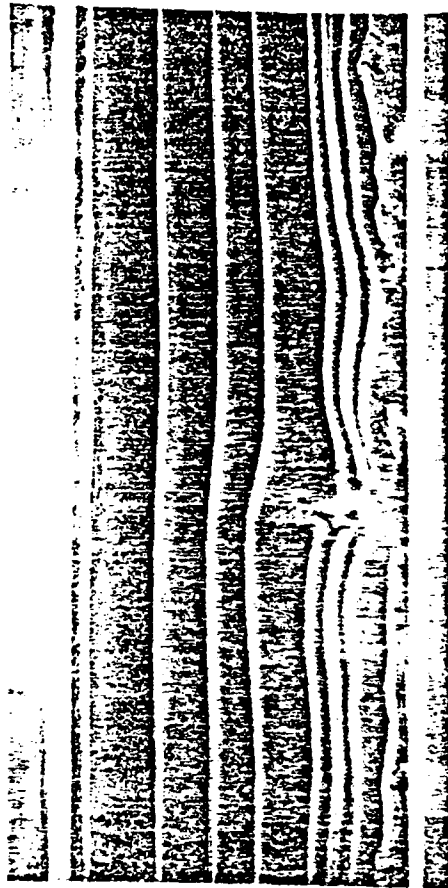
PLANE = -2 INCHES
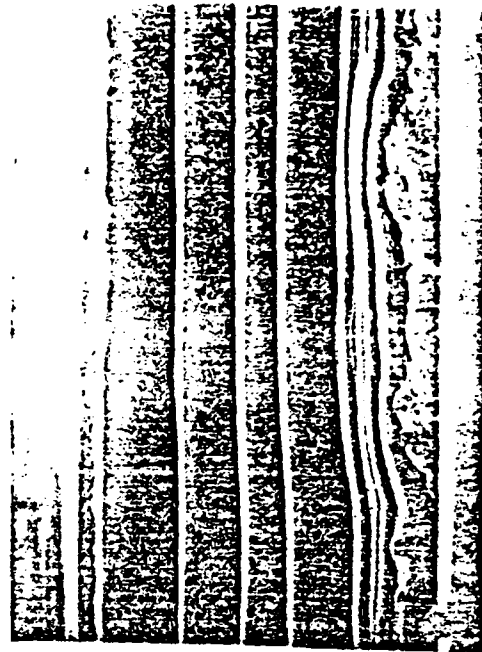
Figure 39.
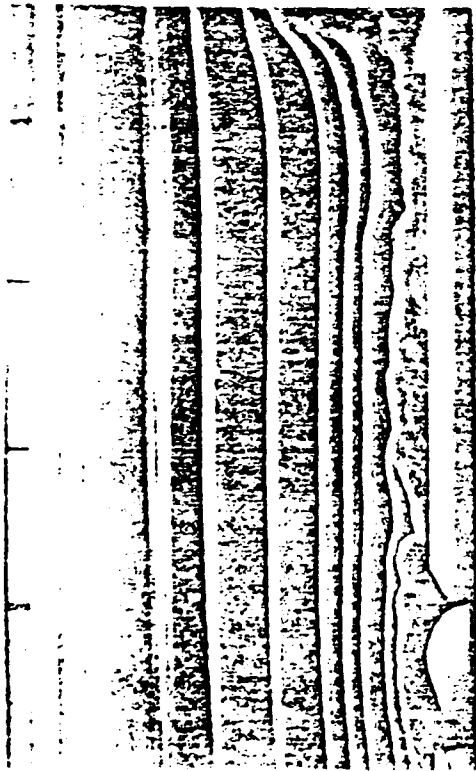
= 240°

PLANE = CENTERLINE

Figure 40.

PLANE = +2 INCHES

= 240°
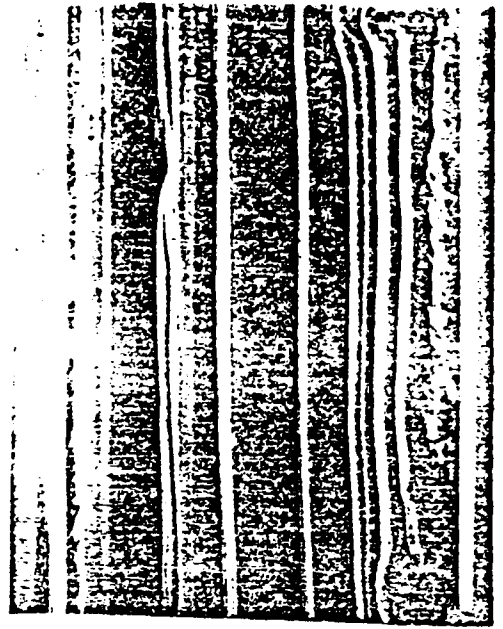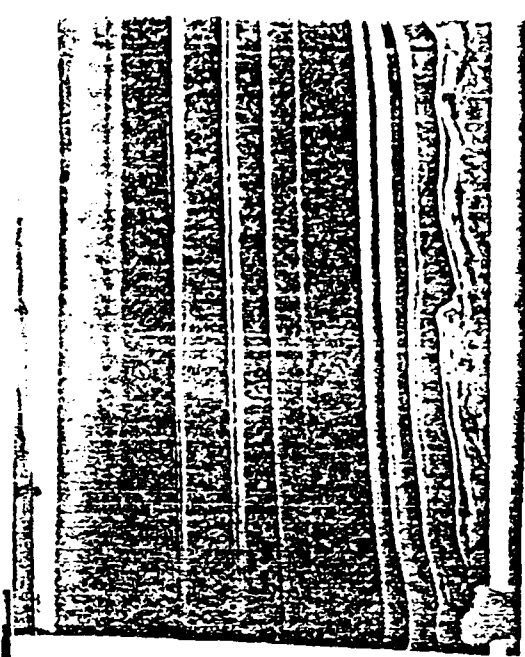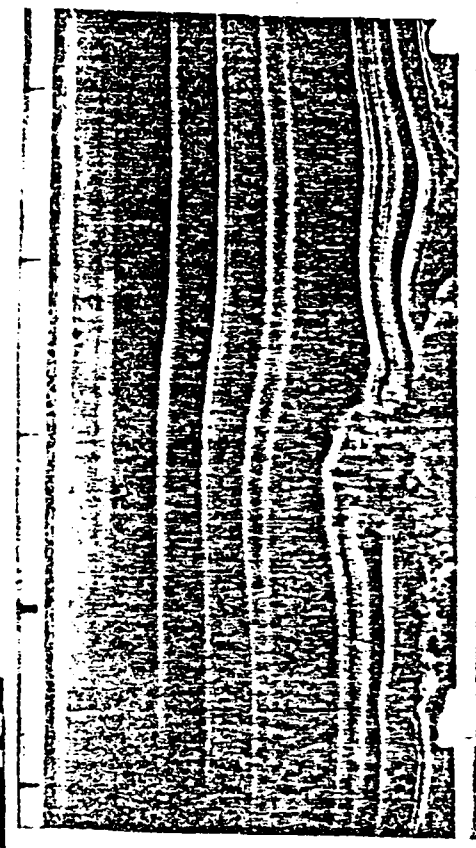
Figure 41.

$= 240°$
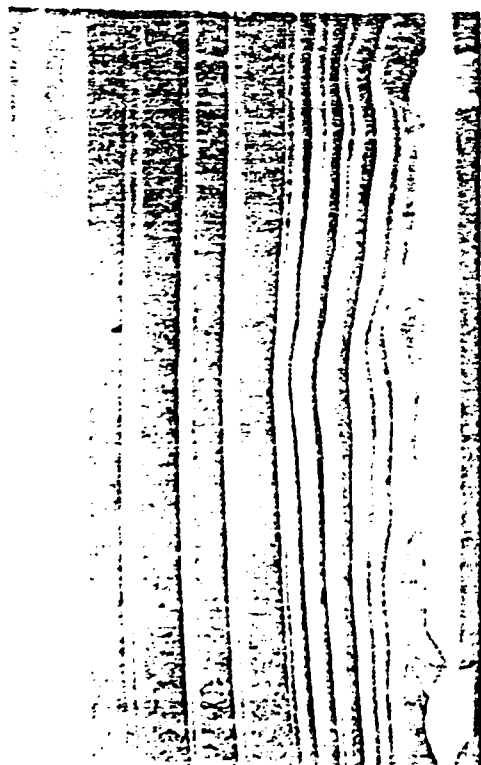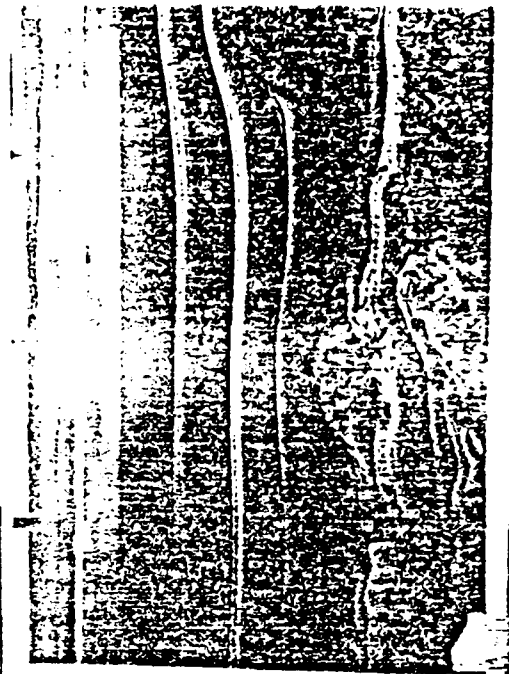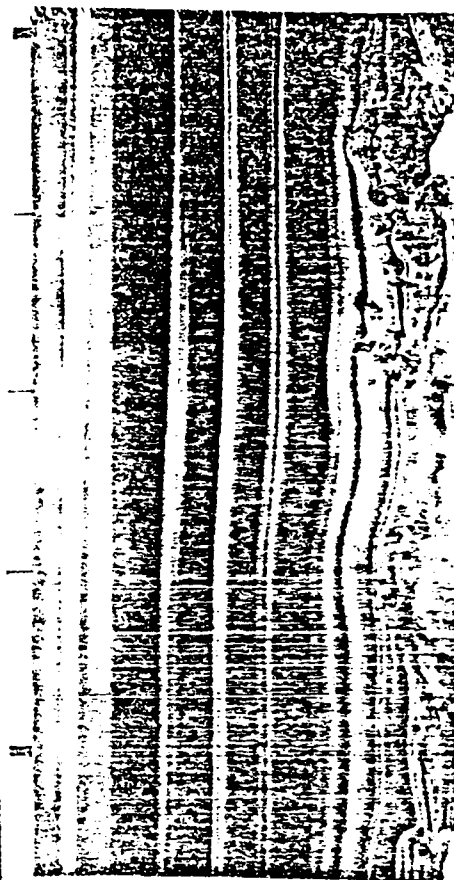
PLANE = +4 INCHES

Figure 42.

= 270°
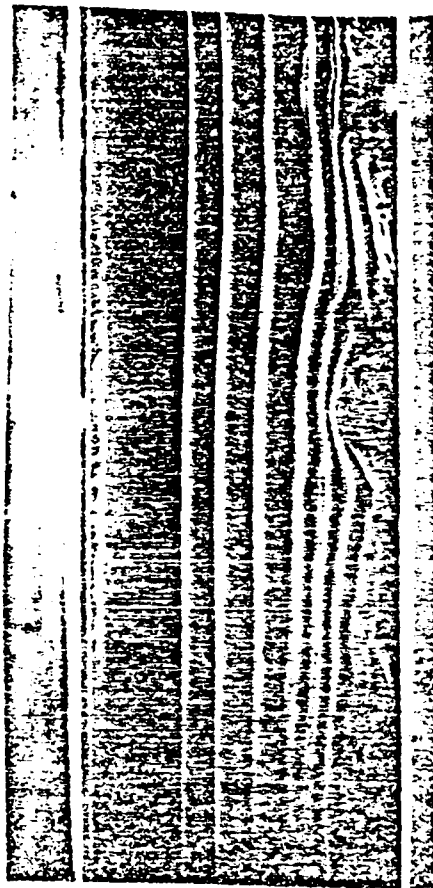
PLANE = -4 INCHES
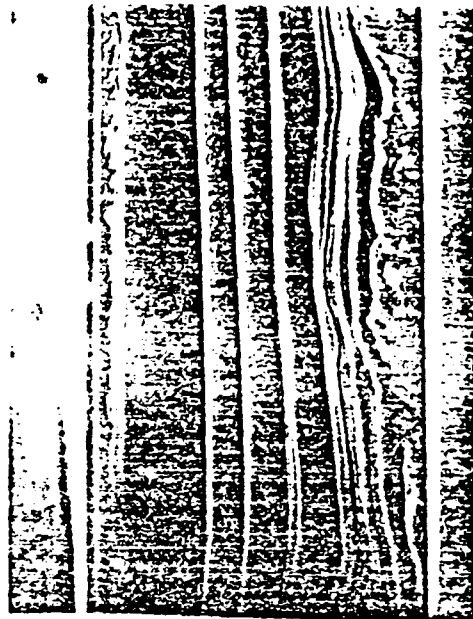
Figure 43.

= 270°
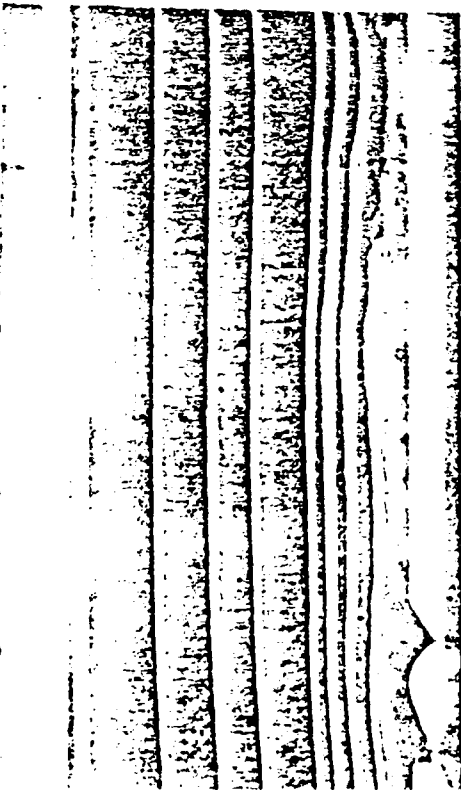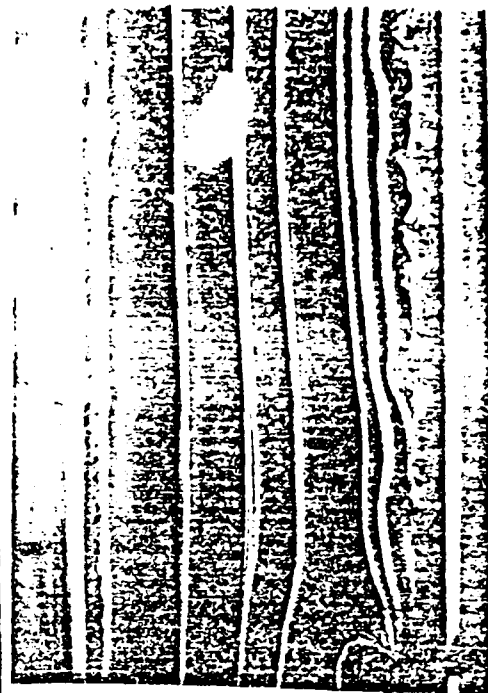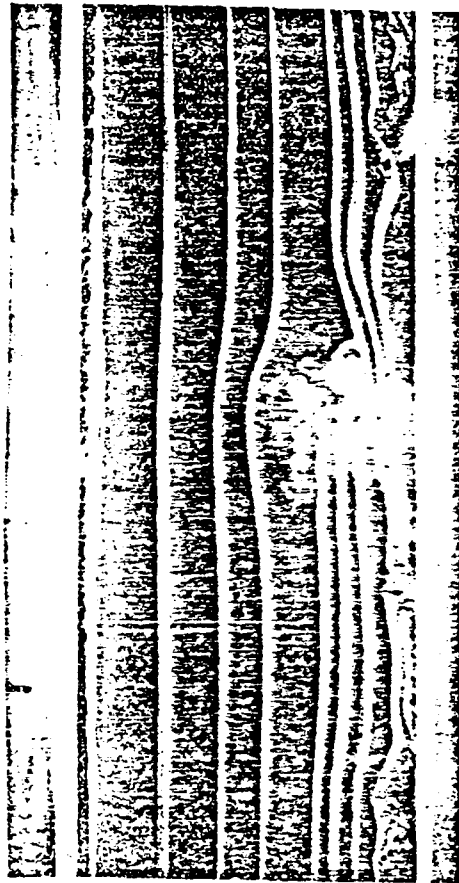
PLANE = - 2 INCHES

Figure 44.

$= 270°$

PLANE = CENTERLINE

Figure 45.

= 270°

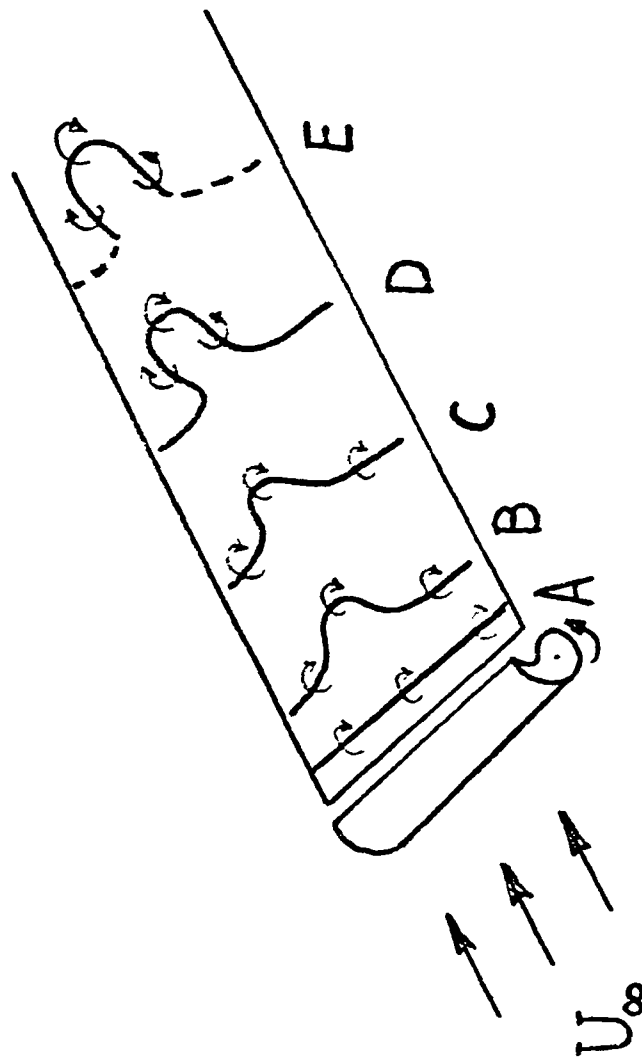PLANE = +2 INCHES

Figure 46.

= 270°
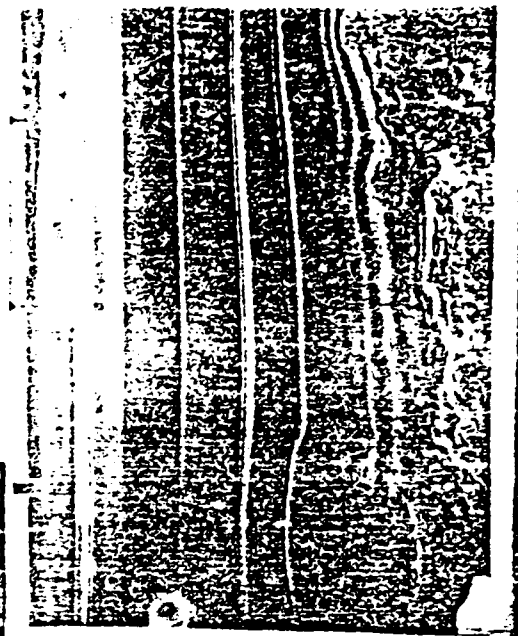
PLANE = +4 INCHES

Figure 47.

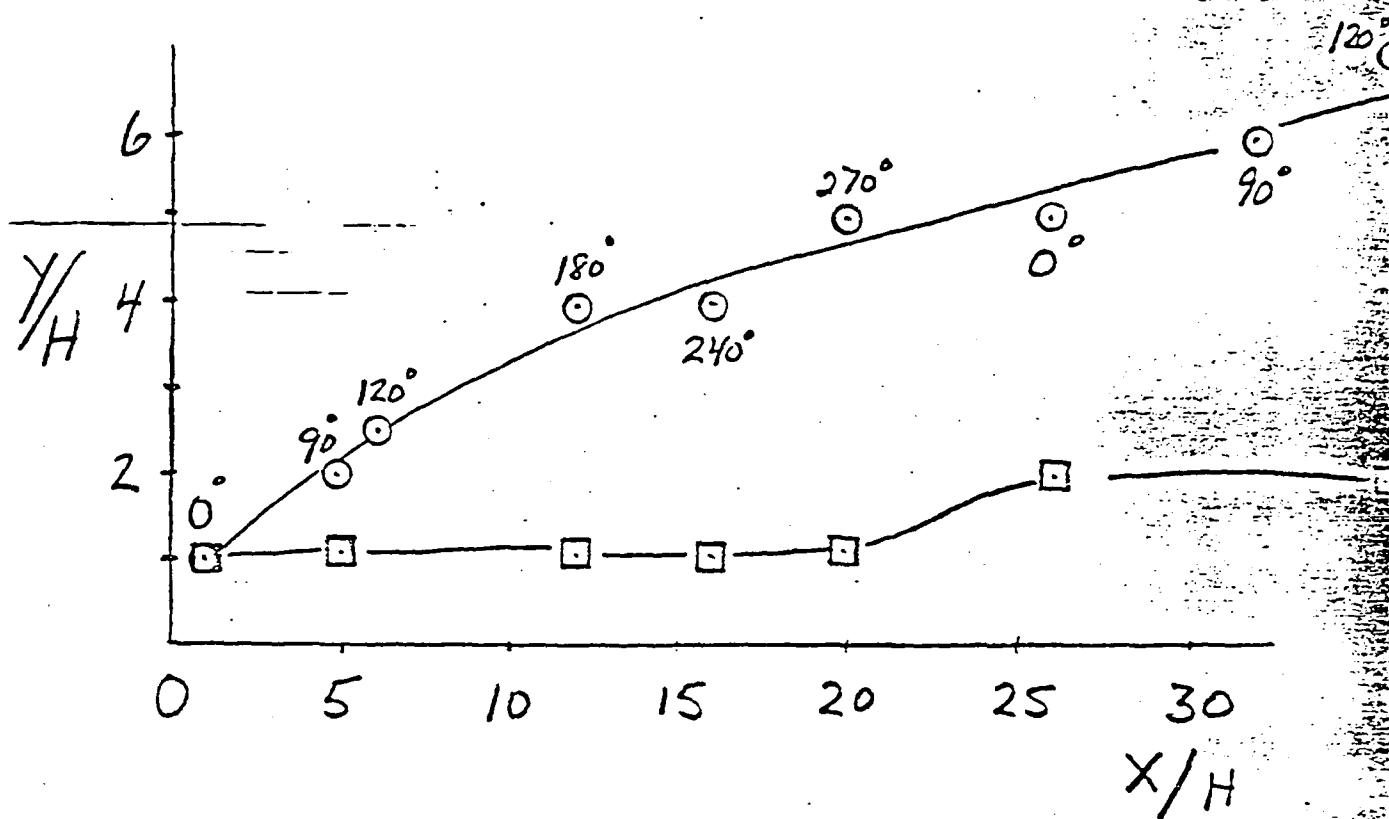Figure 48. Schematic of the vortex deformation based on the flow visualization results.

Figure 49. Vortex trajectories in the centerline
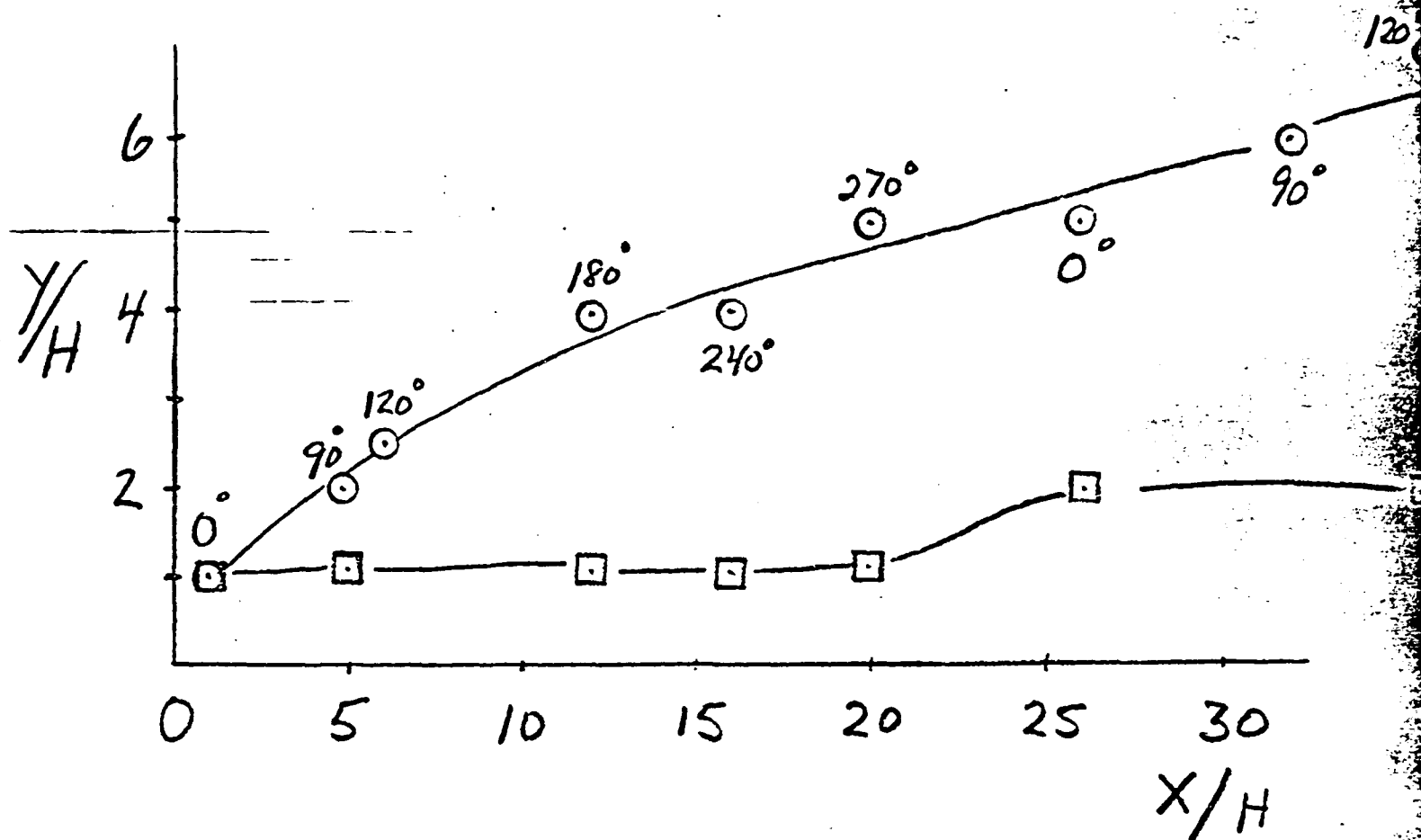plane (0) and the ± 4 plane (□).

Figure 49. Vortex trajectories in the centerline
plane (0) and the ± 4 plane (□).